

May 2015

Gravitational-Wave Science with the Laser Interferometer Gravitational-Wave Observatory

Madeline Wade

University of Wisconsin-Milwaukee

Follow this and additional works at: <https://dc.uwm.edu/etd>

 Part of the [Astrophysics and Astronomy Commons](#), and the [Physics Commons](#)

Recommended Citation

Wade, Madeline, "Gravitational-Wave Science with the Laser Interferometer Gravitational-Wave Observatory" (2015). *Theses and Dissertations*. 933.

<https://dc.uwm.edu/etd/933>

This Dissertation is brought to you for free and open access by UWM Digital Commons. It has been accepted for inclusion in Theses and Dissertations by an authorized administrator of UWM Digital Commons. For more information, please contact open-access@uwm.edu.

GRAVITATIONAL-WAVE SCIENCE WITH THE LASER
INTERFEROMETER GRAVITATIONAL-WAVE
OBSERVATORY

by

Madeline C. Wade

A DISSERTATION SUBMITTED IN
PARTIAL FULFILLMENT OF THE
REQUIREMENTS FOR THE DEGREE OF

DOCTOR OF PHILOSOPHY
IN PHYSICS

at

The University of Wisconsin–Milwaukee
May 2015

ABSTRACT

GRAVITATIONAL-WAVE SCIENCE WITH THE LASER INTERFEROMETER GRAVITATIONAL-WAVE OBSERVATORY

The University of Wisconsin–Milwaukee, May 2015
Under the Supervision of Professor Jolien Creighton

Gravitational-waves, as predicted by Einstein’s theory of general relativity, are oscillations of spacetime caused by the motion of masses. Although not yet directly detected, there is strong evidence for the existence of gravitational-waves. Detectable gravitational-waves will come from dramatic astrophysical events, such as supernova explosions and collisions of black holes. The Laser Interferometer Gravitational-wave Observatory (LIGO) is a network of detectors designed to make the first direct detection of gravitational waves. The upgraded version of LIGO, Advanced LIGO (aLIGO), will offer a dramatic improvement in sensitivity that will virtually guarantee detections. Gravitational-wave detections will not only illuminate mysterious astrophysical systems but will also provide a test of Einstein’s theory of general relativity.

This dissertation discusses the development of software for use in aLIGO and tests on aLIGO data for verifying general relativity. I have constructed and tested critical components of aLIGO’s low-latency data analysis network. Low-latency refers to unnoticeable delays in the performance of software. I have developed and tested low-latency calibration software that takes the raw data from the LIGO detectors and converts it into gravitational-wave strain. I have also conducted a search on initial LIGO data for gravitational waves from sub-solar mass black hole binary systems. This search is a proof-of-principle search for an aLIGO binary neutron star search, which is the most promising search for the first direct gravitational-wave detection. Finally, I have investigated the ability of aLIGO to detect violations of general relativity through a gravitational-wave detection of the orbit and collision of two astrophysical objects. The dissertation work discussed here is aimed to improve low-latency data production and analysis in gravitational-wave physics and will further the scientific findings from a gravitational-wave detection.

TABLE OF CONTENTS

1	Introduction	1
1.1	Review of general relativity and gravitational waves	3
1.1.1	Linearized gravity	5
1.1.2	Vacuum solution to linearized Einstein field equations	6
1.1.3	Effect of gravitational waves on matter	6
1.1.4	Source of gravitational waves	9
1.2	Compact binary coalescence as a source of gravitational waves	11
1.3	Detecting gravitational waves with the Laser Interferometer Gravitational-wave Observatory (LIGO)	14
1.3.1	Order of magnitude estimate of LIGO sensitivity	14
1.3.2	Main components of LIGO	16
1.3.3	Noise in the LIGO interferometers	19
2	Calibration of the Advanced LIGO Instruments	22
2.1	Introduction	22
2.2	A brief description: LIGO length sensing and control system	23
2.3	Injections and $h(t)$ construction	26
2.4	Tracking slowly-varying, time-dependent changes in calibration, $\gamma(t)$	28
2.5	Constructing time domain FIR filters from the frequency domain models	29
2.6	Time domain calibration pipeline	34
2.6.1	gstlal calibration pipeline	34
2.6.2	Calibration state vector	36
2.7	Engineering runs as tests of the calibration procedure	38
2.7.1	Early engineering runs (ER3-ER5)	38
2.7.2	Recent engineering run (ER6)	40
2.8	Conclusions	41

3	Search for sub-solar mass binary systems in Initial LIGO data	43
3.1	Introduction	43
3.1.1	Matched filter statistic	44
3.1.2	Maximum likelihood statistic	45
3.1.3	Non-stationary, non-Gaussian noise	48
3.2	Sub-solar mass binary search motivation	51
3.2.1	Astrophysical motivation	51
3.2.2	Computational motivation	54
3.3	Coherent and null streams for co-located detectors	55
3.4	Search software algorithm	58
3.4.1	Low-latency SNR calculation	59
3.4.2	Likelihood statistic in <code>gstlal_inspiral</code>	62
3.4.3	False alarm probability (FAP) and false alarm rate (FAR)	65
3.5	Results	66
3.5.1	Search sensitivity	67
3.5.2	Required computing resources	69
3.5.3	Gravitational-wave detection results	71
3.6	Conclusions	72
4	Tests of cosmic censorship and the no-hair theorem with aLIGO	73
4.1	Introduction	73
4.2	Compact binary coalescence (CBC) gravitational waveform with higher harmonics	77
4.3	Parameter estimation	83
4.3.1	Fisher matrix	83
4.3.2	Validity of the Fisher matrix	83
4.3.3	Singular-value decomposition	89
4.4	Parameters and parameter space bounds	90
4.4.1	Spinning waveform	90
4.4.2	Nonspinning, tidal waveform	91
4.5	Results	93

4.5.1	Detectable apparent violations of the cosmic censorship conjecture	93
4.5.2	Detectable deviations from the no-hair theorem	103
4.6	Discussion	106
4.7	Conclusions	110
5	Conclusions	112
5.1	Summary	112
5.2	Further work	114
5.3	Closing remarks	115

LIST OF FIGURES

1	Hulse-Taylor binary system orbital decay	2
2	Effect of a plus polarized gravitational wave on a ring of test particles . .	7
3	Effect of a cross polarized gravitational wave on a ring of test particles .	8
4	Compact binary coalescence waveform	13
5	Michelson interferometer	15
6	Fabry-Perot, Michelson interferometer	17
7	Power-recycled, Fabry-Perot, Michelson interferometer	18
8	Signal-recycled, power-recycled, Fabry-Perot, Michelson interferometer .	19
9	LIGO amplitude spectral densities	20
10	DARM feedback loop	24
11	DARM feedback loop with injections	26
12	Actuation FIR filter accuracy	30
13	Inverse sensing FIR filter accuracy	31
14	Actuation FIR filter, split over time	32
15	Actuation FIR filter, centered in time	33
16	Calibration in the low-latency data network	35
17	Schematic of calibration pipeline	35
18	Time domain $h(t)$ accuracy	40
19	SNR time series with local peak finding	47
20	SNR time series for loud glitch in data	48
21	χ^2 vs. ρ plot for noise and injections	50
22	Template bank for sub-solar mass binary search	53

23	Sensitivity of H1, H2, and a coherent combination of H1 and H2	57
24	A flow chart of the <code>gstlal_inspiral</code> pipeline.	58
25	Missed and found injections for SSM binary search	68
26	Sensitive distance of SSM binary search	70
27	Results of SSM binary search	71
28	Results for the validity of the Fisher matrix using $ \log r $ test	84
29	Ambiguity function for different systems	87
30	Parameter errors for varying values of spin	93
31	Illustration of the effect of symmetric mass ratio prior on parameter errors	94
32	Parameter errors for spinning BBH system	96
33	Parameter errors for spinning NS-BH system	97
34	Parameter errors for tidal BBH system	103

LIST OF TABLES

1	Template bank stats for aLIGO BNS and iLIGO SSM searches	56
2	Table of results for spinning BBH system	98
3	Table of results for spinning BBH system with additional phase corrections	99
4	Table of results for spinning NS-BH system	100
5	Table of results for spinning NS-BH system with additional phase corrections	101
6	Table of results for tidal BBH system	104
7	Summary of results table	109

ACKNOWLEDGMENTS

“Now I see a lot can come from the helping hand of a few good friends.”

— The Dump, *The Little Blue Truck* by Alice Shertle

A lot has come from the helping hands of many good friends, family, and colleagues throughout my graduate school career. First and foremost, I would not be where I am today without the constant love and support of my husband, Les Wade. He has helped countless times in numerous ways throughout the entire graduate school adventure, from working together on problem sets and tackling tricky research hurdles together to reminding me to smile and relax when times got tough. His careful, thoughtful approach to problem solving has been invaluable on many, many occasions. Of course, I must also thank my beautiful, rambunctious, smiley, and talented baby girl, Ruth. Raising a baby during the last year of graduate school had its challenges, but the endless joy she has brought me, especially when the dissertation became gloomily daunting, has gotten me through more late nights than I can count. I need to mention my rascally dogs, Brewer and Colby, who have cheered me up, distracted me, and helped me to keep my sanity over the years. Finally, I would like to thank my Mom, mother-in-law, father-in-law, brother, sister, and brother-in-law for supporting me in many different ways throughout graduate school.

I received excellent research advising and support from my advisors Jolien Creighton and Xavier Siemens. Both Jolien and Xavi were patient, supportive, and persistent in pushing me along a track towards independent research. They have been excellent mentors who I have to thank for much of my success. All of the members of the CGCA, including Chris Pankow, Laura Nuttall, Sarah Caudill, Evan Ochsner, Patrick Brady, Tom Downes, and Adam Mercer, have been wonderful collaborators and friends over the years. I would like to thank Sydney Chamberlin, Tom Linz, and Les Wade (again) for making the many late night problem set sessions and early morning classes on no sleep much more enjoyable than they would have otherwise been. A special thank you to Sydney for the countless coffee breaks and pep talks that I have needed over the years.

Thank you to Alex Urban, Justin Ellis, and Brian Vlcek for always being supportive friends and fellow graduate students.

Finally, I acknowledge all of the contributions that my collaborators in the LIGO Scientific Collaboration (LSC) have provided to this dissertation work. Specifically, I would like to mention Jolien Creighton, Xavier Siemens, Chad Hanna, Kipp Cannon, Drew Keppel, Alex Nielsen, Evan Ochsner, Joe Betzweiser, and Jeff Kissel. The LSC has provided a wonderful research environment that fosters independence, excellence, and collaboration. I am grateful for the opportunity to complete my dissertation as a member of the LSC.

CONVENTIONS

- I use Greek letters ($\alpha, \beta, \gamma, \dots$) to indicate spacetime indices, which are summed over 0, 1, 2, 3, and Latin letters (a, b, c, \dots) to indicate spatial indices, which are summed over 1, 2, 3.
- I use the Einstein summation convention where there is an implied sum over dummy indices. For example, $\eta_{\alpha\mu}T^\mu = \sum_{\mu=0}^3 \eta_{\alpha\mu}T^\mu$.
- The Fourier transform and inverse Fourier transform conventions used are

$$\begin{aligned}\tilde{x}(f) &= \int_{-\infty}^{\infty} x(t)e^{-2\pi ift} dt \\ x(t) &= \int_{-\infty}^{\infty} \tilde{x}(f)e^{2\pi ift} df .\end{aligned}$$

- Bold font indicates a vector or a matrix, such as **J**, **S** and **x**.

Chapter 1

Introduction

“Begin at the beginning and go on until you come to the end: then stop.”

— The King, *Alice in Wonderland*
by Lewis Carroll

Newton described gravity as an attractive force between masses. Newtonian gravity is an excellent theory to explain phenomena in the slowly-moving, weak-field regime, but the theory contains an inherent flaw. In Newton’s theory, gravity is a force between two masses that is inversely proportional to the square of the distance between the masses. Such a formalism requires that information about one mass be instantaneously conveyed to the other mass, which violates causality. This conundrum was solved by Einstein in his re-formulation of gravity as a consequence of the geometry of spacetime, instead of a force. Einstein’s theory of general relativity postulates that masses cause curvature in spacetime. Everything that moves throughout spacetime, whether it be massive objects or light, travels along geodesics. As the spacetime becomes curved by masses, the geodesics are altered, leading to, for example, orbits.

Gravity also contains radiative properties in general relativity. Gravitational radiation, known as gravitational waves, is the propagation of perturbations in spacetime that travel at the speed of light. Gravitational waves are caused by the motion of masses in spacetime, and they become stronger for more relativistic systems. Any gravitational waves produced by day-to-day activities are incredibly small. The only moving masses that can produce detectable gravitational waves are dramatic astrophysical events, such

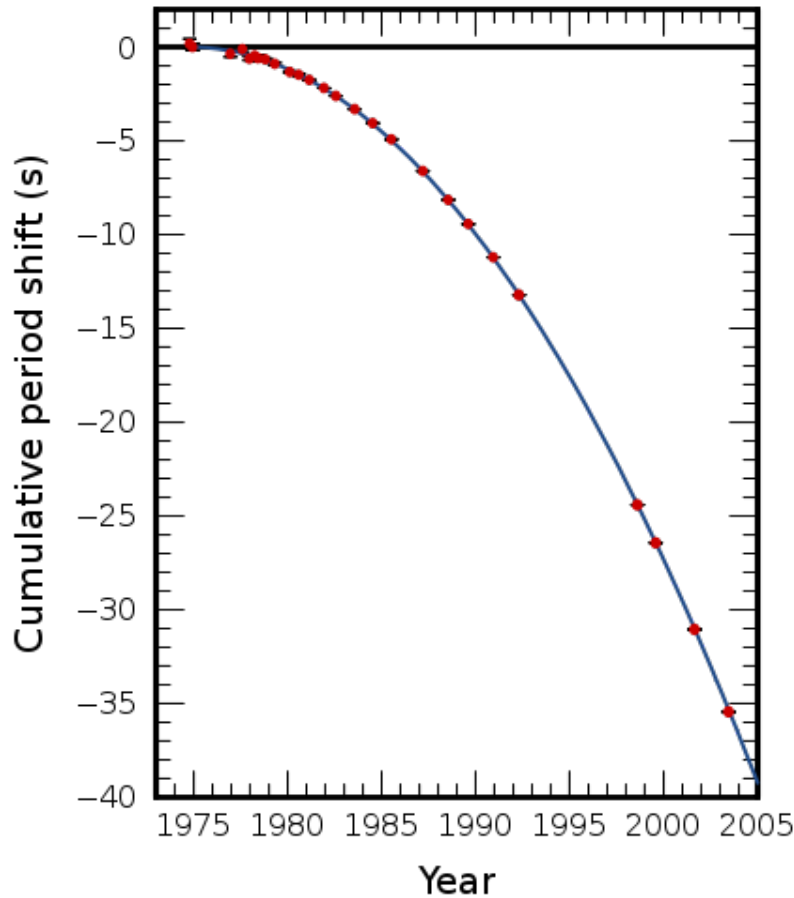


Figure 1 : Measured data (red) for the orbital decay of a binary star system and the prediction from general relativity (blue) of the orbital decay due to gravitational-wave emission.

as the coalescence of binary neutron stars and supernova.

Gravitational waves have never been directly detected, but there is strong evidence for the existence of gravitational waves. As a system emits gravitational radiation, the system loses energy that is carried away with the radiation. The orbit of a binary system will therefore decay over time as energy is lost due to gravitational radiation. Hulse and Taylor were able to very accurately measure the decay of a binary neutron star system, and the results were incredibly accurately described by the loss of energy due to gravitational radiation. Fig. 1 shows the data points obtained for the orbital decay along with the prediction from general relativity.

The Laser Interferometer Gravitational-wave Observatory (LIGO) is an on-going experiment designed to directly detect gravitational waves for the first time. The first

detections of gravitational waves will provide an excellent test of general relativity and are bound to reveal new astrophysics. Information about the source is encoded into the gravitational waves, and we are able to extract this source information from a detected gravitational wave. In this sense, LIGO will become a new type of telescope that will surely lead to improved information about observed dramatic astrophysical events.

This dissertation describes my contributions to various parts of LIGO's gravitational-wave science workflow. This chapter gives a brief overview of the theory behind gravitational wave physics and introduces the most promising source of gravitational waves for LIGO as well as the basic setup of the LIGO detectors. Ch. 2 discusses the process of turning the output of the LIGO detectors into a quantity that describes the measured effect of a gravitational wave on the detector. Ch. 3 discusses a search for gravitational-wave signals in LIGO data from sub-solar mass binary black hole systems. Ch. 4 demonstrates an example of how a detection of gravitational waves can be used to test the theory of general relativity. Finally, in Ch. 5, I summarize the results obtained in this dissertation succinctly.

1.1 Review of general relativity and gravitational waves

This section assumes a basic knowledge of general relativity, such as that contained in Hartle (2003). I only briefly summarize the salient points in gravitational-wave physics, and a more detailed introduction can be found in, for example, Creighton & Anderson (2011) and Flanagan & Hughes (2005). This section follows closely with the discussion found in Creighton & Anderson (2011) and Flanagan & Hughes (2005).

Since general relativity involves a geometric description of spacetime, the most important and fundamental quantity in general relativity is the description of the distance between two points in spacetime. The physical squared distance between two points is

$$ds^2 = g_{\mu\nu} dx^\mu dx^\nu \quad (1.1.1)$$

where $g_{\mu\nu}$ is known as the metric and dx^μ represents the infinitesimal coordinate distance between two points. The metric maps coordinate distances into physical distances. When no curvature is present (flat spacetime), the metric is given the symbol $\eta_{\alpha\beta}$, which is

defined

$$\eta_{\alpha\beta} = \begin{bmatrix} -c^2 & 0 & 0 & 0 \\ 0 & 1 & 0 & 0 \\ 0 & 0 & 1 & 0 \\ 0 & 0 & 0 & 1 \end{bmatrix} \quad (1.1.2)$$

in Cartesian coordinates. Since the metric is a map from coordinate distance into physical distance, it contains a description of both the physical curvature of spacetime and any apparent curvature inherent in a coordinate system (e.g. polar coordinates).

As eloquently stated by John Archibald Wheeler, “Spacetime tells matter how to move; matter tells spacetime how to curve.” The metric describes the curvature of spacetime to which matter will respond. The stress-energy tensor describes the matter properties that will tell spacetime how to curve. The components of the stress energy tensor are

$$T^{00} = \rho \quad (1.1.3)$$

$$T^{0i} = T^{i0} = J^i \quad (1.1.4)$$

$$T^{ij} = S^{ij} \quad (1.1.5)$$

where ρ is mass density, \mathbf{J} is momentum density, and \mathbf{S} is the stress energy tensor.

The Einstein field equations formalize the connection between spacetime and matter,

$$G_{\alpha\beta} = \frac{8\pi G}{c^4} T_{\alpha\beta} , \quad (1.1.6)$$

where $G_{\alpha\beta}$ is the Einstein tensor,

$$G_{\alpha\beta} = R_{\alpha\beta} - \frac{1}{2} g_{\alpha\beta} R . \quad (1.1.7)$$

The Ricci tensor $R_{\alpha\beta}$ and the Ricci scalar R are contractions of the Riemann curvature tensor $R_{\alpha\beta\gamma\delta}$,

$$R_{\alpha\beta} = g^{\mu\nu} R_{\alpha\mu\beta\nu} \quad (1.1.8)$$

$$R = g^{\mu\nu} R_{\mu\nu} . \quad (1.1.9)$$

The Riemann curvature tensor is given by derivatives of the metric and characterizes the physical curvature of spacetime.

The Einstein tensor is divergenceless,

$$\nabla_{\mu} G^{\mu\nu} = 0, \quad (1.1.10)$$

and so the equations of motion for matter,

$$\nabla_{\mu} T^{\mu\nu} = 0, \quad (1.1.11)$$

follow from the Einstein field equations.

1.1.1 Linearized gravity

Linearized gravity refers to the weak-field approximation where the metric is taken to be a small perturbation away from flat spacetime,

$$g_{\alpha\beta} = \eta_{\alpha\beta} + h_{\alpha\beta} \quad (1.1.12)$$

where $\|h_{\alpha\beta}\| \ll 1$. All terms $\mathcal{O}(h^2)$ are ignored in the linearized gravity limit, which reduces Einstein's field equations to

$$-\eta^{\mu\nu} \frac{\partial^2 \bar{h}_{\alpha\beta}}{\partial x^{\mu} \partial x^{\nu}} - \eta_{\alpha\beta} \frac{\partial^2 \bar{h}^{\mu\nu}}{\partial x^{\mu} \partial x^{\nu}} + \frac{\partial^2 \bar{h}_{\beta}^{\mu}}{\partial x^{\alpha} \partial x^{\mu}} + \frac{\partial^2 \bar{h}_{\alpha}^{\mu}}{\partial x^{\mu} \partial x^{\beta}} + \mathcal{O}(h^2) = \frac{16\pi G}{c^4} T_{\alpha\beta}, \quad (1.1.13)$$

where $\bar{h}_{\alpha\beta}$ is the trace-reversed metric and is defined $\bar{h}_{\alpha\beta} \equiv h_{\alpha\beta} - \frac{1}{2}\eta_{\alpha\beta}h$. The trace of the trace-reversed metric is the negative of the trace of the metric, $h = \eta^{\alpha\beta}h_{\alpha\beta} = -\bar{h}$, hence the name ‘‘trace-reversed metric.’’¹ The Einstein field equations can be simplified by making a gauge transformation into what is known as the Lorenz gauge. The Lorenz gauge condition requires that the divergence of the trace-reversed metric vanish,

$$\frac{\partial \bar{h}^{\mu\alpha}}{\partial x^{\mu}} = 0. \quad (1.1.14)$$

The linearized Einstein field equations in the Lorenz gauge are very simply written

$$-\square \bar{h}_{\alpha\beta} = \frac{16\pi G}{c^4} T_{\alpha\beta}, \quad (1.1.15)$$

where \square is the d'Alembertian operator in flat spacetime.

¹In linearized gravity the flat spacetime metric $\eta_{\alpha\beta}$ is used to raise and lower indices.

1.1.2 Vacuum solution to linearized Einstein field equations

In the weak-field limit where you are far from the source that is perturbing spacetime, it is safe to approximate spacetime as a vacuum. The linearized gravity, vacuum Einstein field equations are

$$\square \bar{h}_{\alpha\beta} = 0 \quad (1.1.16)$$

in the Lorenz gauge. This is a wave equation with the solution of a plane wave traveling at the speed of light. The Lorenz gauge condition implies that the plane wave solution is transverse. These transverse, plane-wave, metric perturbations traveling at the speed of light are called *gravitational waves*. If the plane wave is chosen to travel along the z -direction, then the waves are only a function of the retarded time $t - z/c$.

It turns out there is further gauge freedom in the Lorenz gauge. Moving into a gauge where the metric perturbation is both traceless ($h = \bar{h} = 0$) and purely spatial ($h_{\alpha 0} = 0$), known as the transverse-traceless (TT) gauge, removes all remaining gauge freedom. Since the TT gauge is traceless, the metric and trace-reversed metric are the same in this gauge. All t and z components of the metric are zero due to the spatial and transverse properties of the TT gauge. This leaves four non-zero components: $h_{11}^{\text{TT}}, h_{22}^{\text{TT}}, h_{12}^{\text{TT}}, h_{21}^{\text{TT}}$. Due to symmetry of the metric,

$$h_{12}^{\text{TT}} = h_{21}^{\text{TT}} \equiv h_{\times} . \quad (1.1.17)$$

Since the metric is traceless, this further implies $h_{11}^{\text{TT}} + h_{22}^{\text{TT}} = 0$, which means

$$h_{11}^{\text{TT}} = -h_{22}^{\text{TT}} \equiv h_{+} . \quad (1.1.18)$$

The two remaining degrees of freedom in the metric, h_{+} and h_{\times} , represent physical degrees of freedom. These are the two possible polarizations of a gravitational wave. The names “+” and “ \times ” have meaning derived from the effect of each polarization on matter, discussed below.

1.1.3 Effect of gravitational waves on matter

In general relativity, the phenomenon of gravity is explained through the curvature of spacetime. Test masses freely-falling through spacetime simply follow geodesics of that

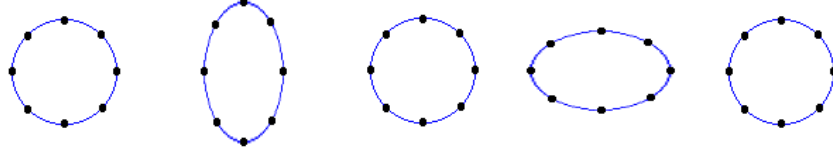


Figure 2 : The proper length between particles in a ring of freely-falling test particles would be affected as shown here for a purely plus polarized gravitational wave traveling into the page. This diagram is a snapshot in time as the wave's crests and troughs pass through the plane of the ring.

spacetime. Depending on how spacetime has been curved by matter, these geodesics could be elliptical orbits or straight lines or many other possible paths. The equations of motion for a particle following a geodesic in spacetime with metric $g_{\alpha\beta}$ are

$$\frac{d^2 x^\alpha}{d\tau^2} = -\Gamma_{\mu\nu}^\alpha \frac{dx^\mu}{d\tau} \frac{dx^\nu}{d\tau} \quad (1.1.19)$$

where τ is the proper time and $\Gamma_{\alpha\beta}^\gamma$ are the connection coefficients, which can be expressed in terms of the metric and derivatives of the metric as

$$\Gamma_{\alpha\beta}^\gamma = \frac{1}{2} g^{\gamma\delta} \left(\frac{\partial}{\partial x^\alpha} g_{\beta\delta} + \frac{\partial}{\partial x^\beta} g_{\delta\alpha} - \frac{\partial}{\partial x^\delta} g_{\alpha\beta} \right). \quad (1.1.20)$$

Re-parameterizing Eq. (1.1.19) in terms of coordinate time t and moving into the TT gauge in the linearized gravity, non-relativistic motion approximation, we reduce the equations of motion for a freely-falling particle to

$$\frac{d^2 x^\alpha}{dt^2} = 0. \quad (1.1.21)$$

This implies that test particles will not experience any *coordinate* acceleration as a result of gravitational waves in the TT gauge. In fact, this reveals the physical meaning of the TT gauge. The TT gauge, which contains only physical degrees of freedom of the gravitational wave in the metric, is the coordinate system that moves with particles as they are affected by a gravitational wave.

Gravitational waves do, however, have a physical effect on the motion of particles. Even though the coordinate distance between particles remains unchanged by a gravitational wave in the TT gauge, the *proper* distance between particles is affected. For a gravitational wave traveling along the z -direction, the proper distance along the x -direction

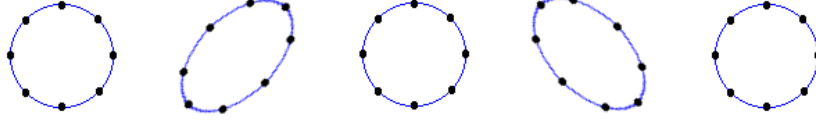


Figure 3 : The proper length between particles in a ring of freely-falling test particles would be affected as shown here for a purely cross polarized gravitational wave traveling into the page. This diagram is a snapshot in time as the wave's crests and troughs pass through the plane of the ring.

between two freely-falling particles located on the x -axis and separated by coordinate distance L'_1 is

$$L_1(t) = \int_0^{L'_1} \sqrt{g_{11}(t)} dx^1 \quad (1.1.22)$$

$$= \int_0^{L'_1} \sqrt{1 + h_{11}^{\text{TT}}(t)} dx^1 \quad (1.1.23)$$

$$\approx \int_0^{L'_1} \left[1 + \frac{1}{2} h_{11}^{\text{TT}}(t) \right] dx^1 \quad (1.1.24)$$

$$= L'_1 \left[1 + \frac{1}{2} h_{11}^{\text{TT}}(t) \right] . \quad (1.1.25)$$

Similarly, for a particle located on the y -axis and separated by coordinate distance L'_2 ,

$$L_2(t) \approx L'_2 \left[1 + \frac{1}{2} h_{22}^{\text{TT}}(t) \right] . \quad (1.1.26)$$

Considering particles located off of the x or y axes involves the remaining non-zero metric perturbations h_{12}^{TT} and h_{21}^{TT} . The proper distance between freely-falling particles will be a changing function of time in the presence of a gravitational wave. For a purely $+$ polarized gravitational wave, a ring of test particles would be perturbed as shown in Fig. 2, and for a purely \times polarized gravitational wave, a ring of test particles would be perturbed as shown in Fig. 3. The names $+$ and \times come from the effect each polarization has on a ring of test particles.

One method to detect such changes in proper distance is to use an interferometer. The end mirrors of the interferometer are considered test particles and the proper distance between the mirrors and the beam splitter will be affected by a passing gravitational wave. For an interferometer with arms along the x and y axes and a gravitational wave

propagating along the z axis,

$$\frac{\Delta L_1(t)}{L'_1} = \frac{L_1(t) - L'_1}{L'_1} \approx \frac{1}{2} h_{11}^{\text{TT}}(t) = \frac{1}{2} h_+(t) \quad (1.1.27)$$

$$\frac{\Delta L_2(t)}{L'_2} = \frac{L_2(t) - L'_2}{L'_2} \approx \frac{1}{2} h_{22}^{\text{TT}}(t) = -\frac{1}{2} h_+(t) . \quad (1.1.28)$$

The difference between the fractional change in length in each arm as induced by a gravitational wave is known as the *gravitational-wave strain* and is related to the gravitational-wave metric perturbation,

$$\frac{\Delta L(t)}{L} \equiv \frac{\Delta L_1(t) - \Delta L_2(t)}{L} \approx h_+(t) \quad (1.1.29)$$

where L is the average, unperturbed interferometer arm length (Thorne et al. 1987).

Generic gravitational waves incident on an interferometer will be a linear combination of the $+$ and \times polarizations. The mapping of a each polarization onto the detector strain is known as the antenna patterns, F_+ and F_\times . The total gravitational-wave strain incident on the interferometer is given by

$$\frac{\Delta L(t)}{L} \approx h(t) = F_+(\theta, \phi, \psi) h_+(t; \iota) + F_\times(\theta, \phi, \psi) h_\times(t; \iota) \quad (1.1.30)$$

where (θ, ϕ) are the source's sky position, ψ is the polarization angle, and ι is the inclination angle between the plane containing the source and the detector and the plane perpendicular to the polarization plane.

1.1.4 Source of gravitational waves

Secs. 1.1.2 and 1.1.3 describe how gravitational waves fall out of the linearized Einstein field equations in a vacuum and the effect of gravitational waves on matter, respectively. The source of gravitational waves is the motion of matter that is curving spacetime.

Including $\mathcal{O}(h^2)$ terms in the Einstein field equations gives

$$\square \bar{h}_{\alpha\beta} = -\frac{16\pi G}{c^4} T_{\alpha\beta} + \mathcal{O}(h^2) . \quad (1.1.31)$$

The $\mathcal{O}(h^2)$ terms can be absorbed into the stress-energy tensor to form an effective stress-energy tensor $\tau_{\alpha\beta}$,

$$\square \bar{h}_{\alpha\beta} = -\frac{16\pi G}{c^4} \tau_{\alpha\beta} . \quad (1.1.32)$$

Note that the effective stress-energy tensor $\tau_{\alpha\beta}$ is also divergenceless, which is consistent with the equations of motion of matter and the Lorenz gauge condition.

The solution for the trace-reversed metric perturbation is found using Green's functions to be

$$\bar{h}_{\alpha\beta}(t, \mathbf{x}) = \frac{4G}{c^4} \int \frac{\tau_{\alpha\beta}(t - \|\mathbf{x} - \mathbf{x}'\|/c, \mathbf{x}')}{\|\mathbf{x} - \mathbf{x}'\|} d^3x' . \quad (1.1.33)$$

We are located far away from the astrophysical sources of gravitational waves. Therefore, any gravitational-wave strain that we detect on Earth would validly fall into the far-field regime, where $\|\mathbf{x} - \mathbf{x}'\| \approx r$ for r being the distance from the source to \mathbf{x} . Assuming slow motion of the source, we can take $t - \|\mathbf{x} - \mathbf{x}'\|/c \approx t - r/c$. We seek the solution in the TT gauge, so we are therefore only concerned with spatial components of the metric. The spatial components of the effective stress-energy tensor can be related to the time component τ^{00} through identities that follow from the equations of motion of matter ($\partial_\mu \tau^{\mu\nu} = 0$). Employing these identities in the far-field limit, the solution to Einstein's field equations in the TT-gauge is

$$h_{ij}^{\text{TT}}(t) \approx \frac{2G}{c^4 r} \ddot{I}_{ij}^{\text{TT}}(t - r/c) \quad (1.1.34)$$

where

$$I_{ij}^{\text{TT}} = P_{ik} I^{kl} P_{lj} - \frac{1}{2} P_{ij} P_{kl} I^{kl} , \quad (1.1.35)$$

the quadrupole tensor is

$$I^{ij}(t) = \int x^i x^j \tau^{00}(t, \mathbf{x}) d^3x , \quad (1.1.36)$$

and the projection operator is $P_{ij} = \delta_{ij} - \hat{n}_i \hat{n}_j$. \hat{n}_i is the unit vector in the direction of propagation. Determining the gravitational-wave strain from a given system therefore involves computing the system's quadrupole tensor and taking time derivatives of the quadrupole tensor.

Recall, the orbit of a binary system will decay over time due to gravitational-wave emission. This is because gravitational waves carry energy with them. The stress-energy tensor for a gravitational wave in the TT-gauge is

$$T_{\alpha\beta}^{\text{GW}} = \frac{c^4}{32\pi G} \left\langle \frac{\partial h_{ij}^{\text{TT}}}{\partial x^\alpha} \frac{\partial h_{ij}^{\text{TT}}}{\partial x^\beta} \right\rangle \quad (1.1.37)$$

where $\langle \dots \rangle$ is an integral average. This can be used to compute the gravitational-wave luminosity, which is related to the third time derivative of the quadrupole tensor,

$$L_{\text{GW}} = -\frac{dE}{dt} = \frac{1}{5} \frac{G}{c^5} \left\langle \ddot{\mathcal{I}}_{ij} \ddot{\mathcal{I}}^{ij} \right\rangle \quad (1.1.38)$$

where

$$\mathcal{I}^{ij} \equiv \int \left(x^i x^j - \frac{1}{3} r^2 \delta^{ij} \right) \tau^{00}(\mathbf{x}) d^3x . \quad (1.1.39)$$

The gravitational-wave luminosity describes the energy carried away by gravitational waves from a system per unit time.

1.2 Compact binary coalescence as a source of gravitational waves

The most promising source for the first direct detection of gravitational waves is a compact binary coalescence (CBC) event, which is the inspiral, merger, and ringdown of a binary system composed of two compact bodies such as neutron stars or black holes. This is the most promising source for the first detection, because it is a source that we know exists and a source for which we have relatively good models. We model a CBC system as two orbiting point particles with masses m_1 and m_2 , orbital separation a , and orbital speed ω . We find the gravitational wave polarizations h_+ and h_\times using Eq. (1.1.34).

The non-zero components of the quadrupole tensor are

$$I_{11} = \frac{1}{2} \mu a^2 \frac{(1 + \cos^2 \iota)}{2} (1 + \cos 2\phi) \quad (1.2.1)$$

$$I_{22} = \frac{1}{2} \mu a^2 \frac{(1 + \cos^2 \iota)}{2} (1 - \cos 2\phi) \quad (1.2.2)$$

$$I_{12} = I_{21} = \frac{1}{2} \mu a^2 \cos \iota \sin 2\phi \quad (1.2.3)$$

where $\mu = m_1 m_2 / (m_1 + m_2)$, ι is the inclination angle of the observer from the orbital axis, and $\phi = \omega t$. Using Eq. (1.1.34), the non-zero components of the metric perturbation in the TT-gauge are

$$h_+ = h_{11}^{\text{TT}} = -h_{22}^{\text{TT}} = -\frac{4G\mu a^2 \omega^2}{c^4 r} \frac{(1 + \cos^2 \iota)}{2} \cos 2\phi \quad (1.2.4)$$

$$h_\times = h_{12}^{\text{TT}} = h_{21}^{\text{TT}} = -\frac{4G\mu a^2 \omega^2}{c^4 r} \cos \iota \sin 2\phi . \quad (1.2.5)$$

The gravitational-wave frequency f is twice the orbital frequency, which means $\omega = \pi f$. 12

We often express the metric perturbation in terms of the orbital speed $v = a\omega$,

$$h_+ = -\frac{2G\mu}{c^2 r} \left(\frac{v}{c}\right)^2 (1 + \cos^2 \iota) \cos 2\phi \quad (1.2.6)$$

$$h_\times = -\frac{4G\mu}{c^2 r} \left(\frac{v}{c}\right)^2 \cos \iota \sin 2\phi. \quad (1.2.7)$$

As gravitational waves carry energy away from the system, the orbital separation of the system decays. Over time, the bodies orbit closer and closer together. Eventually the two bodies merge, which is known as the coalescence. The time until coalescence in terms of the system's initial velocity v_0 is

$$t_c = \frac{5}{256\eta} \frac{GM}{c^3} \left(\frac{v_0}{c}\right)^{-8} \quad (1.2.8)$$

where $M = m_1 + m_2$. This is obtained by integrating the conservation of energy equation from v_0 to infinity. Conservation of energy implies that the luminosity of gravitational-wave emission, as given by Eq. (1.1.38), equal the rate of energy loss in the binary system, which we approximate using the Newtonian energy.

As the orbit of the system decays, the phase ϕ and speed v evolve over time. Eqs. (1.2.6) and (1.2.7) are therefore functions of time through $\phi(t)$ and $v(t)$. The plus and cross gravitational-wave polarizations as a function of time for a CBC system in the Newtonian limit are

$$h_+(t) = -\frac{GM}{c^2 r} \frac{1 + \cos^2 \iota}{2} \left(\frac{c^3(t_c - t)}{5GM}\right)^{-1/4} \cos \left[2\phi_c - 2 \left(\frac{c^3(t_c - t)}{5GM}\right)^{5/8} \right] \quad (1.2.9)$$

$$h_\times(t) = -\frac{GM}{c^2 r} \cos \iota \left(\frac{c^3(t_c - t)}{5GM}\right)^{-1/4} \sin \left[2\phi_c - 2 \left(\frac{c^3(t_c - t)}{5GM}\right)^{5/8} \right] \quad (1.2.10)$$

for $t < t_c$ where t_c and ϕ_c are the time and phase of coalescence, respectively, and

$$\mathcal{M} = \frac{(m_1 m_2)^{3/5}}{M^{1/5}}. \quad (1.2.11)$$

A generic gravitational wave induces a strain on a detector, also known as the *gravitational waveform*, given by Eq. (1.1.30). For a CBC system, the strain as a function of time in the Newtonian limit is

$$h(t) = -\frac{GM}{c^2 D_{\text{eff}}} \left[\frac{c^3(t_0 - t)}{5GM} \right]^{-1/4} \cos \left(2\phi_0 - 2 \left[\frac{c^3(t_0 - t)}{5GM} \right]^{5/8} \right) \quad (1.2.12)$$

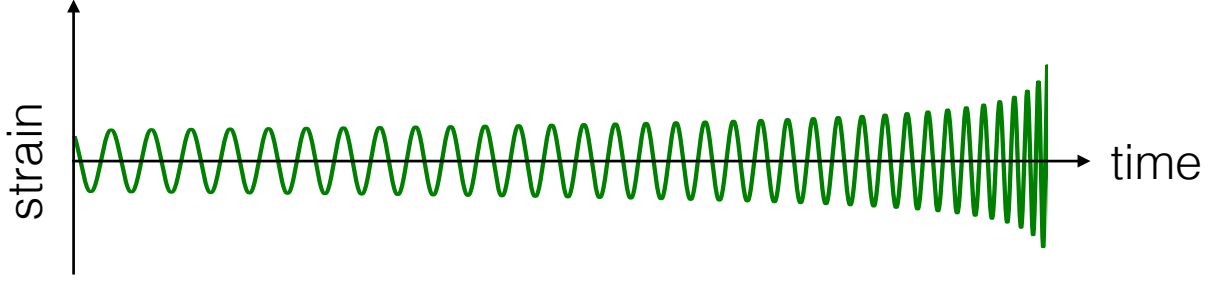


Figure 4 : An example CBC chirp waveform as a function of time.

where $t < t_0$ and

$$\phi_0 = \phi_c - \frac{1}{2} \tan^{-1} \left(\frac{F_{\times} 2 \cos \iota}{F_{+}(1 + \cos^2 \iota)} \right) \quad (1.2.13)$$

$$D_{\text{eff}} = r \left[F_{+}^2 \left(\frac{1 + \cos^2 \iota}{2} \right)^2 + F_{\times}^2 \cos^2 \iota \right]^{-1/2}, \quad (1.2.14)$$

and t_0 is the termination time, which refers to the time of coalescence as observed in the detector. A plot of an example waveform is shown in Fig. 4. The amplitude and frequency of the waveform increase with time. If the waveform were played as an audio stream it would sound like a chirp. For this reason, the CBC waveform is often referred to as a *chirp waveform*. Since, at the Newtonian level, the CBC waveform is a function of mass only through \mathcal{M} as defined in Eq. (1.2.11), \mathcal{M} is called the *chirp mass*.

The gravitational waveform is often expressed in the frequency domain instead of the time domain. Using the stationary phase approximation (SPA), the Fourier transform of the CBC waveform in the Newtonian limit is

$$\tilde{h}(f) = \sqrt{\frac{5\pi G^2 \mathcal{M}}{24 c^5 D_{\text{eff}}}} \left(\frac{\pi G \mathcal{M} f}{c^3} \right)^{-7/6} e^{-i\psi_{\text{SPA}}(f)} \quad (1.2.15)$$

where

$$\psi_{\text{SPA}}(f) = 2\pi f t_c - 2\phi_c - \frac{\pi}{4} + \frac{3}{128} \left(\frac{\pi \mathcal{M} G f}{c^3} \right)^{-5/3}. \quad (1.2.16)$$

All of the expressions reviewed so far are in the Newtonian limit where $GM/c^2 R \ll 1$ and $v/c^2 \ll 1$ for a system with characteristic size R , mass M , and speed v . Post-Newtonian solutions are obtained by keeping higher order corrections to the metric and stress-energy tensor and carrying these corrections throughout each derivation. In practice, much effort is put into computing post-Newtonian corrections to the energy and flux equations, which are inputs for $\phi(t)$ and $v(t)$ in the derivation of $h(t)$.

1.3 Detecting gravitational waves with the Laser Interferometer Gravitational-wave Observatory (LIGO) ¹⁴

The expected gravitational-wave strain from astrophysical sources is on the order of $h \sim 10^{-20}$, which is equivalent to measuring a ΔL that is the width of a human hair if the unperturbed length L is the distance between Earth and the closest star. In order to measure metric perturbations on this order, we need to design a detector that is incredibly sensitive to distance changes. The Laser Interferometer Gravitational-wave Observatory (LIGO) is a ground-based interferometer designed to meet such sensitivity standards. The first generation of the LIGO experiment, Initial LIGO (iLIGO), was in operation from 2002-2007. It was then upgraded to Enhanced LIGO (eLIGO) that ran from 2009-2010. The next generation of detectors, Advanced LIGO (aLIGO), are just starting to come online. We anticipate the first science-quality data to be taken in the fall of 2015. The sections below describe the basic components of LIGO and the major sources of noise in the detector. These sections are adapted from Creighton & Anderson (2011).

1.3.1 Order of magnitude estimate of LIGO sensitivity

The most simplified picture of LIGO is as a Michelson interferometer. Fig. 5 is a schematic of the layout of a Michelson interferometer. The interference pattern created at the photodiode depends on the difference in length of the two interferometer arms, $L_x - L_y$. If the length of the arms are changed by amounts ΔL_x and ΔL_y , then the change in the interference pattern corresponds to the differential change in arm length $\Delta L = \Delta L_x - \Delta L_y$. The most obvious change in interference pattern occurs when a light fringe is shifted to a dark fringe. Such a change corresponds to a $\Delta L \sim \lambda_{\text{laser}}$. The wavelength of the laser in LIGO is approximately $1 \mu\text{m}$. If LIGO were only a Michelson interferometer, then in order to be sensitive to gravitational waves with strain $h = \Delta L/L \sim 10^{-20}$, then the average arm length L would have to be

$$L = \frac{\Delta L}{h} \sim \frac{\lambda_{\text{laser}}}{h} \sim \frac{10^{-6} \text{ m}}{10^{-20}} = 10^{14} \text{ m} , \quad (1.3.1)$$

which would require the LIGO arms to stretch from Earth out into the Kuiper belt. This is obviously unreasonable, and since LIGO is a well-funded NSF experiment that does

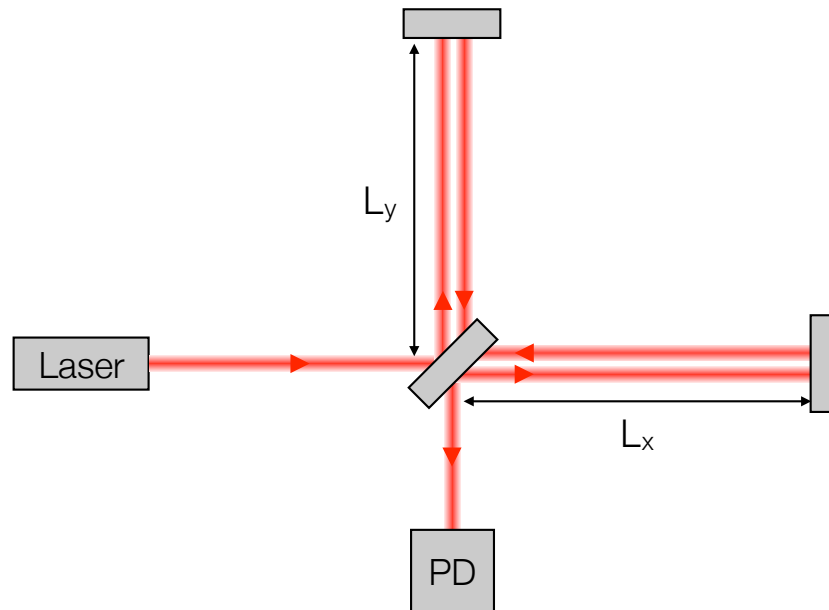


Figure 5 : Schematic of a Michelson interferometer. The laser light is sent to a beamsplitter where it then travels down the two interferometer arms of length L_x and L_y . The light bounces off of the end mirrors and travels back towards the beam splitter. Some of the recombined light travels back towards the laser and some travels towards the photodiode (PD).

not extend to Pluto, it must not be just a Michelson interferometer. In reality, the length of the LIGO arms is ~ 1 km, and such a Michelson interferometer would be sensitive to $h \sim 10^{-9}$.

One way to improve LIGO's sensitivity is to increase the effective length of the arms by having the light take many trips up and down the arms before recombining at the photodiode. However, there is a limit to how large the effective length should be which is $\sim \lambda_{\text{GW}}$. If the time the light remains in the arms becomes comparable to the period of the incident gravitational wave, then the light recombining at the cavity is much less sensitive to the gravitational wave perturbation, except at particular periods corresponding to the free spectral range of the interferometer arms. We seek to detect $\lambda_{\text{GW}} \sim 1000$ km with LIGO. By increasing the effective arm length to ~ 1000 km, LIGO's sensitivity improves to,

$$h \sim \frac{\Delta L}{L_{\text{effective}}} \sim \frac{\lambda_{\text{laser}}}{\lambda_{\text{GW}}} \sim \frac{10^{-6} \text{ m}}{10^6 \text{ m}} = 10^{-12}. \quad (1.3.2)$$

So far, this order of magnitude calculation has assumed that we are trying to detect a shift from a light to dark fringe in the interference pattern, which meant $\Delta L \sim \lambda_{\text{laser}}$. In

reality, with a high quality photodiode we can detect changes in the interference pattern that correspond to a departure from the expected number of photons arriving. Assuming the photon arrival follows a Poisson distribution, then we can detect

$$\Delta L \sim \frac{\sqrt{N_{\text{photons}}}}{N_{\text{photons}}} \lambda_{\text{laser}} \quad (1.3.3)$$

where N_{photons} is the number of photons expected to arrive in some time interval t . Once again, it is only useful to consider light collected over a time period on the order of the period of the incident gravitational wave, $t \sim \lambda_{\text{GW}}/c$. The number of photons arriving in a time period t is

$$N_{\text{photons}} = \frac{P_{\text{laser}}}{hc/\lambda_{\text{laser}}} \frac{\lambda_{\text{GW}}}{c} = \frac{P_{\text{laser}} \lambda_{\text{laser}} \lambda_{\text{GW}}}{hc^2} \quad (1.3.4)$$

where P_{laser} is the laser power and $hc/\lambda_{\text{laser}}$ is the energy of each photon. For a laser power of 1 W, $N_{\text{photons}} \sim 10^{18}$, which means LIGO would be sensitive to a strain of

$$h \sim \frac{\Delta L}{L_{\text{effective}}} \sim \frac{\sqrt{N_{\text{photons}}}}{N_{\text{photons}}} \frac{\lambda_{\text{laser}}}{\lambda_{\text{GW}}} \sim \frac{1}{10^9} \frac{10^{-6} \text{ m}}{10^6 \text{ m}} \sim 10^{-21} . \quad (1.3.5)$$

We can get even better sensitivity by increasing the effective power of the laser. This is done by using a power recycling cavity, discussed in more detail below. In addition, Advanced LIGO will make use of a signal recycling cavity, giving an even greater boost to sensitivity.

1.3.2 Main components of LIGO

As described above, LIGO must be more than just a simple Michelson interferometer in order to achieve the desired sensitivity. Initial LIGO was actually a power-recycled, Fabry-Perot, Michelson interferometer, and Advanced LIGO will be a signal-recycled, power-recycled, Fabry-Perot, Michelson interferometer. Each of the components of the interferometer are briefly described below, and a more detailed discussion can be found in, for example, Abbott et al. (2009) or Creighton & Anderson (2011).

Michelson interferometer

A Michelson interferometer consists of a laser, a beamsplitter, one mirror at the end of each arm, and a photodiode, as diagramed in Fig. 5. The laser light travels towards

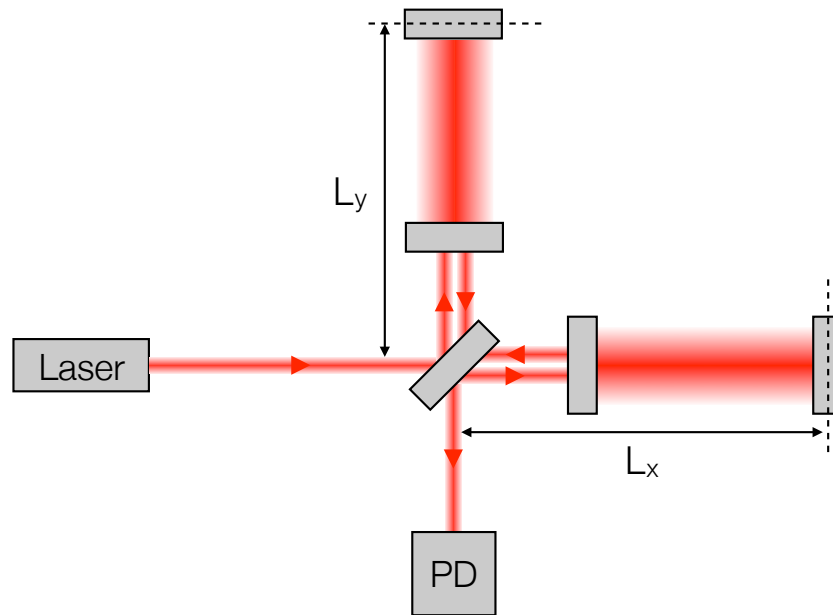


Figure 6 : LIGO contains a Fabry-Perot cavity at the end of each arm of the Michelson interferometer. The end test masses of the Michelson interferometer are the input mirrors of the Fabry-Perot cavity.

the beamsplitter and then is split evenly down each arm of the interferometer towards the two end mirrors. The transmission direction through the beamsplitter is called the x -arm and the reflection direction is called the y -arm. The light is reflected off of the end mirrors back towards the beamsplitter where it recombines. The laser light combines symmetrically back towards the laser (the symmetric port) and anti-symmetrically towards the photodiode (the anti-symmetric port). Any relative change in length of the interferometer arms will manifest as a change in the recombined light.

A relative change in length of the interferometer arms can be caused by noise or by gravitational waves. The end mirrors within the Michelson interferometer are referred to as test masses. We are studying the effect of a gravitational wave on the mirrors in the same way discussed in Sec. 1.1.3 for freely-falling test masses. As was shown in Sec. 1.3.1, a reasonably sized Michelson interferometer alone would not be sensitive enough to changes in length caused by astrophysical gravitational waves.

Fabry-Perot cavity

A Fabry-Perot cavity contains two mirrors that form a cavity. Light incident on the input mirror circulates within the cavity for a certain number of bounces before exiting.

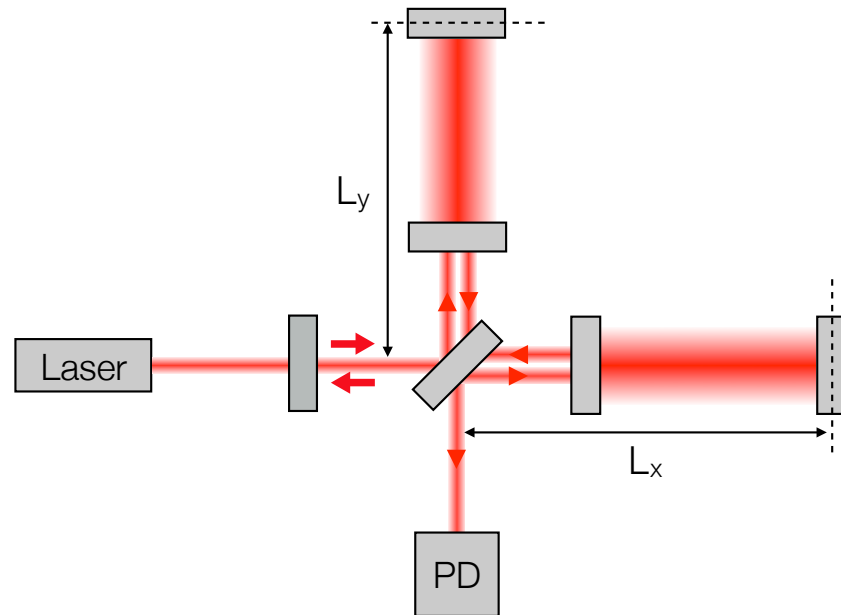


Figure 7 : A mirror is placed between the laser and the beamsplitter. Light exiting the interferometer at the symmetric port is recycled back into the interferometer. The result is to effectively increase the laser power used for the interferometer.

This amplifies the phase shift in the light exiting the cavity by a factor known as the arm cavity gain. LIGO contains a Fabry-Perot cavity at the end of each arm of the Michelson interferometer. The input mirrors of the Fabry-Perot cavity are the end mirrors of the Michelson interferometer. Fig. 6 diagrams the set-up of a Fabry-Perot, Michelson interferometer.

Power recycling cavity

Sec. 1.3.1 discussed the connection between LIGO's sensitivity to gravitational waves and the laser power. The effective laser power is increased in LIGO by using a power recycling cavity. A mirror is placed between the laser and the beamsplitter. This sends some of the light from the symmetric port of the interferometer back into the interferometer arms, which results in an increase in the light power in the arms and the beamsplitter. Fig. 7 shows a power-recycling, Fabry-Perot, Michelson interferometer.

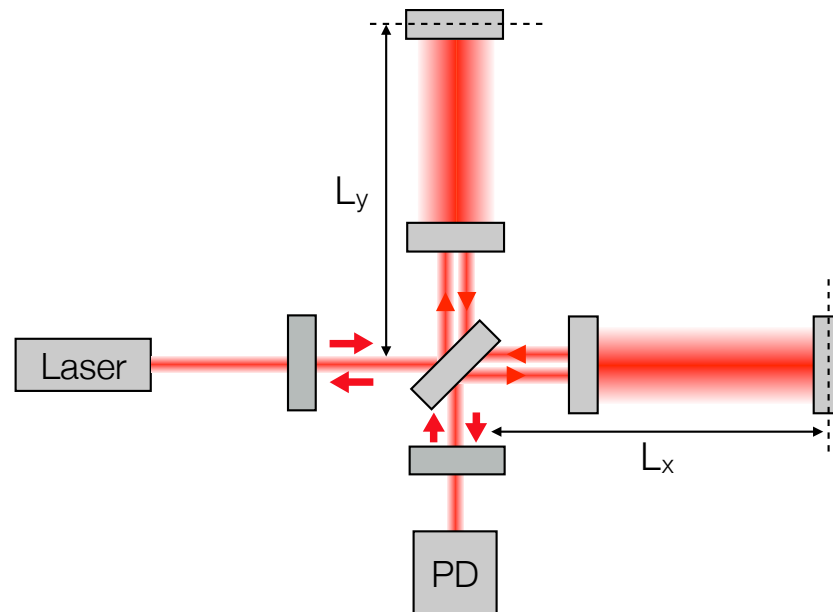


Figure 8 : A mirror is placed between the photodiode and the beamsplitter along the antisymmetric port. Light exiting the interferometer at the antisymmetric port is recycled back into the interferometer. The signal recycling cavity can be tuned to adjust the interferometer sensitivity within a certain bandwidth.

Signal recycling in aLIGO

Advanced LIGO incorporates an additional component in the interferometer known as the signal recycling cavity. A mirror is placed between the photodiode and the beamsplitter along the antisymmetric port, see Fig. 8. The length of the signal recycling cavity, which is the distance between the the signal recycling mirror and the beamsplitter, is tunable. Tuning the signal recycling cavity affects the bandwidth of the interferometer. The signal recycling cavity can be tuned to provide improved sensitivity at low frequencies, improved sensitivity at high frequencies, or improved sensitivity in a narrow frequency band.

1.3.3 Noise in the LIGO interferometers

LIGO's goal is to detect changes in the differential arm length caused by gravitational waves. However, the recorded strain by the photodiode of the interferometer contains both noise (non-gravitational-wave signals) as well as potential gravitational-wave signals. It is essential for the effort of extracting gravitational-wave signals from the data to understand the noise. The frequency-dependent noise in the LIGO interferometers is characterized by the noise amplitude spectral density, which is the square-root of the

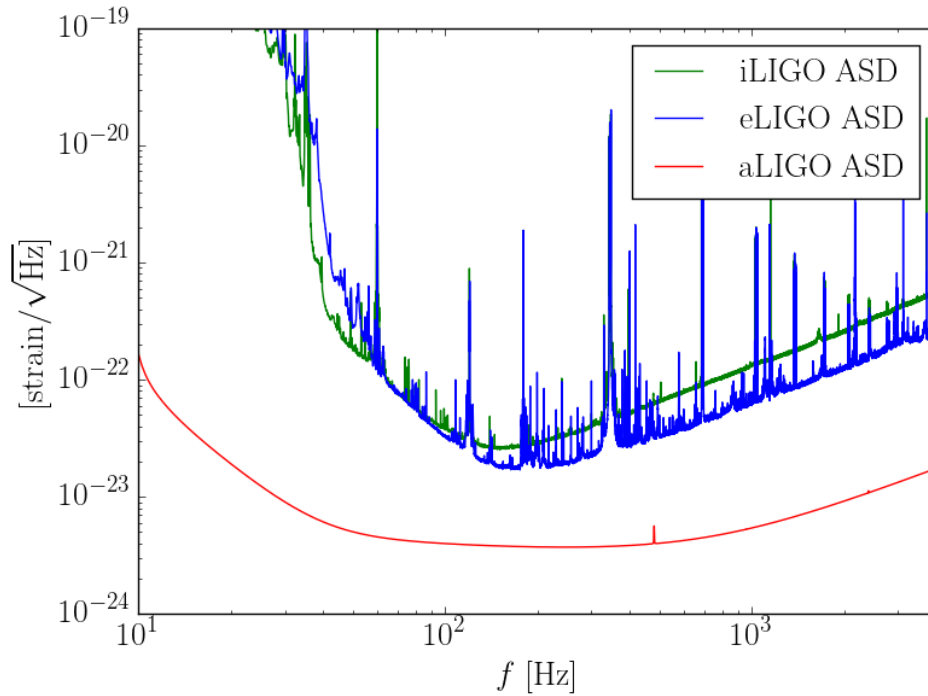


Figure 9 : The amplitude spectral density (ASD) for Initial LIGO (green curve), Enhanced LIGO (blue curve), and the anticipated ASD for Advanced LIGO at design sensitivity (red curve).

noise power spectral density. The noise power spectral density is the power spectral density of the strain read out by the interferometer in the presence of no gravitational-wave signal. (See Sec. 3.1.1 for a definition of power spectral density.) Fig. 9 shows the noise amplitude spectral density that was achieved in Initial LIGO and Enhanced LIGO and the anticipated Advanced LIGO noise amplitude spectral density.

There are three dominant components to the noise in the LIGO interferometers.

- **Seismic noise (low frequencies)** At low frequencies, the noise in LIGO is dominated by ground-based activity that couples to the interferometer end test masses. Ground-based activity changes the length of the interferometer arms by physically moving the end test masses. This noise includes everything from rush hour traffic to earthquakes to the vibration of a fan in the control room. We mitigate the seismic noise by dampening the motion of the end test masses through a system of pendulums. In Initial LIGO, the end test masses were suspended in a single pendulum system. In Advanced LIGO, we have improved the seismic isolation through the use of a quadruple pendulum system. Seismic noise dominated LIGO's noise at

frequencies below 40 Hz in Initial LIGO and should dominate at frequencies below 10 Hz in Advanced LIGO. 21

- **Thermal noise (mid frequencies)** The Brownian motion of molecules both in the end test masses and in the suspension wires changes the measured length of the interferometer arms. Since we are concerned with perturbations of spacetime on the sub-atomic particle scale, thermal noise is a relevant source of noise that limits our sensitivity in the mid-frequency region (10s of Hz to 100s of Hz). Advanced LIGO will mitigate thermal noise through the use of higher quality mirrors and suspension wires when compared to Initial LIGO.
- **Photon shot noise (high frequencies)** Photons arrive at the photodiode in a Poisson process, which leads to noise associated with the process of counting photons at the photodiode, as discussed in Sec. 1.3.1. This noise is known as “shot noise” and dominates LIGO’s noise at high frequencies.

This chapter has reviewed how gravitational waves can be detected using an interferometer by observing the strain $\Delta L/L$ induced on the interferometer from a gravitational wave. However, the output of the interferometer is not strain; the output is counts on a photodiode. The very first step in determining whether or not a gravitational-wave signal is present in LIGO data is converting the output of the detector into the physical quantity strain. This effort is known as calibration and will be discussed in Ch. 2.

Chapter 2

Calibration of the Advanced LIGO Instruments

*“Listen to the mustn’ts, child.
Listen to the don’ts. Listen to the
shouldn’ts, the impossibles, the
wont’s. Listen to the never haves,
then listen close to me... Anything
can happen, child. Anything can
be.”*

— Shel Silverstein, *Where the
Sidewalk Ends*

2.1 Introduction

The work described in this chapter is in close collaboration with Xavier Siemens and the aLIGO Calibration Team. This chapter closely follows Wade et al. (2014). The equivalent effort for Initial LIGO is described in detail in Siemens et al. (2004).

The starting point of all LIGO gravitational-wave searches is the strain—the fractional change in the length of the detector arms—caused by external sources including seismic and other noise along with gravitational-wave signals. The goal of the calibration is to provide an accurate reconstruction of the strain on the interferometer in the form of a time series $h_{\text{ext}}(t)$,

$$h_{\text{ext}}(t) = \frac{\Delta L_{\text{ext}}(t)}{L} \quad (2.1.1)$$

where $\Delta L_{\text{ext}}(t) = L_x(t) - L_y(t)$ is the length change of the x and y arms caused by

external sources, and L is the effective length of the unperturbed arms. See Fig. 8 and Sec. 1.3 for more information about the setup of the LIGO interferometers. Calibration is the essential first step in the analysis of gravitational-wave data. I am the lead of the low-latency time-domain calibration effort, which is a crucial component in LIGO's ability to rapidly send gravitational-wave event alerts to the astronomical community, and so for LIGO to fully participate as a facility for transient astronomy (Singer et al. 2014).

The LIGO interferometers are controlled with a set of multiple-input-multiple-output (MIMO) digital feedback loops. Calibration focuses on the differential arm (DARM) control loop and approximates it as single-input-single-output (SISO). A major calibration effort is performing measurements to construct accurate frequency-domain models for the various sub-systems within the DARM feedback loop. These tasks are often referred to as the “frequency-domain” calibration. The tasks involved in the “time-domain” calibration are the construction of digital filters from the frequency-domain responses and the deployment and maintenance of a pipeline that applies the appropriate filters to the error and control signals of the DARM loop to produce a time series for h_{ext} .

2.2 A brief description: LIGO length sensing and control system

A diagram of the DARM feedback loop is shown in Fig. 10. At low frequencies, the noise in the external strain is dominated by seismic activity. A control displacement ΔL_{ctrl} is applied to physically move the test masses in opposition of the external displacement ΔL_{ext} at low frequencies. Active feedback at the low frequencies is necessary to ensure that the interferometer stays in alignment. A residual high-frequency displacement ΔL_{res} remains.

The sensing function $\gamma(t)C$ turns the residual displacement into the digital error signal d_{err} . This function contains a slowly-varying time-dependent gain $\gamma(t)$ which depends on the amount of light stored in the Fabry-Perot cavities in each of the arms. The calculation of $\gamma(t)$ is discussed in Sec. 2.4. The sensing function is the frequency response

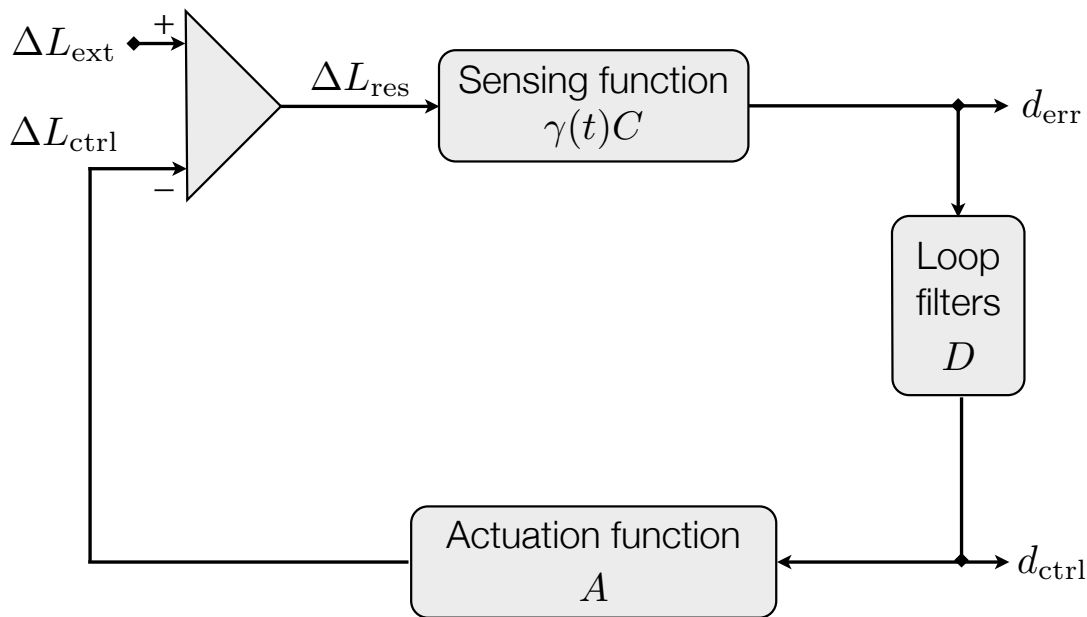


Figure 10 : The LIGO interferometers are kept in control through multiple digital feedback loops. A simplified diagram of the differential arm (DARM) length control loop, which is the focus of external strain calibration, is shown here.

of the Fabry-Perot cavity. The Fabry-Perot cavity is sensitive to oscillations in the cavity length with a period greater than the average light storage time in the cavity. The frequency dependence of the sensing function is given approximately by a real pole at around 400 Hz known as the cavity pole. The cavity pole is inversely proportional to the light storage time in the Fabry-Perot cavity. Within the feedback loop, a set of known digital filters D is applied to the error signal in order to produce the digital control signal d_{ctrl} . All digital filtering performed in the DARM loop is done in double floating-point precision. The actuation function A converts the digital control signal into the physical control displacement applied to the mirrors at the end of each arm. Each end test mass is suspended at the bottom of a quadruple pendulum and the control displacement is applied through actuators at each stage of the quadruple pendulum suspension system. The frequency dependence of the actuation function is given by the frequency response of the pendulum suspension systems.

The external displacement ΔL_{ext} is constructed from both the digital error signal d_{err} and the digital control signal d_{ctrl} . The result is then divided by the mean interferometer arm length L to obtain h_{ext} . In fact, ΔL_{ext} can be constructed from the digital error

signal alone, but it turns out to be useful to to construct ΔL_{ext} from both the error and control signals for reasons discussed in Sec. 2.4. Using the feedback loop shown in Fig. 10, we find

$$\begin{aligned}\Delta L_{\text{res}} &= \Delta L_{\text{ext}} - \Delta L_{\text{ctrl}} \\ d_{\text{err}} &= \gamma(t)C \Delta L_{\text{res}} \\ \Delta L_{\text{ctrl}} &= A d_{\text{ctrl}} .\end{aligned}$$

Combining the above equations gives,

$$\Delta L_{\text{ext}} = \frac{d_{\text{err}}}{\gamma(t)C} + A d_{\text{ctrl}} . \quad (2.2.1)$$

In the frequency domain, Eq. (2.2.1) is a simple multiplication, up to the tim-varying $\gamma(t)$. In the time domain, the time series d_{err} and d_{ctrl} need to be convolved with the appropriate digital filters. The sensing gain $\gamma(t)$ is more slowly varying than the decay time of the digital filter $1/C$, so we can just digitize the reference inverse sensing function $1/C$, convolve it with d_{err} , and divide the resulting time series by $\gamma(t)$. Written explicitly,

$$\Delta L_{\text{ext}}(t) \approx \frac{1}{\gamma(t)} \left[\frac{1}{C} * d_{\text{err}} \right] (t) + [A * d_{\text{ctrl}}] (t), \quad (2.2.2)$$

where A is the digitized actuation filter, and the convolution of the filter F with the time series $x(t)$ is defined as

$$[F * x] (t) = \int x(t')F(t - t')dt' . \quad (2.2.3)$$

The digitized filters A and $1/C$ are kept fixed for as long as they are deemed to accurately represent the appropriate components of the DARM loop. When the various instrument subsystems are no longer accurately represented by the reference measurements for the sensing and actuation filters, updated measurements are used to produce new digital filters.

In summary, frequency-domain calibration activities include performing careful hardware measurements to accurately determine the sensing function C and the actuation A . Time-domain calibration activities include accurate digitization of the actuation and the inverse sensing frequency-domain models, tracking of the time-dependent gain of the

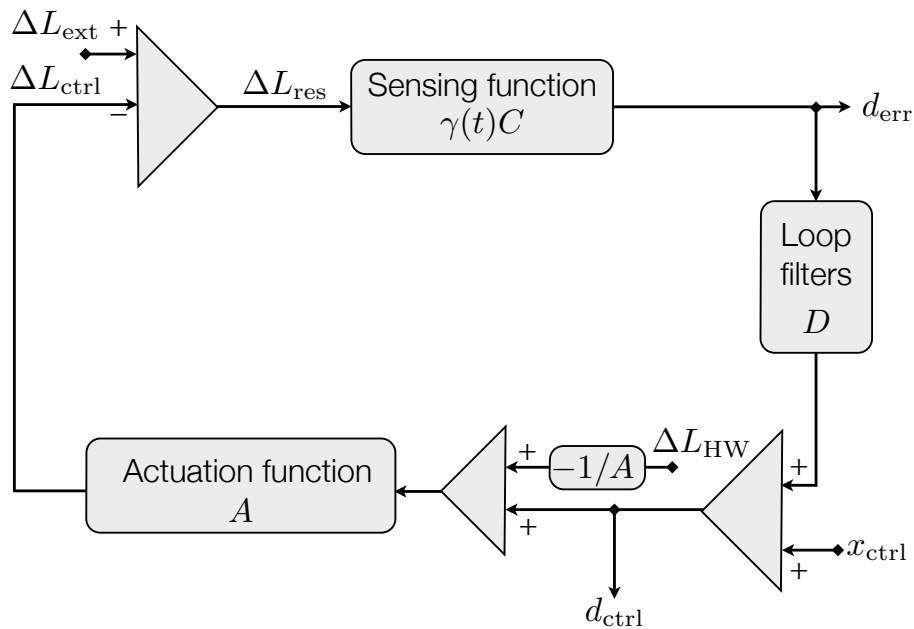


Figure 11 : Hardware injections are injected after the digital error signal is read out, since hardware injections should appear in the final product ΔL_{ext} . However, injections that should not appear in the final product ΔL_{ext} , such as with the injections used to calculate $\gamma(t)$, are injected before the digital error signal is read out.

sensing function, and applying the digitized filters along with the time-dependent sensing gain to the interferometer outputs to generate the external strain incident on the interferometer.

2.3 Injections and $h(t)$ construction

In order to commission the interferometer and test our ability to detect gravitational waves in the data, we often inject simulated signals into the interferometer. For example, we simulate gravitational-wave events appearing in our interferometer by introducing a strain modeled after a real gravitational-wave signal directly into the instrument. These are known as “hardware injections” and are used to study our ability to find simulated signals with our search pipelines (Thrane et al. 2014). We also perform other types of injections, such as sinusoidal injections at a set frequency, in order to study the interferometer response to a known input for commissioning. These types of injections are not of interest

to data analysts when searching for gravitational-wave events in the external strain.

Injecting into the DARM loop requires careful thought about the desired result of the injection. There is flexibility as to whether injections are placed before or after the digital control signal d_{ctrl} is read out. If the injection should appear in the final result ΔL_{ext} , such as with hardware injections used to test our astrophysical search pipelines, the injection should be done after d_{ctrl} is read out. If the injection should not appear in the final result ΔL_{ext} , such as the excitation channel x_{ctrl} used to calculate $\gamma(t)$ for calibration (see Sec. 2.4), it needs to be injected prior to where d_{ctrl} is read out.

The reason this flexibility exists is because the digital control signal d_{ctrl} is used in the construction of ΔL_{ext} . The details become clear when the excitation signal x_{ctrl} and the hardware injection signal ΔL_{HW} are included in the feedback loop (Fig. 11). The injected excitation signal x_{ctrl} is automatically incorporated appropriately into the calculation of ΔL_{ext} (Eq. (2.2.1)), since the digital control signal d_{ctrl} includes the excitation signal x_{ctrl} within it. However, the hardware injection signal ΔL_{HW} is not contained within d_{ctrl} since it is injected after d_{ctrl} is read out. Using Fig. 11, the true differential arm length caused by external sources should be

$$\begin{aligned}\Delta L_{\text{ext,true}} &= \frac{1}{\gamma(t)C} d_{\text{err}} + A d_{\text{ctrl}} + A \left(-\frac{1}{A} \Delta L_{\text{HW}} \right) \\ &= \frac{1}{\gamma(t)C} d_{\text{err}} + A d_{\text{ctrl}} - \Delta L_{\text{HW}} .\end{aligned}$$

Since Eq. (2.2.1) is used instead for ΔL_{ext} construction, the value reported for external displacement contains the hardware injection signal

$$\begin{aligned}\Delta L_{\text{ext,reported}} &= \frac{1}{\gamma(t)C} d_{\text{err}} + A d_{\text{ctrl}} \\ &= \Delta L_{\text{ext,true}} + \Delta L_{\text{HW}} .\end{aligned}$$

This is the desired results, since hardware injections are meant to appear in the external strain sent to data analysis pipelines.

The use of Eq. (2.2.1) for the construction of ΔL_{ext} allows any control signal, such as x_{ctrl} , that is injected prior to the digital control signal d_{ctrl} to be automatically accounted for in the determination of ΔL_{ext} . Any signal that should appear as part of the reported ΔL_{ext} should be injected after the digital control signal is read out.

2.4 Tracking slowly-varying, time-dependent changes in calibration, $\gamma(t)$ 28

The time-dependent gain of the sensing function $\gamma(t)$ can be measured by adding digital excitation signals x_{ctrl} into the DARM control loop. These excitations take the form of large amplitude sinusoids and are usually referred to as “calibration lines,” because of how they appear in the spectra of the DARM error and control signals.

From Fig. 11, it is possible to derive an expression for the time-dependent gain of the sensing function $\gamma(t)$ in terms of outputs of the interferometer. For this derivation, the hardware injections are ignored. The digital control signal can be expressed in terms of the digital error signal and the excitation signal,

$$d_{\text{ctrl}} = D d_{\text{err}} + x_{\text{ctrl}} .$$

At the injected line frequency f_c , the amplitude of the injected excitation is set to be much larger than the external displacement, meaning in the frequency domain the residual displacement is dominated by the injected signal $\Delta L_{\text{res}}(f_c) \approx -\Delta L_{\text{ctrl}}(f_c) = -A(f_c)d_{\text{ctrl}}(f_c)$. This means that for Fourier transforms of x_{ctrl} and d_{ctrl} centered at time t we can write

$$d_{\text{ctrl}}(f_c) \approx -D(f_c) \gamma(t) C(f_c) A(f_c) d_{\text{ctrl}}(f_c) + x_{\text{ctrl}}(f_c) , \quad (2.4.1)$$

which we can use to solve for $\gamma(t)$

$$\gamma(t) \approx \frac{1}{G(f_c)} \left(\frac{x_{\text{ctrl}}(f_c)}{d_{\text{ctrl}}(f_c)} - 1 \right) . \quad (2.4.2)$$

Here $G(f_c) \equiv D(f_c)C(f_c)A(f_c)$ is the open loop gain at the calibration line frequency. The sensing gain $\gamma(t)$ should always be real, up to noise contributions to ΔL_{res} . Departures of $\gamma(t)$ from being real-valued indicate that one or more of the DARM model components are not modeled correctly, and a check on the reality of $\gamma(t)$ is used to diagnose the fidelity of the calibration model.

The time-dependent gain of the sensing function $\gamma(t)$, also commonly known as the calibration factor, is calculated using Eq. (2.4.2). The digital control signal $d_{\text{ctrl}}(t)$ and the excitation signal $x_{\text{ctrl}}(t)$ are measured as time series. These time series need to be demodulated at the calibration line frequency of interest f_c . The demodulation is

accomplished by first applying a Hann window to one second of time series data centered at time t_0 and then taking a Fourier transform of the data at frequency f_c . The value of $x_{\text{ctrl}}(f_c; t_0)$ is given by

$$x_{\text{ctrl}}(f_c; t_0) = \sum_{j=-}^{N-1} w_j x_{\text{ctrl}} \left(t_0 - \frac{1}{2} N \Delta t + j \Delta t \right) e^{-2\pi i j \Delta t f_c} \quad (2.4.3)$$

where the Hann window

$$w_j = \frac{1}{2} \left[1 - \cos \left(\frac{2\pi j}{N-1} \right) \right], \quad (2.4.4)$$

$1/\Delta t$ is the sample rate, and $N\Delta t = 1$ second. The equations above are for the excitation signal, but the same transform is performed for the digital control signal. The open loop gain is measured as a function of frequency using swept sine measurements, and the open loop gain at the calibration line frequency is determined from these measurements. The digital control signal d_{ctrl} is whitened before being recorded as output of the interferometer. Therefore, within the calculation for $\gamma(t)$, the digital control signal must also be de-whitened at the calibration line frequency. The value of the whitening filter for d_{ctrl} is known. This provides all of the ingredients required to compute $\gamma(t_0)$. The Hann window is then shifted ahead in time by one sample and the calculation is repeated for $\gamma(t_0 + \Delta t)$. In this way $\gamma(t)$ is calculated on a sample-by-sample basis starting with a one second delay.

2.5 Constructing time domain FIR filters from the frequency domain models

We digitize the frequency domain models for the inverse sensing function $1/C$ and the actuation function A in order to compute $\Delta L_{\text{ext}}(t)$ (Eq. (2.2.2)). A lot of effort must first be put towards making accurate measurements of A and C in the frequency domain in order to produce reliable values for the external displacement. For more details on the frequency domain models for the sensing function and the actuation function see Kissel et al. (2014). The impulse response for the inverse sensing and actuation functions are nicely approximated with finite impulse response (FIR) filters. The rationale for using FIR filters in the reconstruction of the strain, as opposed to infinite impulse response

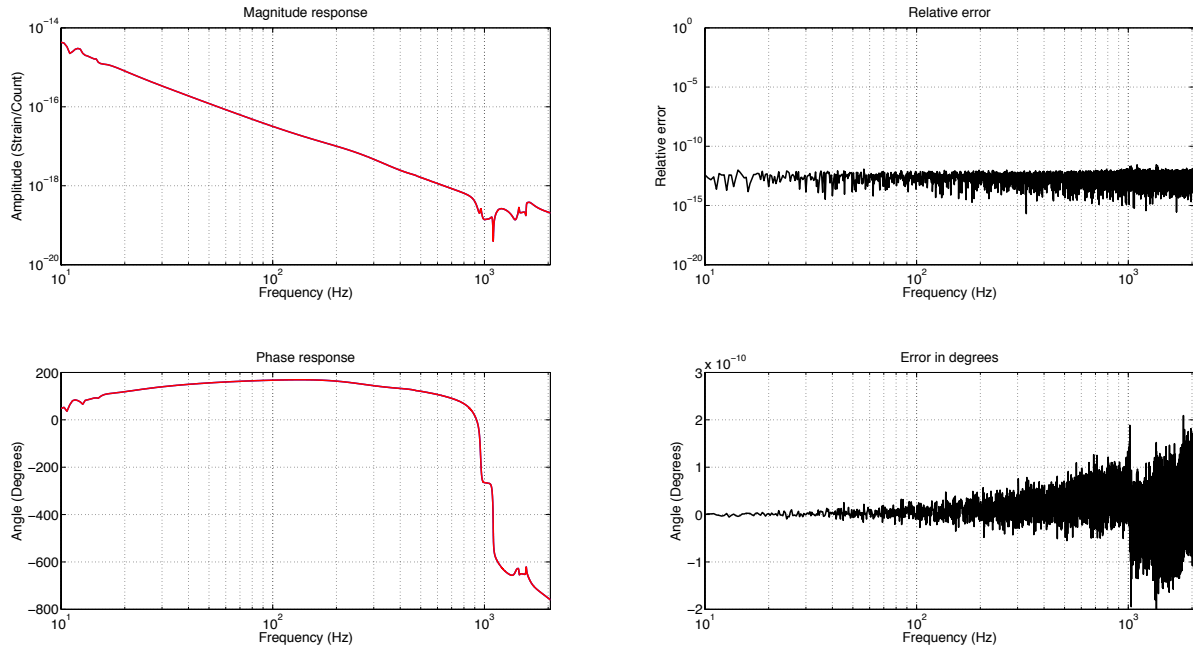


Figure 12 : The magnitude (top) and phase (bottom) response of the actuation FIR filter (blue) and the true frequency domain actuation model (red). The plots on the right indicate the relative error between the two models. The errors in magnitude and phase are essentially zero across all relevant frequencies, [10 Hz, 2048 Hz].

(IIR) filters, is two-fold. First, calibrated data often need to be re-calibrated with improved models. For example, in LIGO's fifth science run there were four revisions to the calibration which required re-calibration of the entire data set. Unlike IIR filters, FIR filters don't require storing a history, making re-calibration of the data set trivially parallelizable: all the data can be calibrated at once on a computing cluster provided the data is divided into segments with sufficiently long overlaps. Second, when data drop-outs occur, filling in the gaps of missing data is trivial with FIR filters: again, we just need sufficient overlap with existing calibrated data. To fill in a few second gap, say, of missing data with IIR filters would require re-calibrating much larger quantities of data because of the need for filter histories.

The inverse sensing function is nicely approximated using a short, one second filter, and it is calculated using the full data sample rate of 16384 Hz. However, the actuation function requires a longer \sim a few seconds filter to capture the behavior appropriately.

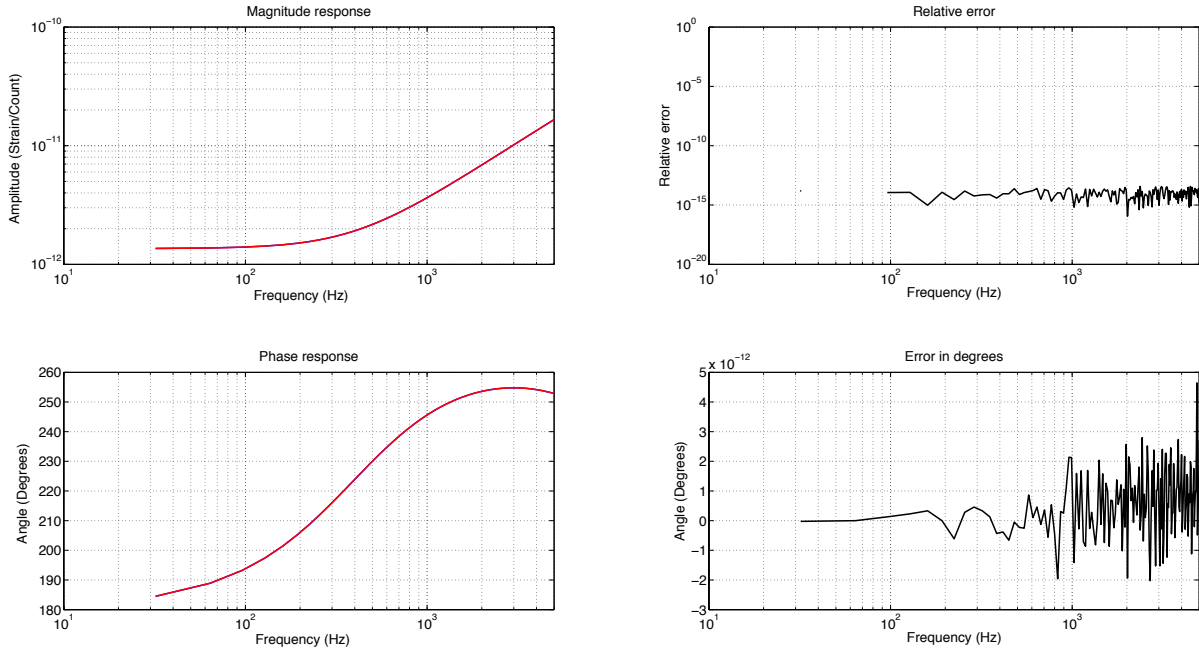


Figure 13 : The magnitude (top) and phase (bottom) response of the inverse sensing FIR filter (blue) and the true frequency domain inverse sensing model (red). The plots on the right indicate the relative error between the two models. The errors in magnitude and phase are less than 10^{-12} across the entire calibration frequency band, [10 Hz, 5000 Hz].

This is due to narrow frequency bandwidth notch filters, such as digital notch filters at the violin mode frequencies of the suspensions, in the actuation function that must be resolved using a long integration time. Since the actuation is only relevant for low frequencies and since it is a long filter, for computational speed-up the FIR filter for the actuation is computed at a lower sample rate of 4096 Hz. For both of these filters, we incorporate a high pass filter with a cutoff frequency of 10 Hz.

Frequency-domain calibration provides the transfer function for the sensing and the actuation. The FIR filters for inverse sensing and actuation are computed by simply taking the inverse Fourier transform of the frequency response of these transfer functions. To produce the actuation FIR filter, we

1. Find the frequency response of the actuation transfer function using a frequency vector that corresponds to the desired properties of the final FIR filter. For example, the frequency spacing is $df = 1/T$ where T is the duration of the FIR filter and the

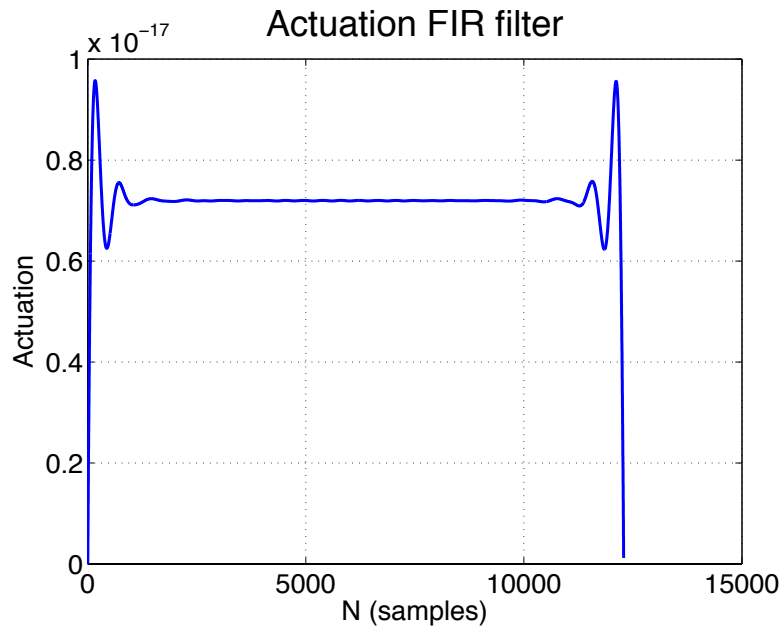


Figure 14 : The actuation FIR filter when no artificial delay is added. The filter is split across time.

Nyquist is chosen to be 2048 Hz.

2. Apply half of a Hann window that rolls off frequencies below 10 Hz to the frequency response.
3. Zero-out the Nyquist component of the frequency response.
4. Compute the inverse Fourier transform of the frequency response. The result is the desired FIR filter.

The resulting FIR filter from the above procedure is split across time, as shown in Fig. 14. We add an artificial delay to center the FIR filter in time. The resulting filter is shown in Fig. 15. This artificially delay must be undone by applying an advance during the filtering procedure.

The inverse sensing function FIR filter is computed in a similar manner. To produce the inverse sensing FIR filter, we

1. Find the frequency response of the sensing transfer function using a frequency vector that corresponds to the desired properties of the final FIR filter. Here, the Nyquist is chosen to be 8192 Hz, since d_{err} is filtered at the full sample rate of 16384 Hz.

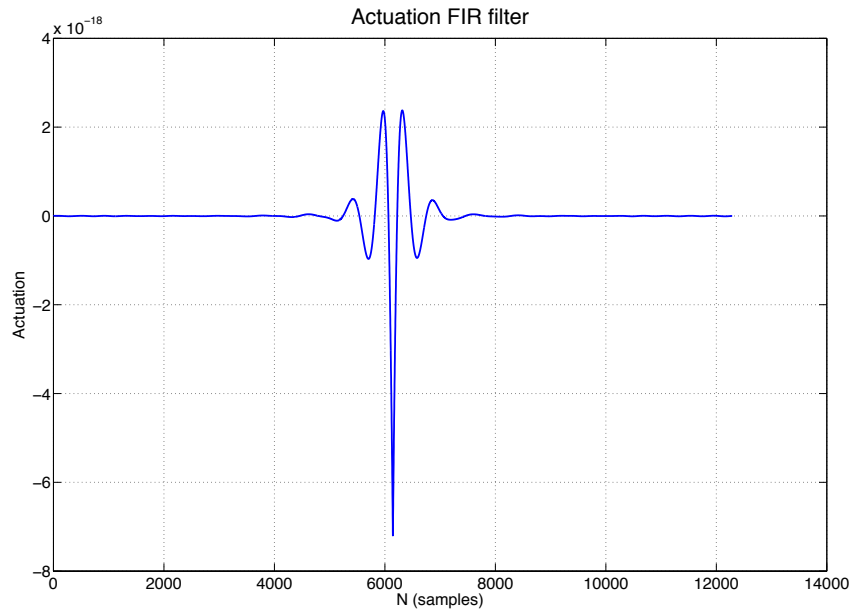


Figure 15 : The actuation FIR filter with an artificial delay added. The filter is centered in time.

2. Take the inverse of the frequency response to obtain the frequency response of the inverse sensing function.
3. Apply half of a Hann window that rolls off frequencies below 10 Hz.
4. Apply half of a Hann window that rolls off high frequencies (above ~ 6 kHz).
5. Zero-out the Nyquist component of the frequency response.
6. Compute the inverse Fourier transform of the frequency response. The result is the dies red FIR filter.

Just as with the actuation FIR filter, we add an artificial delay to center the filter in time. The inverse sensing function requires that an additional artificial delay be added in order to produce a physical filter. There is a delay in the sensing function due in part to the light-travel time in the cavities. When inverting the sensing function, this turns into an advance. Since an advance is unphysical, we must add an artificial delay to the inverse sensing function in order to construct the FIR filter. All of the artificial delays are removed by advancing the time series when the filter is applied to the error signal in the calibration pipeline.

The error and the control signals have a large dynamic range, and in order to avoid floating point precision errors when recording these channels, we whiten both the error and control signals before recording them. This whitening needs to be undone in the calibration pipeline. I produce FIR de-whitening filters in the same manner as described above. I digitize a zero, pole, gain model for the de-whitening filters by taking the inverse Fourier transform of the frequency response of the model.

Fig. 12 shows a comparison of the magnitude and phase response of the computed actuation FIR filter to the true frequency response of the actuation function. The errors in magnitude and phase are essentially zero across all relevant frequencies, [10 Hz, 2048 Hz]. Fig. 13 shows the same comparison in magnitude and phase for the inverse sensing filter. The errors in magnitude and phase are lower than 10^{-12} across the entire calibration frequency band, which is [10 Hz, 5000 Hz].

2.6 Time domain calibration pipeline

For aLIGO, two methods are being developed to construct $h_{\text{ext}}(t)$ in the time domain. The first method involves a low-latency pipeline that will be operated within the Data Monitoring Tool (DMT) at both the Hanford and Livingston interferometer sites. I lead the development of this method and will discuss it in detail below. The second method, which is currently under development, is implemented directly in the front-end of each interferometer producing $\Delta L_{\text{ext}}(t)$ as a raw data product in the same way the error and control signals are currently available.

2.6.1 gstlal calibration pipeline

Our goal is to produce $h_{\text{ext}}(t)$ in very low-latency. The low-latency pipeline that is operated within the DMT is written using a codebase known as `gstlal` (Cannon et al. 2014), which is a number of LIGO Algorithm Library (LAL) (LSC 2015) tools wrapped with `GStreamer`. `GStreamer` (GStreamer 2015) is a common audio and video streaming codebase which is optimized for the manipulation of data streams that need to be processed in real time. The primary motivation for low-latency generation of the strain is prompt data analysis and reporting of gravitational-wave events (from, say, binary neutron star

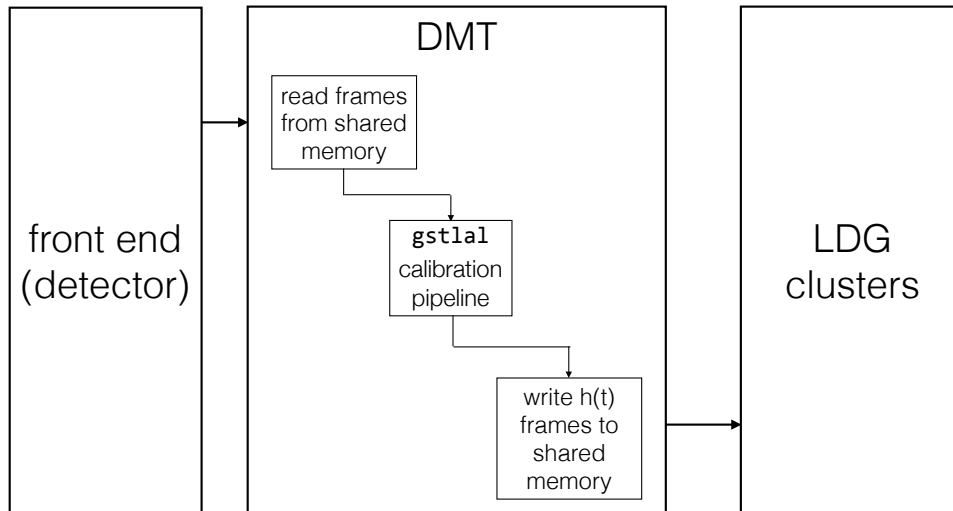


Figure 16 : Diagram of how the calibration pipeline fits into the low-latency data flow.

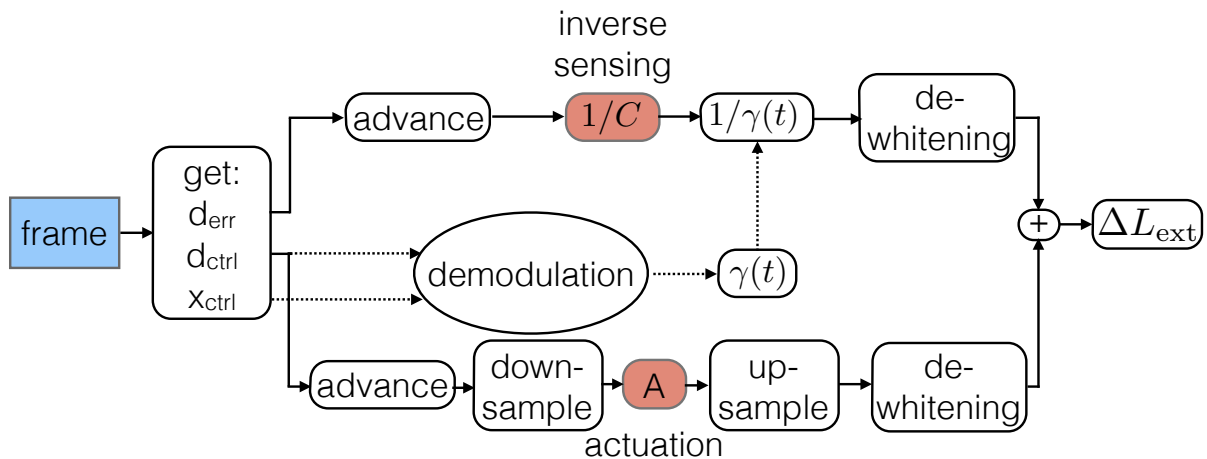


Figure 17 : Basic schematic of $h_{\text{ext}}(t)$ generation for the low-latency pipeline operated within the DMT.

mergers) for electromagnetic follow-up (Singer et al. 2014).

Fig. 16 shows how the calibration pipeline fits into the current low-latency data flow. The front-end of the instrument collects data that is broadcasted to the DMT in the “frame” packaging format. These frames are synced up to a shared memory partition on the DMT machine from which the calibration pipeline reads. The calibration pipeline writes the calibrated data back into frames into a new shared memory partition. This data is then sent to the various LIGO Data Grid (LDG) computing clusters. Full documentation of the low-latency data network can be found in (Zweizig & et al. 2014).

The procedure for computing $h_{\text{ext}}(t)$ in the time domain is shown in Fig. 17. The

pipeline begins by reading in data from a frame and extracting the necessary data channels: the error signal d_{err} , the control signal d_{ctrl} , and the excitation signal x_{ctrl} . The error signal d_{err} is first advanced to compensate for the delay that was added to the inverse sensing FIR filter (see Sec. 2.5), and then convolved with the inverse sensing filter. In parallel, $\gamma(t)$ is calculated as described in Sec. 2.4. The error signal is then divided by $\gamma(t)$ to produce the residual displacement. Also in parallel, the control signal d_{ctrl} is first advanced to compensate for the delay that was added to the actuation FIR filter (see Sec. 2.5), and then down-sampled from 16384 Hz to 4096 Hz. The actuation FIR filter can be long (several seconds) and down sampling is performed for computational efficiency. Since the control signal only contains the low frequency part of $h_{\text{ext}}(t)$, downsampling it and losing the high frequency information is not problematic. The down-sampled control signal is then convolved with the actuation FIR filter and resampled back up to 16384 Hz. The control and error signals in the DARM loop have large dynamic ranges and need to be whitened prior to being recorded in single floating-point precision. For the calibration, the control and error signals must therefore be de-whitened. This is done after the control signal has been filtered through the actuation and after the error signal has been filtered through the inverse sensing and multiplied by $1/\gamma(t)$. Finally, the filtered error and control signals are added together, producing $\Delta L_{\text{ext}}(t)$, and divided by the mean detector arm length L to form the external strain $h_{\text{ext}}(t)$. All of the filtering in this process is performed in the time domain to avoid latencies in h_{ext} production.

2.6.2 Calibration state vector

In addition to producing $h_{\text{ext}}(t)$, the `gst1a1` calibration pipeline also produces calibration state information. The pipeline outputs a bit-wise calibration state vector known as the `GDS-CALIB_STATE_VECTOR` where the populated bits are defined as follows:

- 0** : HOFT_OK: $h(t)$ calibration is okay
- 1** : SCIENCE_LOCKED: “science intent” bit is on and the instrument is locked
- 2** : LOCKED: instrument is locked
- 3** : HOFT_PROD: $h(t)$ is produced by the calibration pipeline

4 : FILTERS_OK: filters settled in

5 : GAMMA_OK: γ in expected range

A value of zero for a given bit means that the bit is “off” and a value of one means the bit is “on.” For example, if the zeroth bit is one then the calibration is considered okay.

The fifth bit is an indication of whether the real and/or imaginary parts of $\gamma(t)$ have strayed too far from one and zero, respectively. If this does occur, that indicates the calibration has incurred an error and should be reexamined. The fourth bit indicates whether or not the filters have been given an appropriate amount of time to settle in after a non-locked time period. If the detector has just locked, then the data for the first N seconds, where N is the length of the filter, should not be analyzed. This is because any glitchy data in the non-locked time period would be contaminating the first N seconds of $h(t)$. If the FILTERS_OK bit is turned on, that means the filters have been given the appropriate amount of time to settle in. The third bit is turned on if any output for $h(t)$ is produced by the pipeline. The value of the second bit, LOCKED, is determined from the Online Detector Characterization (ODC) state vector (Ballmer et al. 2012) that is read-in as a required input to the calibration pipeline. If the ODC vector indicates that the instrument is locked, then the second bit of GDS-CALIB_STATE_VECTOR will be turned on. The first bit, SCIENCE_LOCKED is also determined from the ODC state vector. If the first (“science intent”) AND second (“locked”) bits of the ODC state vector are turned on, then the SCIENCE_LOCKED bit of GDS-CALIB_STATE_VECTOR will be turned on. The “science intent” bit is a human-determined state of the instrument that indicates the instrument is in a mode that should be producing science-quality data.

The calibration is considered okay, and hence the zeroth bit would be recorded as “on”, if the criteria for bits 2-4 are met. The fifth bit, GAMMA_OK, being off does not imply the calibration is not acceptable. Instead, this situation should be treated as a data quality veto flag by data analysis pipelines. In addition, the first bit being off while the second bit is on indicates that the instrument is locked but not in “science intent” mode. Such a scenario does not preclude the calibration from being good, and therefore the first bit does not go into determining the overall state of the calibration. However, analysis pipelines should look for both the zeroth and first bit of GDS-CALIB_STATE_VECTOR to be

2.7 Engineering runs as tests of the calibration procedure

In order to prepare for the advanced detector era, the LIGO Scientific Collaboration has been conducting “engineering runs” that aim to test various aspects of the aLIGO infrastructure. These engineering runs begin with the production of h_{ext} , whether it be fake or real, and test the aLIGO infrastructure from transferring data to the appropriate computing sites all the way through searching the data for gravitational wave signals and preparing electromagnetic follow-up events.

Before the DARM loop was commissioned in the aLIGO interferometers, the `gstlal` calibration pipeline was exercised by producing fake strain data during the early aLIGO engineering runs, specifically during engineering runs 3 through 5 (ER3-ER5). During these earlier ERs the calibration procedure described throughout this document could not be implemented. However, the infrastructure surrounding the `gstlal` calibration pipeline was built-up and tested within the DMT machines during at this time. In the most recent engineering run (ER6), a full interferometer was commissioned at the LIGO Livingston Observatory (LLO). We were able to implement the actual calibration procedure described in Sec. 2.6 during ER6.

2.7.1 Early engineering runs (ER3-ER5)

During the early engineering runs for which the `gstlal` calibration pipeline participated (ER3-ER5), the pipeline produced fake strain data by recoloring data from one of the aLIGO subsystems. The infrastructure surrounding the `gstlal` calibration pipeline was built up and tested during these runs.

The recoloring process is outlined in the following manner:

1. The aLIGO subsystem data is read-in from frames and whitened. Whitening data is the process of removing any frequency dependence from the power spectral density.
 - (a) During ER3, this whitening was done adaptively. This means that the power spectral density (PSD) that was used to whiten the data was measured and

updated on the fly while the pipeline was running. This process hoped to remove undesirable line features in the PSD of the recolored data. However, this process was found to cause data quality issues, specifically the introduction of anti-line features in the recolored data's PSD.

(b) Due to the data quality issue mentioned above, the whitening scheme was adjusted for ER4 and ER5. In ER4 and ER5, the data was whitened using a fixed reference PSD that was taken during a known stable time for the relevant subsystem. The fixed whitening spectrum was smoothed to remove line features by taking the median of 32 samples on either side of each point in the PSD. Since the data is whitened using a fixed PSD, the data quality of the recolored fake strain can vary, sometimes significantly, when the real-time PSD of the relevant subsystem strays from the measured reference PSD.

2. The whitened data was resampled from its original sample rate (32768 Hz) to 16384 Hz.
3. The whitened data was recolored to match the aLIGO zero-detuned high power (ZDHP) PSD (Shoemaker 2009). Recoloring the data means frequency dependence was given to the PSD of the data.
4. The recolored data was labeled with the channel name `FAKE-STRAIN` and written to frames at a sample rate of 16384 Hz.

During ER3 and ER4, the aLIGO subsystem that was recolored was the pre-stabilized laser (PSL). During ER5, the aLIGO subsystem that was recolored was the input mode cleaner (IMC).

During these early engineering runs the reliability and stability of the `gst1a1` pipeline infrastructure was tested and improved. By ER5, the pipeline produced fake strain data in very low latency more than 99.9% of the time for the entire run.

h(t) comparisons

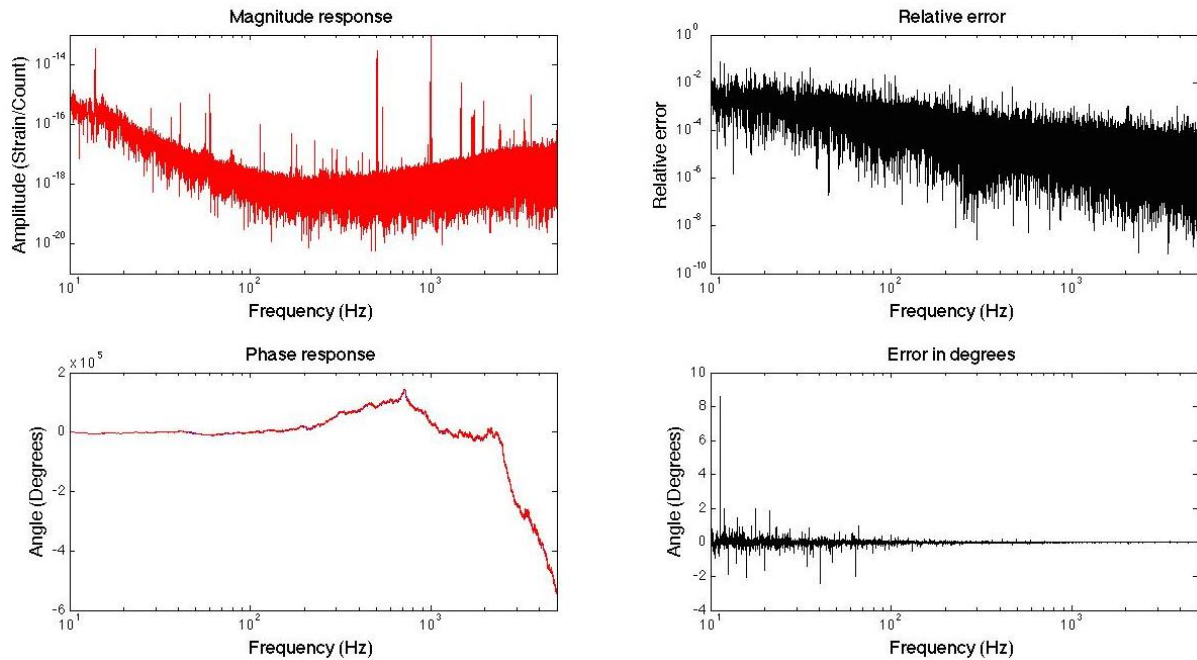


Figure 18 : Comparison in magnitude (top plots) and phase (bottom plots) of the `gstlal` calibration pipeline to a frequency domain calibration (Eq. (2.7.1)).

2.7.2 Recent engineering run (ER6)

In the most recent engineering run (ER6), there was a full interferometer commissioned at LLO. Since the LIGO Hanford Observatory (LHO) did not yet have a full interferometer, we still produced fake strain data as the LHO data stream. The `gstlal` pipeline produced real, calibrated $h_{\text{ext}}(t)$ data during ER6 at LLO. The procedure used for calibration is exactly that described in Sec. 2.6.1, except we artificially set $\gamma(t) = 1$ for the entire engineering run. We were able to produce calibrated data in near-real-time (~ 10 second latency) throughout the entire engineering run. During ER6 we were able to identify several errors in the FIR filter generation procedure and the `gstlal` calibration pipeline. Upon fixing these errors, the time domain calibration agreed to better than 1% in amplitude and 2 degrees in phase with a frequency domain calibration. The frequency domain calibration was computed by Fourier transforming a stretch of d_{err} and d_{ctrl} data, multiplying these by the inverse sensing and actuation function frequency

responses, respectively, adding the result of each multiplication, and dividing by L ,

$$h_{\text{ext}}(f) = \left(d_{\text{ctrl}}(f) A(f) + \frac{d_{\text{err}}(f)}{C(f)} \right) \frac{1}{L}, \quad (2.7.1)$$

taking $\gamma(t) = 1$. Fig. 18 shows a comparison of the frequency domain calibration to the `gstlal` calibration pipeline output. The segment of the strain produced by the `gstlal` calibration pipeline is Fourier transformed for comparison to the frequency domain calibration. If the frequency domain calibration is taken to be the true calibration, the time domain calibration procedure introduces errors of less than 1% in amplitude and 2 degrees in phase across the whole frequency band. This is well within the promised errors for calibration for ER6. However, the complete calibration errors include both the time-domain errors and the errors accrued by inaccuracies of the frequency-domain models. The calculation of the frequency-domain model errors is part of the frequency-domain calibration effort.

2.8 Conclusions

Time-domain calibration provides the transition step between data acquisition at the instrument level and analysis of this data for astrophysical signals. The time-domain calibration process takes in raw instrument data and models of the instrument behavior to produce a time series of the external strain incident on the detector. The first step in the calibration procedure is to make accurate measurements of the relevant instrument parameters and to model each of the relevant subsystems. Detailed discussions of measurement techniques and required models can be found in (Kissel et al. 2014), and a brief discussion of the models can also be found in Sec. 2.2. In addition to modeling the relevant subsystems, the calibration process must track the time-dependent gain of the sensing function, as discussed in Sec. 2.4.

Once measurements are made and models are developed, then the time-domain calibration process can begin. The first step in the time-domain calibration process is to make FIR filters out of the actuation and sensing function models. These FIR filters are quite accurate to the true models, as shown in Sec. 2.5. The time-domain calibration is

currently performed with a `gstlal` based pipeline that is discussed in Sec. 2.6.1. However, a method to perform time domain calibration in the front-end of the interferometer is also under development.

The calibration team has been heavily involved in the LIGO engineering runs, and the `gstlal` calibration pipeline has produced the fake strain data for the third through fifth engineering runs and real calibrated strain data at LLO during the sixth engineering run. We have improved the `gstlal` calibration low-latency infrastructure to better than 99.9% reliability. During the sixth engineering run we were able to test the full accuracy of the time domain calibration for the first time at LLO, and we found accuracies of better than 1% in amplitude and 2 degrees in phase. The errors do not account for the errors associated with the frequency-domain models.

Looking forward to the seventh engineering run and the first official observing runs, we will continue to investigate the major sources of error in the time-domain calibration procedure. We will commission and test the implementation of the $\gamma(t)$ calculation in the `gstlal` calibration pipeline, and we will develop an infrastructure for ensuring the FIR filters for the actuation and inverse sensing are automatically updated in real time when models within the front-end are adjusted.

Calibration is a critical step towards the discovery of gravitational waves. Once the external strain $h_{\text{ext}}(t)$ is constructed, it can then be passed to data analysis pipelines and searched for gravitational-wave events. Ch. 3 picks up where calibration leaves off and discusses how we search for gravitational waves from compact binary coalescence events in LIGO data.

Chapter 3

Search for sub-solar mass binary systems in Initial LIGO data

“Then he looked beyond the thornbushes, out into the big dark night. Nothing could be farther than the sky.”

— Little Nutbrown Hare, *Guess How Much I Love You* by Sam McBratney

3.1 Introduction

Through calibration (see Ch. 2), we construct the external strain incident on the LIGO detectors. The external strain $s(t)$ contains both noise $n(t)$ and, potentially, a gravitational-wave signal $h(t)$,¹

$$s(t) = n(t) + h(t) .$$

The process of searching for gravitational waves in LIGO data is the process of determining the probability that there is a signal buried in the noise. The most promising source for gravitational waves in LIGO is compact binary coalescence (CBC) events. As discussed in Sec. 1.2, the CBC gravitational-wave strain is well-modeled using the post-Newtonian formalism.

¹In the previous chapter, external strain was denoted $h_{\text{ext}}(t)$. Here, to agree with standard conventions, it will be denoted $s(t)$.

Since a search for CBC signals involves a well-defined model for the gravitational-wave strain, these searches can employ the optimal detection statistic, which is a statistic that quantifies the probability that the data $s(t)$ contains the signal model $h(t)$. The optimal detection statistic is the odds ratio, which is the ratio of the probability that there is a signal in the data to the probability that there is just noise in the data. Using Bayes theorem, the odds ratio is found to be proportional to the likelihood ratio (Creighton & Anderson 2011),

$$\Lambda(H_1|s) = \frac{p(s|H_1)}{p(s|H_0)} \quad (3.1.1)$$

where H_1 is the alternative hypothesis stating that there is a signal in the data and H_0 is the null hypothesis stating that there is just noise in the data. The notation $p(A|B)$ refers to the probability density that A is true given B .

3.1.1 Matched filter statistic

This section follows the discussion found in Chapter 7 of Creighton & Anderson (2011) and Allen et al. (2012). Assuming the noise in the LIGO detectors is stationary and Gaussian, the probability of obtaining a data set $n(t)$ is

$$p[n(t)] \propto e^{-(n,n)/2} \quad (3.1.2)$$

where the noise weighted inner product (a, b) is defined

$$(a, b) = 2 \int_{-\infty}^{\infty} \frac{\tilde{a}(f)\tilde{b}^*(f)}{S_n(|f|)} df$$

and $S_n(f)$ is the one-sided power spectral density of the noise n . The power spectral density (PSD) characterizes how much power the data set contains in each frequency component and is often defined in terms of the frequency components of the data set

$$\langle \tilde{n}^*(f')\tilde{n}(f) \rangle = \frac{1}{2} S_n(|f|)\delta(f - f') .$$

The square root of the PSD, known as the amplitude spectral density (ASD), for Initial, Enhanced, and Advanced LIGO is shown in Fig. 9.

For stationary, Gaussian noise, the likelihood ratio can be expressed in terms of exponentials of the noise weighted inner product,

$$\begin{aligned}\Lambda(H_1|s) &= \frac{p[s(t) - h(t)]}{p[s(t)]} \\ &= \frac{e^{-(s-h, s-h)/2}}{e^{-(s,s)/2}} \\ &= e^{(s,h)} e^{-(h,h)/2},\end{aligned}$$

where h is the true signal in the data. The only term in the likelihood ratio that depends on the strain data $s(t)$ is the noise weighted inner product of the strain data $s(t)$ with the signal $h(t)$. Since the likelihood ratio, and therefore the odds ratio, is a monotonically increasing function of the inner product (s, h) , then (s, h) is the optimal detection statistic for stationary, Gaussian noise. This optimal detection statistic is called the matched filter statistic,

$$(s, h) = 2 \int_{-\infty}^{\infty} \frac{\tilde{s}(f)\tilde{h}^*(f)}{S_n(|f|)} df. \quad (3.1.3)$$

A normalized version of the matched filter statistic is often called the signal-to-noise ratio (SNR),

$$\rho = \frac{(s, h)}{\sigma}, \quad (3.1.4)$$

where σ^2 is the variance of the matched filter, which can be shown to be (h, h) (Creighton & Anderson 2011). The SNR characterizes the strength of the signal h in the data for given noise $S_n(f)$. Since the SNR can be constructed from the matched filter statistic, we often refer to the SNR as the optimal detection statistic for stationary, Gaussian noise.

3.1.2 Maximum likelihood statistic

In reality, we do not know the true signal in the data. We have a model for the signal that is a function of parameters, such as binary component masses, termination time, and termination phase. The true parameters are unknown. Instead of using the likelihood statistic as described above, we need to use the maximum likelihood statistic, which is the likelihood, or SNR, maximized over the signal model parameters. The process for maximizing the SNR involves several steps. We seek to maximize the SNR over an unknown signal amplitude, termination time and phase, and intrinsic source parameters,

such as binary component masses. The overall unknown signal amplitude A is actually not of great interest in the search procedure, but it can be solved for given the maximized SNR and the variance of the matched filter statistic σ^2 (Creighton & Anderson 2011). Conventionally, we normalize the signal models and refer to the normalized signal model as a “template,” $h_{\text{mod}}(t) = A m(t)$ where $m(t)$ is the normalized template. We actually compute the matched filter statistic of the data with the normalized template.

Recall from Sec. 1.2 the form of the CBC signal model is

$$h(t) = -\frac{GM}{c^2 D_{\text{eff}}} \left[\frac{c^3(t_0 - t)}{5GM} \right]^{-1/4} \cos \left(2\phi_0 - 2 \left[\frac{c^3(t_0 - t)}{5GM} \right]^{5/8} \right) \quad (3.1.5)$$

where $\mathcal{M} = (m_1 m_2)^{3/5} / (m_1 + m_2)^{1/5}$ is the chirp mass, t_0 is the termination time, ϕ_0 is the termination phase, and D_{eff} is the effective distance. The effective distance is the distance to the source scaled by the binary orientation. The template $m(t)$ is a normalized version of Eq. (3.1.5). Since the termination phase appears in a cosine argument, a rotation of the template by $\pi/2$ in the frequency domain can be expressed as $\tilde{m}(f; 2\phi_0 \rightarrow 2\phi_0 - \pi/2) = \tilde{m}(f)e^{i\pi/2} = i\tilde{m}(f)$ for $f > 0$. It is therefore efficient to maximize the SNR over the unknown termination phase by forming a complex matched filter

$$z = x + iy = 4 \int_0^\infty \frac{\tilde{s}(f)\tilde{m}^*(f)}{S_n(f)} df . \quad (3.1.6)$$

x and y form an orthogonal basis for the template in the termination phase space. The quadrature sum of x and y therefore maximizes the SNR over the unknown termination phase,

$$\rho = \frac{|z|}{\sigma} . \quad (3.1.7)$$

In addition to the unknown termination phase, the signal model also contains an unknown termination time t_0 per Eq. (3.1.5). We take our templates m as a function of $t - t_0$ and seek to maximize the SNR over t_0 . In the frequency domain, $m(t - t_0)$ takes the form $\tilde{m}(f) e^{-2\pi i f t_0}$, which means the complex matched filter statistic becomes

$$z(t_0) = 4 \int_0^\infty \frac{\tilde{s}(f)\tilde{m}^*(f)}{S_n(f)} e^{2\pi i f t_0} df . \quad (3.1.8)$$

We parameterize the matched filter in terms of termination time t and compute a time series for the complex matched filter statistic $z(t)$ for all possible termination times,

$$z(t) = 4 \int_0^\infty \frac{\tilde{s}(f)\tilde{m}^*(f)}{S_n(f)} e^{2\pi i f t} df . \quad (3.1.9)$$

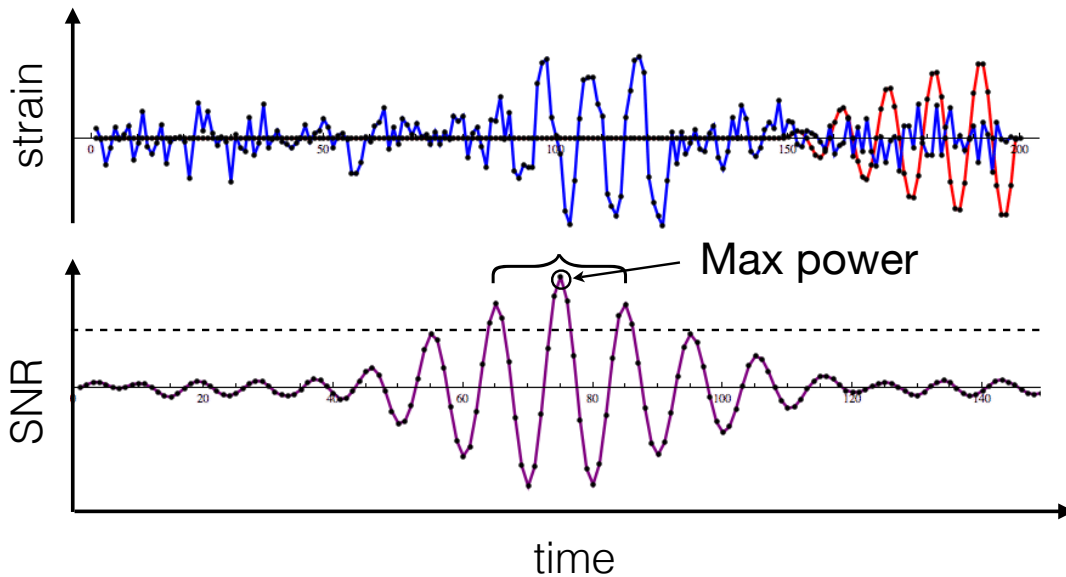


Figure 19 : An illustration of an SNR time series (bottom plot) given Gaussian data plus a signal (blue) for a given template (red) (top plot). Note that the signal is grossly exaggerated in the data for illustrative purposes. Imagine the template has swept across this data segment to produce the SNR time series. The horizontal dashed line on the bottom plot represents the SNR threshold, where events above this threshold are potential triggers. Local peak finding determines the trigger and the estimated arrival time for this trigger. This figure is credit of Leslie Wade.

Since the SNR is a normalized matched filter, this is equivalent to computing an SNR time series $\rho(t) = |z(t)|/\sigma$. The SNR is maximized over termination time using local peak finding of the SNR time series. This completes the maximization over termination time and phase.

The SNR still needs to be maximized over the remaining signal parameters, such as binary component masses. This is done through the use of a template bank. The relevant parameter space is gridded up and a template is calculated at each point on the grid. The coarseness of the grid is determined such that any possible real signal will produce an SNR with at least one template that is greater than or equal to a number known as the minimal match (Owen & Sathyaprakash 1999). The minimal match is typically chosen to be around 0.97, which means no more than 3% of SNR is lost due to the coarseness of the template bank.

Once a template bank is constructed, an SNR time series is computed for each of the templates. The resulting bank of SNR time series are used to determine potential signal candidates, or “triggers.” All points in the SNR time series that cross a pre-determined

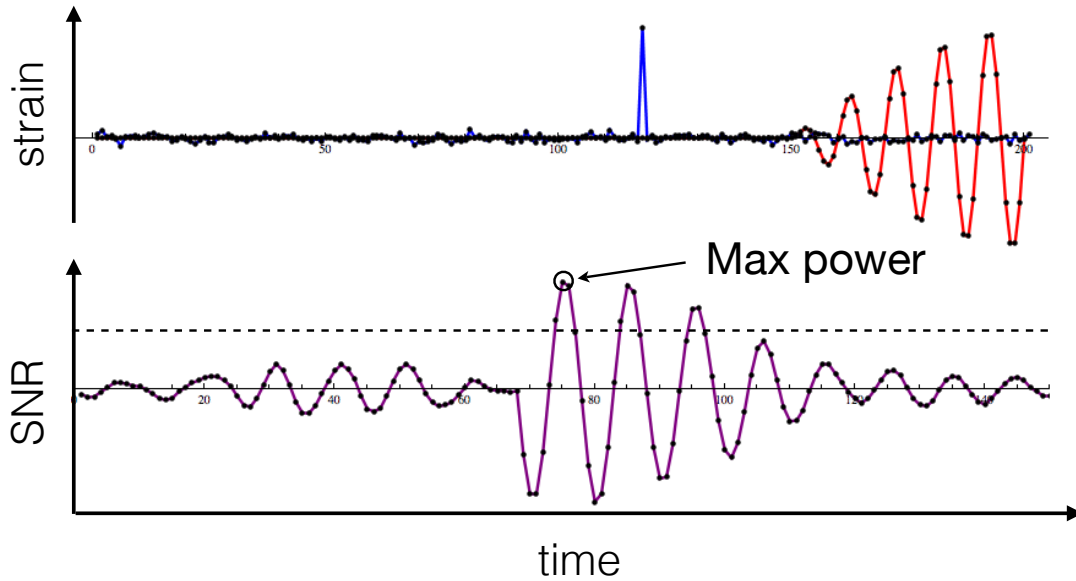


Figure 20 : An illustration of an SNR time series (bottom plot) given data (blue) that includes a large glitch (top plot). Imagine the template (red) has swept across this data segment to produce the SNR time series. The horizontal dashed line on the bottom plot represents the SNR threshold, where events above this threshold are potential triggers. Local peak finding determines the trigger and the estimated arrival time for this trigger. This figure is credit of Leslie Wade.

threshold are stored. Local peak finding is then performed across all stored SNRs within a given time window. The peak SNR value is recorded as a trigger at the peak time t_{peak} . Fig. 19 illustrates the procedure of peak finding in an SNR time series.

3.1.3 Non-stationary, non-Gaussian noise

In reality, the LIGO noise is neither stationary nor Gaussian. Examples of non-stationary noise include certain types of seismic noise, such as the human-related noise associated with rush hour traffic, trains passing nearby, earthquakes, logging, and much more. In order to combat the fact that our noise is not stationary, the power spectral density (PSD) is recomputed over time periods that are short compared to the time-evolution of the noise.

The LIGO noise is also not Gaussian and contains transient noise events (“glitches”) caused by, for example, seismic excitations. We combat the non-Gaussianity of the noise using several methods. First, we flag times in the data that should be vetoed based on data quality tests. The types of vetoes are described in Secs. 3.3 and 4.5. Any triggers that emerge during these times are automatically assumed to be noise events.

In addition, triggers are determined for each detector separately, and the final step in determining signal candidates is to perform a test for coincidence across detectors. A true gravitational wave will appear in each detector within a light-travel-time between the detectors. Not only do triggers need to pass a time coincidence check, but they also must pass a template coincidence check, meaning that only triggers coincident in time across detectors *for the same template* are stored as potential signal candidates. These coincidence requirements effectively veto most glitches, since glitches are unlikely to be coincident across detectors. The rare coincident glitches are usually just a coincidence. However, such coincident coincidences can occur (tongue tied?), and therefore a χ^2 test is used as an additional discriminant.

Glitches will accumulate SNR over time (and frequency) in a different manner than signals. Figs. 19 and 20 illustrate what the SNR time series might look like for a signal vs. for a glitch. The χ^2 test quantifies how similar the SNR accumulation is to what it should be if the signal model is known to be in the data. A small value for χ^2 implies the SNR accumulation is consistent with the modeled signal existing in Gaussian noise. A large value for χ^2 indicates that there is a disagreement in the SNR accumulation with the expectation of the modeled signal in Gaussian noise. A large value for χ^2 indicates that the signal template does not accurately model what appears in the data. This could be caused by a transient event in the data or by an imperfect signal model.

The χ^2 statistic used in the search method we employ is the autocorrelation χ^2 statistic, which compares the SNR time series to the autocorrelation function of the signal model. The autocorrelation function is $\alpha(\tau) \equiv (m(t), m(t - \tau))$, and the autocorrelation χ^2 is

$$\chi_{\text{auto}}^2 = \int_{-T/2}^{T/2} |\rho(t - \tau) - A\alpha(\tau)|^2 d\tau \quad (3.1.10)$$

where T is a tunable parameter that relates to the degrees of freedom of the χ^2 statistic (Privitera 2014) and A is the maximum amplitude of the SNR time series. This is a computationally efficient version of the χ^2 statistic since all of the information necessary to compute this statistic has been previously computed while constructing the matched filter statistic and the template bank.

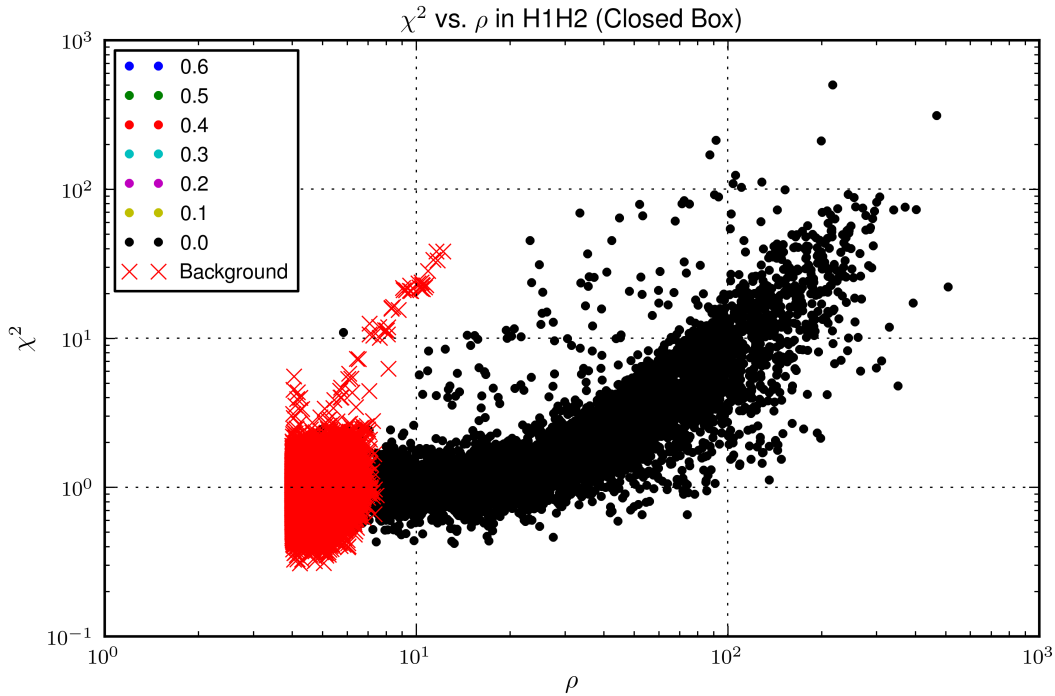


Figure 21 : The distribution of simulated gravitational wave events (injections) and noise events (background) in SNR - χ^2 space. The colored dots in the legend refer to values of spin. This plot is for a non-spinning search, so spin = 0.0. The χ^2 statistic allows for the separation of signals and background.

Through the use of both the SNR and the χ^2 statistics we are able to effectively determine the probability that a gravitational-wave signal exists in LIGO data. A true signal candidate would have a high value for SNR and a small value for χ^2 . We perform tests on our search pipeline by inserting simulated gravitational-wave signals (“injections”) into our data. Fig. 21 demonstrates how the injections separate from the noise events (“background”) in the χ^2 vs. SNR parameter space. Injections will have a range of SNRs, depending on the strength of the gravitational wave and will have a relatively small χ^2 . Signals with large SNR may have a large value for χ^2 due to the mismatch between template and signal, but similarly large SNR glitches will have much larger χ^2 values. Background noise events can also have a range of SNRs, including large values, but the χ^2 value for these events will increase with SNR. The louder a glitch appears in the data, the more pronounced the difference between the shape of the glitch and the shape of a real signal becomes.

3.2 Sub-solar mass binary search motivation

Extensive searches have already been conducted for binary neutron star (e.g. the LIGO Scientific Collaboration et al. (2012)), super-solar mass binary black hole (e.g. The LIGO Scientific Collaboration et al. (2013)), and neutron star – black hole (e.g. the LIGO Scientific Collaboration et al. (2012)) events in Initial LIGO data. The early science runs have also been searched for sub-solar mass binary events (Abbott et al. 2005). However, Initial LIGO’s fifth and sixth science runs have not yet been searched for sub-solar mass binary events. Along with my advisor and collaborators, Kipp Cannon and Chad Hanna, I conduct a search for sub-solar mass (SSM) binary events on one month of Initial LIGO’s fifth science run. The motivation for conducting this search is two fold: (1) There is the possibility for a detection of gravitational waves produced by binary coalescences of massive compact halo objects in this mass region, and (2) this search is computationally very similar in complexity to a search for binary neutron star events in Advanced LIGO data.

3.2.1 Astrophysical motivation

It is well known that dark matter is a large constituent of galactic halos based on measurements of galactic rotation curves (Trimble 1987). The nature of dark matter is currently an active area of research. The current most popular dark matter candidate is a weakly interacting massive particle (WIMP). Historically, massive compact halo objects (MACHOs) have been another enticing possibility for the composition of dark matter. The MACHO Collaboration were the first ones to put an upper limit on the existence of MACHOs in our galactic halo through microlensing of the Large Magellanic Cloud (LMC) (Alcock et al. 2000). The MACHO Collaboration determined that no more than 20% of the galactic halo was composed of MACHOs for their favored galactic halo model. The EROS and OGLE collaborations set even more restrictive upper limits on the existence of MACHOs in the galactic halo (Tisserand et al. 2007; Wyrzykowski et al. 2011). As a result, WIMPs has taken the lead as the most likely candidate for dark matter. However, no conclusive results have been found to support the existence of WIMPs and recent measurements of the galactic rotation curve indicates that the halo could be less massive

than originally believed (Sofue 2013; Bhattacharjee et al. 2014). Hawkins (2015) goes as far as arguing that we should no longer rule out an all-MACHO galactic halo in light of these recent results, and in fact the preferred halo model for quoting upper limits on the MACHO content of our halo may no longer be consistent with galactic rotation curve measurements. For the purpose of this dissertation, it is enough that the existence of MACHOs has not been entirely ruled out.

The most likely mass for MACHOs as determined by microlensing experiments is less than a solar mass, with the most probable mass lying around $0.2 M_{\odot}$ (Alcock et al. 2000; Tisserand et al. 2007; Wyrzykowski et al. 2011). The most likely candidate for sub-solar mass compact objects are primordial black holes. Black holes with masses less than a solar mass cannot form from stellar evolution. According to current theories, the most probable formation process for sub-solar mass black holes is from the collapse of quantum fluctuations in the early universe (Carr & Hawking 1974; Zel'Dovich & Novikov 1967). It is also possible that primordial black holes will have formed in binary systems. These primordial black hole binary systems are the target source for the SSM binary search discussed here.

The only existing direct upper limit on SSM binaries, independent of halo model, is $\mathcal{R} < 63 \text{ yr}^{-1} \text{ MWH}^{-1}$, set by LIGO (Abbott et al. 2005) after searching for SSM CBC signals in iLIGO's second science run (S2). In the absence of a detection, a search for SSM binaries in iLIGO's fifth science run (S5) will set a more restrictive upper limit due to both increased sensitivity of the detectors and increased observation time (≈ 1 year) when compared to S2.

During S5, there were three operational LIGO detectors. Two detectors were co-located in Hanford, WA. One of these detectors (H1) had 4 km arms and the other detector (H2) had 2 km arms. There was a third detector in Livingston, LA with 4 km arms (L1). One way we measure the sensitivity of each interferometer is to compute the horizon distance for a given CBC signal. The horizon distance is the distance at which an optimally oriented CBC system with some specified mass parameters would produce a signal with SNR of 8 in the detector. The estimated horizon distance for a $0.5 M_{\odot} - 0.5 M_{\odot}$ binary in S5 was about 6 Mpc for the least sensitive LIGO detector (H2) and 12 Mpc

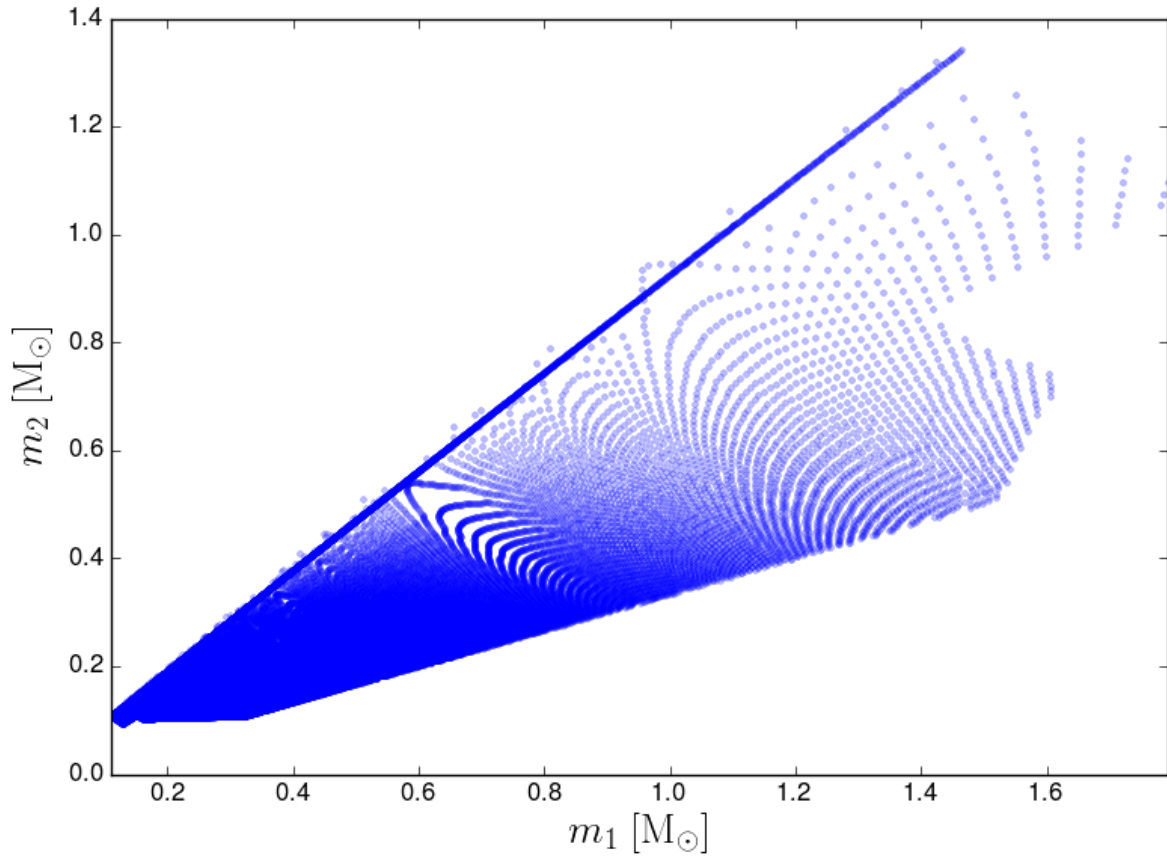


Figure 22 : Distribution of templates in the binary component mass space. Each dot indicates a template in the template bank.

for the two larger detectors (H1 and L1). These horizon distances probe other galaxy halos, beyond even our Local Group, which has not been done previously when searching for SSM binaries.

Since microlensing experiments place the most likely MACHO mass around $0.2 M_{\odot}$, we chose our template bank parameter space to extend down to $0.11 M_{\odot}$. We do not want to place the most probable mass on the edge of the template bank, but computational restraints prevent us from moving the lower mass cut off below $0.11 M_{\odot}$. In addition, LIGO has never searched for SSM – neutron star (NS) binary systems, so we chose to push the upper mass limit in our template bank up to $1.4 M_{\odot}$. However, such a template bank is too computationally expensive given current resources. We decide to restrict the mass ratios of the template bank to $[1 : 1, 3 : 1]$. This limits the size of the template bank while still allowing binaries that straddle the most probable mass of $0.2 M_{\odot}$ and includes

potential SSM – NS systems, such as a $0.5 M_{\odot} - 1.4M_{\odot}$ system.

Fig. 22 shows how the template bank is distributed in binary component masses. Some templates are placed beyond the mass limits discussed above. These templates are necessary in order to ensure the edge of the template bank has the desired minimal match. The chosen minimal match for this template bank was 0.93, rather than the typical 0.97. This was done so that the problem is computationally tractable within a graduate student’s lifetime, assuming 2015-era resources.

3.2.2 Computational motivation

An arguably more important justification than the astrophysical justification for a SSM binary search on S5 data is the technological similarities such a search holds to a binary neutron star (BNS) search in the advanced detector era. Binary neutron star systems are the most probable source for the first CBC detection (Abadie et al. 2010) and therefore viewed as a high priority search in aLIGO. The SSM binary search on S5 data will be conducted with the `gstlal_inspiral` pipeline from the `gstlal` software package (Cannon et al. 2014, 2012), which is poised to be the online low-latency CBC pipeline in aLIGO. Using this pipeline for an iLIGO SSM binary search will test its capability of performing a computationally intensive low-latency search. The iLIGO SSM binary search is an important proof-of-principle for aLIGO BNS searches at design sensitivity. We analyze the ability of the low-latency search software to produce prompt gravitational-wave events through the iLIGO SSM binary search.

Some of the technical similarities between a SSM S5 search and a BNS aLIGO search are the number of templates required in a template bank and the duration of signals in the LIGO sensitive frequency band. The number of templates N required for a template bank scales with the minimal match (MM), the minimum mass in the template bank, and the low frequency cut-off (Owen & Sathyaprakash 1999),

$$N \sim (1 - MM)^{-1} m_{\min}^{-8/3} f_{\min}^{-8/3}. \quad (3.2.1)$$

The low frequency cut-off is determined by the “seismic wall,” which refers to the sharp climb in seismic noise below a certain frequency. For iLIGO, the seismic wall occurred

at 40 Hz. Largely due to improved seismic isolation systems in aLIGO, the seismic wall should be pushed down to 10 Hz at aLIGO design sensitivity. Therefore, compared to an BNS iLIGO search, an aLIGO BNS search will require more templates per Eq. (3.2.1). Similarly, an iLIGO SSM search requires more templates than an iLIGO BNS search because of the lower minimum mass m_{\min} ($0.11 M_{\odot}$ rather than $1 M_{\odot}$).

In addition to requiring more templates in the template bank, lowering the low-frequency cut-off also increases the duration of signals in the LIGO sensitive frequency band. The duration of a CBC inspiral signal is given by the time until coalescence t_c , which is the time it takes the system to evolve from some starting frequency f_{\min} to infinity,

$$t_c = \frac{5}{256\eta} \frac{GM}{c^3} \left(\frac{\pi GM f_{\min}}{c^3} \right)^{-8/3}, \quad (3.2.2)$$

where $\eta = m_1 m_2 / M^2$ is the symmetric mass ratio and M is the total binary mass. The SSM search also has longer templates than the BNS search in iLIGO, again because of the lower minimum mass.

In summary, compared to an iLIGO BNS search, aLIGO BNS searches will require more templates and each template will be longer. These two effects are mimicked in an iLIGO SSM search. Even though the low frequency cut-off is 40 Hz, the lower masses in the template bank lead to a large number of templates required in the bank and longer template durations. Table 1 shows the comparison between an aLIGO BNS search and an iLIGO SSM search. For the astrophysical reasons discussed in Sec. 3.2.1 and computational feasibility, the iLIGO SSM template bank is chosen with a minimum mass of $0.11 M_{\odot}$ and mass ratios restricted to [1:1,3:1]. This template bank is also chosen because of its similarity to an aLIGO BNS template bank. Fig. 22 shows the distribution of templates across binary component mass space.

3.3 Coherent and null streams for co-located detectors

Since the two Hanford interferometers (H1 and H2) were co-located, it is possible to combine the data from the two interferometers into two new types of data streams: a coherent combination and a null combination (Creighton & Anderson 2011). The

	m_{\min}	m_{\max}	f_{\min}	q	MM	duration	# templates
aLIGO BNS	1.0 M_{\odot}	3.0 M_{\odot}	10 Hz	all	0.97	~ 30 mins	92,319
iLIGO SSM	0.11 M_{\odot}	1.4 M_{\odot}	40 Hz	[1 : 1, 3 : 1]	0.93	~ 30 mins	101,133

Table 1 : Comparison of iLIGO SSM search costs to aLIGO BNS search costs assuming the aLIGO zero-detuned high power noise spectrum (Shoemaker 2009). The minimum mass in the template bank m_{\min} and the low frequency cut-off f_{\min} are the main factors in dictating the number of templates required for a template bank with a given minimal match MM . The maximum mass in the template bank m_{\max} has a minimal effect on the required number of templates. In order to make an iLIGO SSM search with $m_{\min} = 0.11 M_{\odot}$ more feasible, we restrict the mass ratio q of the bank to be [1 : 1, 3 : 1]. We also show the duration that a signal with the minimum masses in each template bank would remain in the LIGO sensitive frequency band.

coherent combination is a sensitivity-weighted linear combination of the two individual interferometer data streams, and it contains noise along with any gravitational-wave signals,

$$\tilde{s}_{\text{coh}}(f) = \frac{\tilde{s}_{\text{H1}}(f)/S_{\text{H1}}(f) + \tilde{s}_{\text{H2}}/S_{\text{H2}}(f)}{1/S_{\text{H1}}(f) + 1/S_{\text{H2}}(f)}. \quad (3.3.1)$$

Note, this definition is normalized so that if $\tilde{s}_{\text{H1}} = \tilde{h}$ and $\tilde{s}_{\text{H2}} = \tilde{h}$ then $\tilde{s}_{\text{coh}} = \tilde{h}$. The PSD of the coherent combination is

$$S_{\text{coh}}^{-1} = \frac{1}{S_{\text{H1}}(f)} + \frac{1}{S_{\text{H2}}(f)}. \quad (3.3.2)$$

The coherent combination has the benefit of an improved sensitivity of about 10% over the more sensitive individual interferometer data stream. Fig. 23 shows the improved sensitivity of the coherent combination over the two individual interferometer data streams.

The null combination is a simple subtraction of the two data streams obtained from each individual interferometer,

$$s_{\text{null}}(t) = s_{\text{H1}}(t) - s_{\text{H2}}(t). \quad (3.3.3)$$

Since a gravitational wave will manifest in the same way in co-located interferometers, the null combination will contain no gravitational-wave signal. Therefore, the null combination can be used to veto large transient events that are only noise.

While it is possible to create coherent and null combinations for interferometers that are not co-located, the formation of these streams is more complicated and computationally expensive for such systems. For interferometers that are not co-located, the coherent

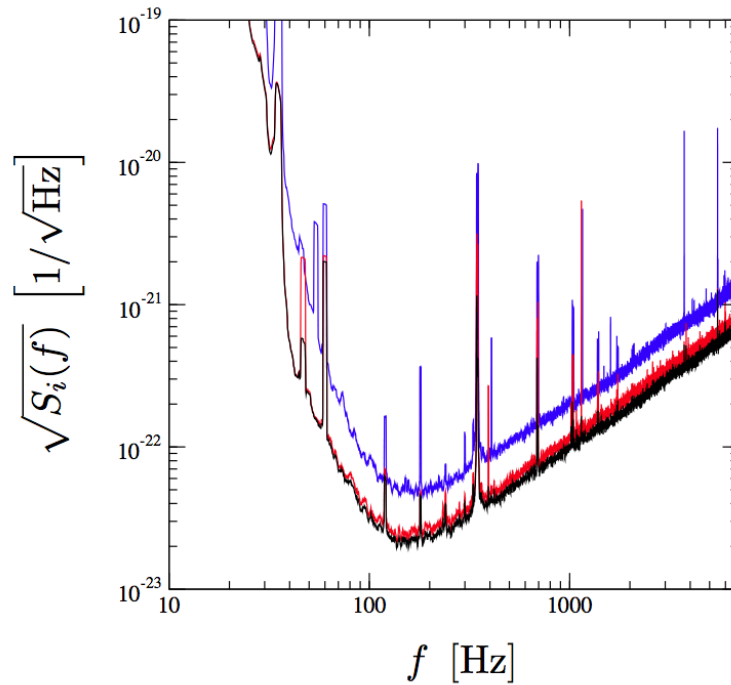


Figure 23 : The power spectral density $S(f)$, or noise, of the two individual Hanford interferometers, H1 (red) and H2 (blue), and the coherent combination (black), which is a linear combination of the two individual interferometer data streams. As the plot demonstrates, the coherent combination has better sensitivity (less noise) than the two individual interferometers by themselves. The coherent combination yields an improvement of about 10% over the H1 individual interferometer.

and null combinations are only produced when a sky position for the source of the gravitational wave is known to some degree (Creighton & Anderson 2011). Therefore, the coherent and null combinations are only used for the co-located Hanford detectors in our search and not for the network of Hanford and Livingston detectors.

For the SSM binary search, we search for gravitational waves using the coherent combination data stream instead of the individual H1 and H2 data streams. We are effectively treating H1 and H2 as a single instrument (H1H2) that is 10% more sensitive than H1. We use the null stream to form a list of veto times. We first whiten the null stream,

$$\tilde{s}_{\text{null,white}}(f) = \frac{\tilde{s}_{\text{null}}(f)}{\sqrt{S_{\text{null}}(f)}} . \quad (3.3.4)$$

Whitening is the process of removing any frequency dependence from the PSD. In reality, $S_{\text{null}}(f)$ is an average PSD of the null combination over a given time interval. Bursts of

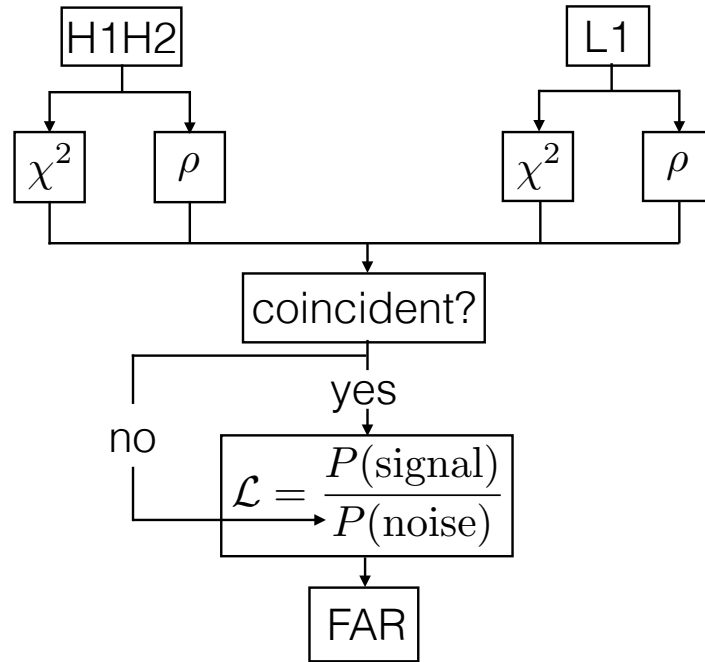


Figure 24 : A flow chart of the `gstlal_inspiral` pipeline.

power that appear over short time intervals compared to the average time for the PSD will not be eliminated through the whitening process. Since this is the null combination, any bursts of power must be associated with glitches, not gravitational-wave events. We set a threshold on the whitened null stream and mark any time periods that cross above the threshold as veto times. This means that any gravitational-wave event candidates that we identify in these veto times will be discarded after-the-fact.

3.4 Search software algorithm

The software that we use for the SSM binary search is `gstlal_inspiral` from the `gstlal` software package (Cannon et al. 2014, 2012), which is poised as the leading low-latency CBC search pipeline for aLIGO. As described in Sec. 3.1, `gstlal_inspiral` computes the SNR statistics for a template bank for all interferometers involved in the search. The pipeline employs several methods to improve the computational speed of this calculation. These methods are briefly described in Sec. 3.4.1. After triggers are generated by passing a pre-determined SNR threshold, the pipeline computes the autocorrelation χ^2 statistic for each trigger and checks for coincidence in triggers across detectors. As discussed

in Sec. 3.1.3, we look for coincidence in time and template. All triggers that pass the coincidence tests are considered gravitational-wave event candidates. We know that we do not have stationary, Gaussian noise, so the maximized SNR is not the maximum likelihood statistic. Instead, a different likelihood statistic, described in Sec. 3.4.2, is computed using both the SNR and the autocorrelation χ^2 statistic for each event candidate. Any triggers that pass the SNR threshold but are not found in coincidence are known to be produced by noise. These triggers are actually used to help determine the denominator of the likelihood statistic. The value of the likelihood for all event candidates is translated into a false alarm rate (FAR). We place a threshold on the FAR, and all event candidates that pass the FAR threshold are considered gravitational-wave events. Sec. 3.4.3 discusses the transformation from likelihood into FAR. Fig. 24 is a flow chart that demonstrates the procedure `gstlal_inspiral` uses to identify gravitational-wave events.

3.4.1 Low-latency SNR calculation

The first search statistic that is computed is the SNR time series. This is derived from the matched filter statistic (see Eq. (3.1.9)), as $\rho(t) = |z(t)|/\sigma$. In reality, we absorb the normalization σ into the templates. We also whiten both the templates and the data such that,

$$\begin{aligned}\tilde{s}_w(f) &= \frac{\tilde{s}(f)}{\sqrt{S_n(f)}} \\ \tilde{m}_{w,n}(f) &= \frac{\tilde{m}(f)}{\sigma\sqrt{S_n(f)}}\end{aligned}$$

where $\tilde{s}_w(f)$ is the whitened data, $\tilde{m}_{w,n}(f)$ is the whitened, normalized template, and $S_n(f)$ is the power spectral density of the noise. In this formalism, the SNR time series is calculated through,

$$\rho(t) = \left| 4 \int_0^\infty \tilde{s}_w(f) \tilde{m}_{w,n}^*(f) e^{2\pi i f t} df \right|. \quad (3.4.1)$$

The external strain on the LIGO detectors is a time series, but the SNR is traditionally calculated in the frequency domain due to the computational efficiency of the calculation in the frequency domain. Typically, the data is chunked up in time, each time chunk is Fourier transformed, and then the SNR is calculated on that chunk.

There is inherent latency involved in the frequency domain calculation of SNR since enough data must accumulate for a time chunk before the SNR can be computed. The `gstlal_inspiral` pipeline is designed as a low-latency search pipeline and therefore seeks to avoid the inherent latency of the frequency domain calculation. Eq. (3.4.1) can also be expressed in the time domain,

$$\rho(t) = \left| 2 \int_{-\infty}^{\infty} s_w(\tau) m'_{w,n}(\tau - t) d\tau \right|, \quad (3.4.2)$$

where $m'_{w,n}(t) = m_{w,n}(t, \phi_0 = 0) + im_{w,n}(t, \phi_0 = \pi/2)$, which is used in order to maximize over termination phase, and the template $m_{w,n}(t)$ is a windowed kernel. For a signal model that would be in the LIGO sensitive frequency band for a duration T ,

$$m_{w,n}(t) = \begin{cases} 0 & : t < 0 \\ m_T & : 0 < t < T \\ 0 & : t > T \end{cases}$$

where m_T is the whitened, normalized signal model as it would appear in the LIGO sensitive frequency band.

The SNR computation in the time domain is capable of producing real-time output, once a time T has passed from the start of the analysis, where T is the template duration. However, the time domain computation is computationally expensive. Actually producing low-latency output would require a very large amount of computing power. The `gstlal_inspiral` pipeline combats this issue by using several tricks for reducing the SNR calculation's computational requirements.

The LIGO data is not a continuous time series but is discretely sampled at a sample rate of 16384 Hz. The discretized version of Eq. (3.4.2) is

$$\rho[i] = \left| 2 \sum_{j=0}^{N-1} s_w[j] m'_{w,n}[j - i] \Delta t \right|, \quad (3.4.3)$$

where $N = T/\Delta t$ is the length of template. However, the signal model does not need to be sampled at 16384 Hz across its full duration. Fig. 4 shows an example CBC waveform. At early times, this template can be effectively sampled at lower frequencies than at later times. It saves computational cost to slice the template up in time and resample each

time slice to only the necessary sampling rate. The s^{th} time sliced template sampled at a rate of f_s would be,

$$m_{w,n}^s[j] \equiv \begin{cases} m_{w,n} \left[j \frac{f}{f_s} \right], & \text{if } t_s \leq j/f_s < t_{s+1} \\ 0, & \text{otherwise,} \end{cases} \quad (3.4.4)$$

where f is the original sample rate of the template and $[t_s, t_{s+1})$ is the time interval for the s^{th} time slice. The SNR calculation is then performed on each time slice separately, with the data being resampled to the appropriate sample rate,

$$\rho_s[i] = \left| 2 \sum_{j=0}^{N_s-1} s_w \left[j \frac{f}{f_s} \right] m_{w,n}^{s'} \left[(j-i) \frac{f}{f_s} \right] \Delta t_s \right|, \quad (3.4.5)$$

where N_s is the number of samples in the s^{th} time slice and $f_s = 1/\Delta t_s$. Details on the exact computational cost savings for this method can be found in Cannon et al. (2012).

In addition to slicing the templates in time and resampling to a lower sampling rate, the `gstlal_inspiral` pipeline also reduces the computational cost of the time-domain SNR calculation by taking advantage of the redundancy of the templates in a template bank. The templates in the template bank form a matrix where the rows are the whitened, normalized time-domain template samples and columns are template index. In this formalism, the SNR for all templates in the bank can be reduced to a matrix operation,

$$\rho_s = 2 M_s s_w, \quad (3.4.6)$$

where M_s is the matrix of templates and the subscript s refers to a specific time slice. In fact, the matrix M_s contains $2N$ templates where N is the number of templates in the template bank, one template with phase $\phi_0 = 0$ and one template with phase $\phi_0 = \pi/2$ for each template in the bank. The SNR maximized over termination phase is the quadrature sum of the two orthogonal phase templates. Many of the templates in the template bank are redundant, since this is necessary to fill the bank with the appropriate minimal match. However, this leads to redundant computations for SNR. The effective dimension of the matrix M_s is reduced in `gstlal_inspiral` by performing a singular value decomposition (SVD) on the matrix M_s and computing the SNR using the decomposed matrix. The singular vectors of the SVDed M_s are ranked by singular value, and the least important

singular vectors (lowest corresponding singular value) are discarded. This effectively reduces the dimensions of M_s , which in turn reduces the computational cost of the SNR calculation. The truncation of the matrix M_s is done in a manner such that the fractional loss in SNR is

$$\left\langle \frac{\delta\rho}{\rho} \right\rangle = \frac{1}{2n} \sum_{s=0}^{S-1} \sum_{\mu=n's+1}^n (\sigma_\mu^s)^2, \quad (3.4.7)$$

where n is the number of rows in M_s , n' is the number of rows in the truncated M_s , S is the total number of time slices, and σ_ν^s is the ν^{th} singular value in time slice s (Wade 2012). The details of how the full SVD decomposition and truncation method is employed can be found in Cannon et al. (2010) and Cannon et al. (2012).

The combination of time slicing the templates and truncating a singular value decomposition of the matrix of templates in the template bank allows the low-latency, time-domain computation of SNR to become computationally feasible given reasonable computing resources. The `gstlal_inspiral` pipeline uses the autocorrelation χ^2 statistic, discussed in Sec. 3.1.3, as the second detection statistic. This statistic is already computationally efficient and does not require further improvement for use in low-latency. Once SNR and autocorrelation χ^2 are computed, the next step in the algorithm is to compute a likelihood based on these two statistics.

3.4.2 Likelihood statistic in `gstlal_inspiral`

As was shown in Eq. (3.1.1), the likelihood ratio determines the probability that there is a signal in the data given the data; it is given by the probability of the data given a signal is present divided by the probability of the data given only noise. The `gstlal_inspiral` pipeline computes a likelihood ratio statistic to rank gravitational-wave candidates from the two detection statistics, SNR and χ^2 , and from probabilities of these statistics manifesting in the detected combination of interferometers at detected interferometer sensitivities. In fact, there are N combinations of SNR and χ^2 where N is the number of interferometers involved in the search. For this search, there is ρ_{H1H2} , χ_{H1H2}^2 , ρ_{L1} , and χ_{L1}^2 , where H1H2 is the effective coherent detector of H1 and H2. The likelihood ratio used by `gstlal_inspiral` is discussed in detail in Cannon et al. (2015) and Cannon et al. (2013). This section gives a brief overview of the likelihood calculation. The likelihood

ratio statistic that is used is

$$\Lambda(\text{signal}|\{D_{\text{HIFO1}}, D_{\text{HIFO2}}, \dots\}, \{\text{IFO1}, \text{IFO2}, \dots\}, \rho_{\text{IFO1}}, \chi_{\text{IFO1}}^2, \rho_{\text{IFO2}}, \chi_{\text{IFO2}}^2, \dots, \bar{\theta}) \quad (3.4.8)$$

$$= \Lambda(\dots|\bar{\theta})\Lambda(\bar{\theta}) \quad (3.4.9)$$

$$= \frac{P(\{D_{\text{HIFO1}}, D_{\text{HIFO2}}, \dots\}, \{\text{IFO1}, \text{IFO2}, \dots\}, \rho_{\text{IFO1}}, \chi_{\text{IFO1}}^2, \rho_{\text{IFO2}}, \chi_{\text{IFO2}}^2, \dots | \bar{\theta}, \text{signal})}{P(\{D_{\text{HIFO1}}, D_{\text{HIFO2}}, \dots\}, \{\text{IFO1}, \text{IFO2}, \dots\}, \rho_{\text{IFO1}}, \chi_{\text{IFO1}}^2, \rho_{\text{IFO2}}, \chi_{\text{IFO2}}^2, \dots | \bar{\theta}, \text{noise})} \Lambda(\bar{\theta}), \quad (3.4.10)$$

where $\{D_{\text{HIFO1}}, D_{\text{HIFO2}}, \dots\}$ is the horizon distance for the set of interferometers (IFOs) that observed an event, $\{\text{IFO1}, \text{IFO2}, \dots\}$ is the set if IFOs that observed the event, and $\bar{\theta}$ are the template parameters for the event. This is a likelihood statistic in that it is a probability of the data given a signal in the data and template parameters $\bar{\theta}$ divided by a probability of the data given noise only and the template parameters $\bar{\theta}$. These probabilities depend on the specific set of coincident IFOs, the sensitivity of those IFOs, given by the horizon distance, and computed values for the detection statistics SNR and χ^2 .

The factor $\Lambda(\bar{\theta})$ is the probability of finding parameters $\bar{\theta}$ given a signal in the data divided by the probability of finding parameters $\bar{\theta}$ given only noise in the data. The probability of finding parameters $\bar{\theta}$ given a signal in the data is chosen to be uniform, and the probability of finding $\bar{\theta}$ given only noise in the data is computed by dividing the total number of noise events found for a template with parameters $\bar{\theta}$ by the total number of noise events found by all templates.

The numerator of the Eq. (3.4.10) can be factored to

$$\begin{aligned} & P(\{D_{\text{HIFO1}}, D_{\text{HIFO2}}, \dots\})P(\{\text{IFO1}, \text{IFO2}, \dots\}|\{D_{\text{HIFO1}}, D_{\text{HIFO2}}, \dots\}, \text{signal}) \\ & \times P(\rho_{\text{IFO1}}, \rho_{\text{IFO2}}, \dots|\{D_{\text{HIFO1}}, D_{\text{HIFO2}}, \dots\}, \{\text{IFO1}, \text{IFO2}, \dots\}, \text{signal}) \\ & \times \prod_{\text{inst} \in \{\text{IFO1}, \text{IFO2}, \dots\}} P(\chi_{\text{inst}}^2 | \rho_{\text{inst}}, \text{signal}), \end{aligned} \quad (3.4.11)$$

since the χ^2 values for each of the IFOs are independent, and the denominator can be factored to

$$\begin{aligned} & P(\{D_{\text{HIFO1}}, D_{\text{HIFO2}}, \dots\})P(\{\text{IFO1}, \text{IFO2}, \dots\}|\text{noise}) \\ & \times \prod_{\text{inst} \in \{\text{IFO1}, \text{IFO2}, \dots\}} P(\rho_{\text{inst}}, \chi_{\text{inst}}^2 | \text{noise}) \end{aligned} \quad (3.4.12)$$

since the noise in each IFO is independent.

The first factor in Eq. (3.4.11) and Eq. (3.4.12) are common to the numerator and the denominator and therefore cancel out of the likelihood calculation. The remaining factors in the numerator of the likelihood are computed in the following manner:

- The second factor in Eq. (3.4.11), $P(\{\text{IFO1}, \text{IFO2}, \dots\} | \{D_{\text{HIFO1}}, D_{\text{HIFO2}}, \dots\}, \text{signal})$, is the probability that the specific set of IFOs finds the signal in coincidence given the signal and the IFO sensitivities. This term is computed by performing a Monte Carlo integration over the full sky that gives the number of sources visible above an SNR threshold in a certain set of IFOs.
- The third factor in Eq. (3.4.11), $P(\rho_{\text{IFO1}}, \rho_{\text{IFO2}}, \dots | \{D_{\text{HIFO1}}, D_{\text{HIFO2}}, \dots\}, \{\text{IFO1}, \text{IFO2}, \dots\}, \text{signal})$, is the joint probability of finding the signal with specific values of SNR given the set of coincident detectors and their sensitivities. This term is also computed with a Monte Carlo integration that maps out the correlations between SNRs for each set of IFOs.
- The fourth factor in Eq. (3.4.11), $P(\chi_{\text{inst}}^2 | \rho_{\text{inst}}, \text{signal})$, is the probability of obtaining the specific value of χ^2 for the signal given an SNR. This is computed by first computing $P(\rho, \chi^2/\rho^2 | \text{signal})$, given by an analytic expression assuming Gaussian noise, and then marginalizing over ρ .

The remaining terms in the denominator of the likelihood are calculated in the following manner:

- The second factor in Eq. (3.4.12), $P(\{\text{IFO1}, \text{IFO2}, \dots\} | \text{noise})$, is the probability that a specific set of IFOs will find a trigger in coincidence given only noise. This is computed by measuring the rate of noise triggers in each separate IFO and using the coincidence time window, which is the time window in which the trigger must appear in another IFO in order to be considered coincident, to find the rate of noise coincidences in a set of IFOs.
- The third factor in Eq. (3.4.12), $P(\rho_{\text{inst}}, \chi_{\text{inst}}^2 | \text{noise})$, is the probability that specific values for SNR and χ^2 will be found given only noise. Triggers that pass the SNR threshold but are not found in coincidence are called “non-coincident triggers.” The

non-coincident triggers are binned up in SNR and χ^2 space to form the probability of obtaining a certain SNR and χ^2 from noise alone. This is shown as part of the `gstlal_inspiral` flow chart in Fig. 24.

After all of the components are calculated, an interpolated likelihood function is computed and used to assign likelihood values to all gravitational-wave candidates.

3.4.3 False alarm probability (FAP) and false alarm rate (FAR)

The final step in determining if there are any gravitational-wave events in the data is to assign a false alarm probability and, for historical reasons, a false alarm rate to each gravitational-wave candidate. The full details of this calculation can be found in Cannon et al. (2015) and Cannon et al. (2013). The false alarm probability (FAP) is the probability that a noise event would be assigned likelihood Λ . To find FAP, first compute

$$P(\Lambda|\bar{\theta}, \text{noise}) = \int_{\Sigma(\Lambda)} P(\dots|\bar{\theta}, \text{noise}) d^{n-1}\Sigma, \quad (3.4.13)$$

where (...) are all n parameters that the likelihood depends on, as given in Eq. (3.4.10), and $\Sigma(\Lambda)$ are surfaces of constant likelihood Λ . This integral is computed by sampling the (...) parameter space using importance-weighted sampling and determining Λ and $P(\dots|\bar{\theta}, \text{noise})$ at each sample point. Once the space is adequately sampled, the integral can be computed along a surface of constant Λ . Eq. (3.4.13) is then marginalized over all of the templates to give $P(\Lambda|\text{noise})$. The probability of finding a noise event with $\Lambda \geq \Lambda^*$ is

$$P(\Lambda \geq \Lambda^*|\text{noise}) = \int_{\Lambda^*}^{\infty} P(\Lambda|\text{noise}) d\Lambda. \quad (3.4.14)$$

Accounting for the trials factor, the probability of finding at least one event with $\Lambda \geq \Lambda^*$ from m independent coincidences is

$$P(\Lambda \geq \Lambda^*|m \text{ ind. coins.}) = 1 - (1 - P(\Lambda \geq \Lambda^*|\text{noise}))^m, \quad (3.4.15)$$

which is the false alarm probability.

For historical reasons and in order to compare to other CBC searches, the FAP is turned into a false alarm rate (FAR). Assuming Poisson statistics, the probability of

observing n events when the mean of the Poisson process is λ is

$$P(n|\lambda) = \frac{\lambda^n}{n!} e^{-\lambda}, \quad (3.4.16)$$

and the probability of observing n or more events is

$$P(\geq n|\lambda) = 1 - e^{-\lambda} \sum_{j=0}^{n-1} \frac{\lambda^j}{j!}. \quad (3.4.17)$$

The FAP is the probability of observing one or more events with $\Lambda \geq \Lambda^*$. Setting $n = 1$ in Eq. (3.4.17) gives

$$P(\geq 1|\lambda) = P(\Lambda \geq \Lambda^* | m \text{ ind. coins.}) = 1 - e^{-\lambda}. \quad (3.4.18)$$

Solving Eq. (3.4.18) for λ , which is a function of Λ^* , gives

$$\lambda(\Lambda^*) = -\ln[1 - P(\Lambda \geq \Lambda^* | m \text{ ind. coins.})] \quad (3.4.19)$$

or, equivalently,

$$\lambda(\Lambda^*) = -m \ln \left[\int_0^{\Lambda^*} P(\Lambda | \text{noise}) d\Lambda \right]. \quad (3.4.20)$$

The false alarm rate is the average number of events with $\Lambda \geq \Lambda^*$, which is $\lambda(\Lambda^*)$ divided by the observation time T ,

$$\text{FAR}(\Lambda^*) = \frac{\lambda(\Lambda^*)}{T}. \quad (3.4.21)$$

The final step in determining whether a gravitational-wave candidate is an event is to place a threshold on the FAR. Any gravitational-wave candidates above the threshold are considered events. For the SSM binary search which took place on one month of data, a 5σ detection would require $\text{FAR} \approx \text{FAP}/(\text{one month}) = (1/1744278)/(2629740 \text{ s}) = 2.18 \times 10^{-13}$.

3.5 Results

We analyze one week of data from iLIGO's fifth science run using the template bank described in Sec. 3.2 and the `gstlal_inspiral` search pipeline described in Sec. 3.4. The template bank is composed using the frequency domain post-Newtonian CBC waveform with phase corrections kept out to the 3.5 post-Newtonian order. The time period we

chose to analyze was from GPS times 871156422 - 873786162. GPS time is the number of seconds since 00:00:00 UTC, January 6, 1980. These times correspond to 19:53:28, August 14, 2007 - 06:22:28, September 14, 2007. We use the null vetoes described in Sec. 3.3 and the following three categories of data quality vetoes:

- Category 1: Indicates a severe problem with the data to the point where any PSD estimates are unusable.
- Category 2: Indicates a major problem with the data, such as instrumental problems in sub-systems that are known to couple to the DARM feedback loop.
- Category 3: Indicates a moderate concern with the data, such as an elevated glitch level.

In order to test the efficiency and sensitivity of the search pipeline on the SSM binary region of parameter space, we insert a large number of simulated CBC signals (“injections”) into the data. We analyze the signals the same way any real triggers would be analyzed by the pipeline. We then draw conclusions on the sensitivity and efficiency of the search pipeline based on how many injections were found in the data and how many injections were missed in the data. In addition, we record the computational resources required to perform the search and conclude on the `gstlal_inspiral` pipeline’s ability to perform a similar type of search, such as an aLIGO BNS search, in low latency. Finally, we determine if any gravitational-wave events were present in the analyzed data.

3.5.1 Search sensitivity

We chose to distribute the injection set uniformly in component masses between $0.11 M_{\odot}$ and $1.4 M_{\odot}$ with the mass ratio restricted to $[1 : 1, 3 : 1]$, uniformly in the logarithm of distance, and uniformly in sky position, cosine of inclination angle, and polarization. The waveform used for injections is the post-Newtonian CBC waveform with phase corrections kept out to 3.5 post-Newtonian order. The injections were performed uniformly in time throughout the entire search period.

One measure of the sensitivity and efficiency of the search is to analyze how many of the injections were found and how many were missed. Fig. 25 shows how many injections

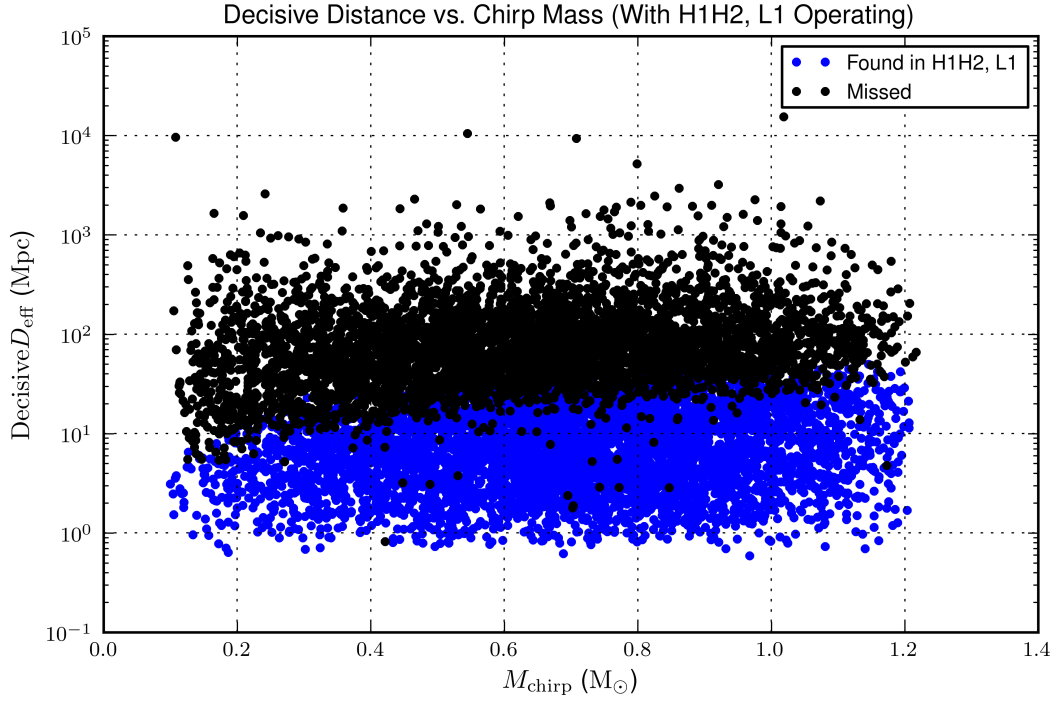


Figure 25 : Distribution of injections that were found (blue dots) above the FAR threshold and injections that were missed (black dots) in Chirp Mass–Decisive $D_{\text{effective}}$ space.

were found (blue dots) and how many injections were missed (red dots) in Chirp Mass – Decisive $D_{\text{effective}}$ space. Decisive $D_{\text{effective}}$ is the second highest $D_{\text{effective}}$ out of the operating instruments for each set of injection parameters, and $D_{\text{effective}}$ and chirp mass are defined in Eqs. (1.2.14) and (1.2.11), respectively. Out of the 10,177 injections, a total of 5,326 were found and 4,851 were missed.

We compute the efficiency of the search over a range of distances by first creating M distance bins. We determine the total number of found injections in the j^{th} bin $N_{\text{found},j}$ and divide that by the total number of injections N_j in the bin to give the efficiency of the j^{th} distance bin,

$$\epsilon_j = \frac{N_{\text{found},j}}{N_j} . \quad (3.5.1)$$

The efficiency in each distance bin can then be used to compute the volume to which the search was sensitive,

$$V = \sum_{j=1}^M 4\pi\epsilon_j d_j^2 \Delta d_j , \quad (3.5.2)$$

where d_j is a representative distance in the j^{th} distance bin, such as the midpoint of the

bin, and Δd_j is the width of the bin. The distance to which the search is sensitive R is then just derived from the sensitive volume,

$$R = \left(\frac{3V}{4\pi} \right)^{1/3}. \quad (3.5.3)$$

The sensitive distance is a measure how far the search is actually sensitive out to (in an average sense), taking into account the combined instrument noise and the search procedure.

There is error in the calculation for efficiency associated with the fact that we perform only a finite number of injections. This error is modeled approximately by a binomial distribution,

$$\Delta\epsilon_j = \sqrt{\frac{\epsilon_j(1-\epsilon_j)}{N_j}}. \quad (3.5.4)$$

The errors on efficiency are propagated into errors on sensitive volume, and the error on sensitive distance is derived from the relationship between sensitive distance and sensitive volume (Eq. (3.5.3)),

$$\begin{aligned} \Delta V &= \sqrt{\sum_{j=1}^M (4\pi\Delta\epsilon_j d_j^2 \Delta d_j)^2} \\ \Delta R &= \frac{R}{3} \frac{\Delta V}{V}, \end{aligned}$$

where Δd_j still refers to the width of the j^{th} distance bin.

Fig. 26 shows the sensitive distance of the SSM binary search in four total mass bins as a function of FAR. The sensitive distance is a function of FAR through the FAR threshold that determines found injections in the efficiency calculation (Eq. (3.5.1)). For the smallest total mass values, ranging from $0.00 M_\odot - 0.75 M_\odot$, we are sensitive to systems out to ~ 4 Mpc. This includes the Local Group and therefore provides a significant expansion to previous searches for MACHOs.

3.5.2 Required computing resources

The SSM binary search was conducted on a large LSC computing cluster. Condor was used to distribute the analysis across computing nodes (HTCondor 2015). We track the total number of CPU hours used for the analysis through condor and determine the

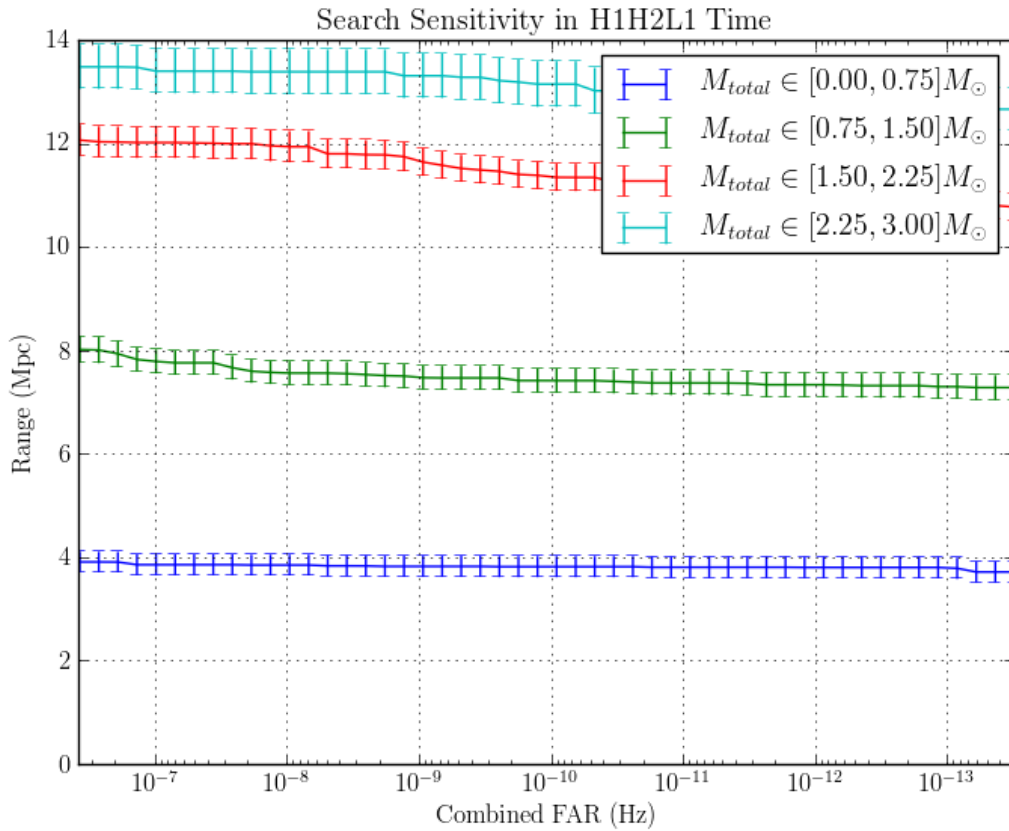


Figure 26 : The sensitive distance of the SSM binary search across a range of FAR values. The sensitive distance is provided for four chirp mass bins.

number of CPUs required in order for the analysis to be able to produce real-time results. This is how many CPUs are required in order for the analysis to complete in N days when analyzing N days of data. The number of CPUs required in order to produce real-time results is

$$\#\text{CPUs} = \frac{\text{CPU hours}}{\text{analysis time}}. \quad (3.5.5)$$

Certain properties of the `gstlal_inspirals` pipeline were tuned to maximize efficiency and minimize computational cost. For example, the level of truncation of the SVDed matrix of templates was tuned and how often the full SNR time series was reconstructed from the SVDed result was tuned. These tunings were done by hand and could be optimized more efficiently in the future.

After tuning the pipeline, we found that for our one month analysis of S5 data, we would require ~ 200 CPUs in order to produce real-time results. We conclude that a

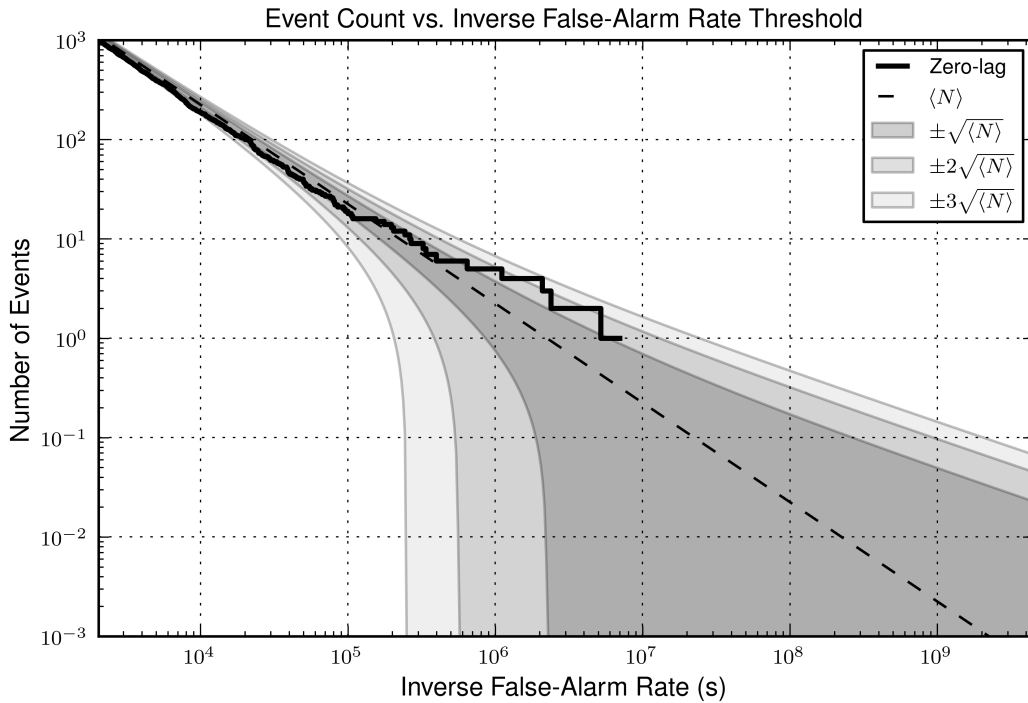


Figure 27 : The number of events detected vs. inverse FAR (solid line). The dotted line indicates the expectation from a Poisson process. The shaded regions indicate 1σ , 2σ , and 3σ contours.

comparable aLIGO BNS search would require ~ 200 CPUs in order to produce low-latency gravitational-wave events. This is a very reasonable computing request and shows the low-latency `gstlal_inspiral` pipeline is ready for a high performing, low-latency search in the advanced detector era.

3.5.3 Gravitational-wave detection results

Fig. 27 shows the number of events detected vs. inverse FAR and compares this to the expectation from a Poisson process. The number of detected events for a given inverse FAR is consistent with a Poisson process to within 3σ , which means all detected events fall within the expectation of a noise event to 3σ . None of the detected events stand out above the noise as true gravitational-wave events.

The loudest gravitational-wave candidate had a FAR of 1.43×10^{-7} and a FAP of 0.295. This event was found as a $1.37 M_{\odot} - 0.47 M_{\odot}$ system with a combined SNR of 9.36. This loudest gravitational-wave candidate was within 2σ of the expected background and therefore is not significant enough to be considered a gravitational-wave event. There

were multiple events found with a FAR $\sim 10^{-7}$. However, the combination of these events still falls within 3σ of the expectation from a Poisson process.

3.6 Conclusions

While no gravitational-wave events were found in this search, it did yield positive results. We find the `gstlal_inspiral` search pipeline is sensitive to SSM binary systems out to the edge of our Local Group for the least massive systems (and farther for more massive systems). Previously, MACHOs, such as SSM binary systems, have only been searched for within our own Milky Way halo. The SSM binary search is able to significantly expand the search volume to other galaxy halos within our Local Group. In addition, we find that the `gstlal_inspiral` search pipeline is already at a very reasonable computational efficiency for long-duration, large-template-bank searches, such as a search for BNS systems in aLIGO data at design sensitivity.

We plan to expand this work in the future and run the SSM binary search on all of LIGO's fifth (S5) and sixth (S6) science run data. LIGO's sixth science run yielded improved instrument sensitivity over S5. However, a search on S6 data would not employ the coherent and null data streams for the co-located Hanford detectors, since the smaller Hanford detector (H2) was decommissioned in S6. Future work also involves including the Virgo interferometer in each analysis. A search involving a three detector network is more computationally burdensome and further study is required to determine the computational readiness of `gstlal_inspiral` for a three detector network BNS search in the advanced detector era.

While we hope to discover gravitational-wave events in a search on all of S5 and/or S6 data, we can also produce interesting results in the absence of a detection. If no gravitational-wave events are found, we will set an upper limit on the rate of SSM binary coalescences that includes information beyond our own galaxy halo. Such a result can contribute useful information to the mystery of the nature of dark matter.

After a gravitational-wave detection is made, there is a good deal of astrophysics that can be extracted from the detection. Ch. 4 discusses one route for post-detection science through a test of conjectures believed to be true in general relativity.

Chapter 4

Tests of cosmic censorship and the no-hair theorem with aLIGO

“The greatest secrets are always hidden in the most unlikely places.”

— Roald Dahl, *Charlie and the Chocolate Factory*

4.1 Introduction

This chapter follows closely Wade et al. (2013) and involves work done in collaboration with Jolien Creighton, Evan Ochsner, and Alex Nielsen. As was discussed in Sec. 1.2, the inspiral portion of compact binary coalescence (CBC) events are the most promising sources for gravitational-wave detections in ground-based interferometers, such as aLIGO. Expected detection rates for binary black hole (BBH) mergers range from 0.4 to 1000 per year with a realistic rate of 20 per year, and expected detection rates for neutron-star–black-hole (NS-BH) mergers range from 0.2 to 300 per year with a realistic rate of 10 per year (Abadie et al. 2010). The form of the gravitational-wave strain, as it was introduced in Sec. 1.1, depends on the chosen metric theory of gravity. The most accepted theory of gravity is Einstein’s theory of general relativity. An important use of gravitational-wave detectors will be to test the theory of general relativity and cosmological conjectures associated with general relativity.

Even within the confines of general relativity, there are conjectures that, while widely

believed, have not been absolutely established, and violations could be uncovered by gravitational-wave observations. One such conjecture that is believed to be true in general relativity is the cosmic censorship conjecture, which states roughly that all singularities in spacetime must have an event horizon that conceals the singularity from a distant observer (Penrose 1969). In the Kerr geometry of a spinning black hole, the event horizon can only exist for mass and spin ratios that satisfy the Kerr bound, $j \leq m^2$ in geometric units (adopted throughout this chapter), where j is the spin of the black hole and m is the mass of the black hole. If the spin of a compact object exceeds the value of its mass squared, then the compact object violates the cosmic censorship conjecture within the context of the Kerr geometry (Kerr 1963; Misner et al. 1973; Hartle 2003). This limit is often expressed in terms of the Kerr parameter $\chi \equiv j/m^2 \leq 1$.

The no-hair theorem is a consequence of the theory of general relativity. The no-hair theorem states that a regular black hole that has settled down to its final stationary vacuum state is determined only by its mass, spin and electric charge (Hawking 1971, 1972; Israel 1967, 1968; Carter 1970; Ruffini & Wheeler 1971; Misner et al. 1973; Chrusciel et al. 2012). Astrophysical black holes are thought to be electrically neutral, and therefore would be categorized just by their mass and spin. It is widely expected that black holes in binary systems will be closely described by such simple states for most of the inspiral phase. Although the black hole will be slightly tidally distorted by its binary partner, it has been shown that the relativistic tidal Love number of a nonrotating black hole will still be zero (Binnington & Poisson 2009). The literature shows that the tidal Love number should be zero for slowly rotating black holes (Landry & Poisson 2015), and we suspect it should still be small for rapidly rotating black holes. Thus if the post-Newtonian tidal Love number is found to deviate from zero for a nonrotating object, it can be seen as evidence that the requirements of the no-hair theorem are not fulfilled, since the black hole is no longer uniquely defined by its mass, spin and electric charge. If the object is too massive to be a neutron star (i.e. $m_i > 3 M_\odot$)¹, then it is likely to be some exotic

¹Reasonably general arguments show that compact objects having $m > 3 M_\odot$ should be fully-collapsed black holes (Hannam et al. 2013), though it is possible that exotic objects may have masses with $m > 3 M_\odot$.

object far from the Schwarzschild solution. A more detailed discussion of the implications of the no-hair theorem can be found in Sec. 4.4.2.

The gravitational-wave strain produced by the inspiral portion of a CBC event depends on the system's parameters, such as component masses, component spins, and component tidal Love numbers. Once a gravitational-wave detection is made by aLIGO, parameter estimation techniques will be used to extract the system's most likely parameters from the raw data. This will be done using full Bayesian analyses that involve techniques such as Markov-chain Monte Carlo and nested sampling. An in-depth discussion of LIGO parameter estimation can be found in the LIGO Scientific Collaboration et al. (2013). Based on the results of parameter estimation, if at least one of the system's measured component masses indicates that a body should nominally be a black hole, then the system can be used to test for apparent violations of the cosmic censorship conjecture and the no-hair theorem.

Many other authors have investigated the possibility of using gravitational-wave observations to test aspects of general relativity. These include measuring the deviation of post-Newtonian coefficients from their predicted values in general relativity (Arun et al. 2006; Yunes & Pretorius 2009; Li et al. 2012), looking for alternative wave-polarization states that do not occur in general relativity (Chatziioannou et al. 2012; Hayama & Nishizawa 2013), testing for a nonzero graviton mass (Arun & Will 2009; Mirshekari et al. 2012; Keppel & Ajith 2010), and exploring whether the ringdown signal is consistent with the quasinormal modes of a Kerr black hole (Gossan et al. 2012; Dreyer et al. 2004; Kamaretsos et al. 2012). For recent reviews of these techniques, see Van Den Broeck (2013); Arun & Pai (2013); Yunes & Siemens (2013). Rodriguez et al. (2012) look at aLIGO's ability to verify the no-hair theorem for intermediate-mass black hole systems. Tests of the no-hair theorem and cosmic censorship can also be conducted in the electromagnetic sector using a variety of techniques, including accretion disk modeling (Johannsen & Psaltis 2013), observations of orbiting stars and gas (Sadeghian & Will 2011), and pulsar orbit timing (Stairs 2003).

The inspiral portion of the CBC gravitational waveform is well-modeled by post-Newtonian (pN) expansions to the phase and amplitude of the waveform (Einstein et al.

1938; Epstein & Wagoner 1975; Misner et al. 1973; Weinberg 1972; Blanchet 2002; Creighton & Anderson 2011; Buonanno et al. 2009). However, systematic biases due to the deviation of a post-Newtonian waveform from the true waveform can significantly affect parameter estimation. Therefore, when using post-Newtonian waveforms, it is important to employ the most up-to-date and accurate calculations. We use the waveforms provided in Arun et al. (2009) that include post-Newtonian expansions of the phase to 3.5 pN order and of the amplitude to 2.5 pN order. Spin corrections are calculated for both the post-Newtonian phase to 2.5 pN order and amplitude to 2.0 pN order in Arun et al. (2009). We briefly investigate how the 3.0 pN- and 3.5 pN order spin-orbit phase corrections calculated by Marsat et al. (2013) affect our results. For nonspinning, tidal waveforms, we use the lowest-order tidal correction to the phase of the waveform given in Hinderer et al. (2010).

To estimate the measurability of parameters appearing in the inspiral CBC gravitational waveform, we use the Fisher matrix formalism for a single detector, described in Sec. 4.3. The accuracy of measurement errors produced by the Fisher matrix formalism is a function of the signal-to-noise ratio (SNR). At low SNR, parameter error estimates obtained with the Fisher matrix formalism will be biased (Vallisneri 2008). However, a more accurate Bayesian approach to parameter estimation using techniques such as Markov-chain Monte Carlo (MCMC) can be computationally expensive. For the purpose of this preliminary investigation, the Fisher matrix formalism does well to indicate the effects that should be studied more closely with a full Bayesian analysis.

Much work has been done on parameter measurability for CBC systems using the Fisher matrix formalism and post-Newtonian CBC inspiral waveforms. Cutler & Flanagan (1994) studied the measurability of spin parameters, along with other parameters, for the gravitational waveform with a Newtonian-amplitude (0.0 pN order correction to the amplitude) and 1.5 pN order corrections to the phase. Poisson & Will (1995) and Królak et al. (1995) expanded the study for Newtonian-amplitude waveforms with 2.0 pN order phase corrections. Arun et al. (2005) studied parameter estimation for nonspinning waveforms with a Newtonian-amplitude and phase corrections to 3.5 pN order. Van Den Broeck & Sengupta (2007) included post-Newtonian corrections to the amplitude of the

waveform and kept corrections to 3.5 pN order in the phase of the waveform, including spin effects in the phase. Nielsen (2013) studied a Newtonian-amplitude waveform with additional spin-spin and spin-orbit corrections appearing in the phase of the waveform as derived in Arun et al. (2009).

We investigate aLIGO’s ability to detect apparent violations of the cosmic censorship conjecture and the no-hair theorem. We study how different post-Newtonian approximations to the amplitude of the gravitational waveform affect parameter measurability. We include the post-Newtonian phase corrections to 3.5 pN order with spin-orbit and spin-spin² phasing corrections to 2.5 pN and 2.0 pN order respectively, and we vary the post-Newtonian-amplitude corrections from 0.0 pN to 2.5 pN order. We also study the effect of spin corrections in the amplitude of the waveform (Arun et al. 2009) and of spin-orbit corrections to the phase of the waveform at 3.0 pN and 3.5 pN order (Marsat et al. 2013).

We investigate how prior knowledge about unphysical areas of parameter space can affect the measurability of spin and tidal parameters appearing in the waveform. We have not done this by incorporating a prior into the Fisher matrix calculations. It is difficult to incorporate flat priors into the Fisher matrix formalism, although this has been studied by Nielsen (2013). Instead, we restrict some of the parameter space after a full Fisher matrix calculation has been carried out.

(Units convention: $G = c = 1$.)

4.2 Compact binary coalescence (CBC) gravitational waveform with higher harmonics

Sec. 1.2 derived the CBC gravitational waveform and described the post-Newtonian expansion of the phase of the waveform while assuming a Newtonian amplitude. Recall, the gravitational-wave strain for the inspiral portion of a CBC event has the following

²The “spin-spin” corrections include not only $\vec{\chi}_1 \cdot \vec{\chi}_2$ corrections, but also quadrupole-monopole and the so-called “self-spin” terms $\propto \chi_1^2$.

general form in the frequency domain

$$\tilde{h}(f) = A(f; \vec{\theta}) e^{i\Psi(f; \vec{\theta})}, \quad (4.2.1)$$

where f is the gravitational-wave frequency and $\vec{\theta}$ are the parameters of the system producing the gravitational-wave signal (Misner et al. 1973). In general, we expand the amplitude A and the phase Ψ in a post-Newtonian (pN) approximation, and the phase is found using the stationary phase approximation (SPA). The form for the pN expanded waveform in amplitude and phase given in Arun et al. (2009) is

$$\tilde{h}(f) = \frac{M^2}{D_M} \sqrt{\frac{5\pi\eta}{48}} \sum_{n=0}^N \sum_{k=0}^K v_k^{n-\frac{7}{2}} C_k^{(n)} e^{i[k\Psi_{\text{SPA}}(v_k) - \pi/4]}, \quad (4.2.2)$$

where $M = m_1 + m_2$ is the total post-Newtonian mass of the binary system, D_M is the transverse comoving distance (see Hogg (1999), however, no cosmological redshift effects are included in this study), $\eta = m_1 m_2 / M^2$ is the symmetric mass ratio, Ψ_{SPA} is the SPA for the phase of the waveform to some chosen pN order (see below), the index n indicates twice the pN expansion order of the amplitude, N is twice the highest included pN expansion order of the amplitude, the index k indicates the k^{th} harmonic, K is the highest included harmonic, and the $C_k^{(n)}$ coefficients are given in Appendix D of Arun et al. (2009). The dimensionless pN expansion parameter v_k for the k^{th} harmonic is

$$v_k = \left(2\pi M \frac{f}{k} \right)^{1/3}. \quad (4.2.3)$$

The gravitational-wave frequency f is related to the orbital frequency F of the binary system through $f = kF$.

We restrict ourselves to spin-aligned (or antialigned), nonprecessing systems, where the spin is defined in the standard post-Newtonian fashion. In reality, precession should be included in the gravitational waveform model when spins are not aligned with the orbital angular momentum (Kidder 1995a; Apostolatos et al. 1994). This is especially important for unequal-mass systems, such as NS-BH binaries. The size of the precession cone scales with the mass ratio in such a way that unequal-mass systems will precess more than equal-mass systems. The effect of precession on parameter estimation has been studied in depth for space-based detectors (Lang & Hughes 2006; Vecchio 2004; Lang et al. 2011).

In these studies, it is found that precession improves parameter estimation by breaking parameter degeneracies, but astrophysical systems may not have enough precession to induce this effect. There are fewer studies of parameter estimation that include precession for ground-based detectors. The LIGO-Virgo Collaboration performed parameter estimation for a few precessing models in the LIGO Scientific Collaboration et al. (2013). The effect of precession upon detection, rather than parameter estimation, for ground-based interferometers was recently studied in Harry et al. (2013). Recent studies of precession for LIGO parameter estimation include Brown et al. (2012); Cho et al. (2013); Pekowsky et al. (2013), but there are no definitive conclusions on how precession will affect parameter estimation for ground-based detectors. Large-scale, systematic Bayesian inference analyses will likely be required to develop a better understanding of how precession will impact parameter estimation in the aLIGO era. For simplicity, we have not investigated precessing systems here.

We study waveforms with amplitude corrections up to the 2.5 pN order ($N = 5$), which include up to seven harmonics ($K = 7$) in the waveform. Post-Newtonian corrections for spinning systems have been investigated at length in, for example, Arun et al. (2009), Marsat et al. (2013), Kidder et al. (1993), Kidder (1995b), Porto (2006), Owen et al. (1998), Tagoshi et al. (2001), Faye et al. (2006), and Porto (2010). We include spin corrections to amplitude and phase as found in Arun et al. (2009). These include spin-orbit corrections calculated at 1.5 pN and 2.5 pN order in the phase, spin-spin corrections at 2.0 pN order in the phase, spin-orbit corrections appearing at 1.0 pN and 1.5 pN order in the amplitude, and spin-spin corrections appearing at 2.0 pN order in the amplitude. Separately, we also study spin-orbit corrections that appear at 3.0 pN and 3.5 pN order in the phase as recently calculated in Marsat et al. (2013). We investigate both spinning waveforms with no tidal corrections and nonspinning waveforms with the leading-order tidal correction to the phase, which appears at 5.0 pN order.

The general SPA phase Ψ_{SPA} used in Eq. (4.2.2) is

$$\begin{aligned}
\Psi_{\text{SPA}}(v_k) = & \frac{v_k^3}{M} t_c - \phi_c + \frac{3}{256} \frac{1}{v_k^5 \eta} \left\{ 1 + \left(\frac{3715}{756} + \frac{55}{9} \eta \right) v_k^2 + (4\epsilon\beta - 16\pi) v_k^3 \right. \\
& + \left(\frac{15293365}{508032} + \frac{27145}{504} \eta + \frac{3085}{72} \eta^2 - 10\epsilon\sigma \right) v_k^4 \\
& + \left(\frac{38645\pi}{756} - \frac{65\pi}{9} \eta - \epsilon\gamma \right) \left(1 + 3 \ln \left[\frac{v_k}{v_{\text{ref}}} \right] \right) v_k^5 \\
& + \left[\frac{11583231236531}{4694215680} - \frac{6848}{21} \gamma_E - \frac{640\pi^2}{3} + \left(\frac{2255\pi^2}{12} - \frac{15737765635}{3048192} \right) \eta \right. \\
& + \left. \frac{76055}{1728} \eta^2 - \frac{127825}{1296} \eta^3 - \frac{6848}{21} \ln(4v_k) + \alpha(160\pi\beta - 20\xi) \right] v_k^6 \\
& + \left[\frac{77096675\pi}{254016} + \frac{378515\pi\eta}{1512} - \frac{74045\pi\eta^2}{756} + \alpha \left(-20\zeta + \gamma \left(-\frac{2229}{112} - \frac{99\eta}{4} \right) \right. \right. \\
& \left. \left. + \beta \left(\frac{43939885}{254016} + \frac{259205\eta}{504} + \frac{10165\eta^2}{36} \right) \right) \right] v_k^7 \left. \right\}, \quad (4.2.4)
\end{aligned}$$

where ϵ and α are either 1 or 0 to turn on or off spin corrections to the phase (ϵ turns on or off the 1.5 pN- to 2.5 pN order corrections and α turns on or off the 3.0 pN- and 3.5 pN order corrections), t_c and ϕ_c are the time and phase of coalescence, $M = M\eta^{3/5}$ is the chirp mass, $\gamma_E = 0.577216\dots$ is Euler's constant, and v_{ref} is an integration constant, which we take to equal 1.

The five spin parameters appearing in Ψ_{SPA} and derived in Arun et al. (2009) and Marsat et al. (2013)— β , σ , γ , ξ , and ζ —are

$$\begin{aligned}
\beta &= \sum_{i=1}^2 \left(\frac{113}{12} \left(\frac{m_i}{M} \right)^2 + \frac{25}{4} \eta \right) \vec{\chi}_i \cdot \hat{\mathbf{L}}_N, \\
\sigma &= \eta \left[\frac{721}{48} (\vec{\chi}_1 \cdot \hat{\mathbf{L}}_N) (\vec{\chi}_2 \cdot \hat{\mathbf{L}}_N) - \frac{247}{48} (\vec{\chi}_1 \cdot \vec{\chi}_2) \right] \\
&\quad \sum_{i=1}^2 \left\{ \frac{5}{2} q_i \left(\frac{m_i}{M} \right)^2 \left[3 (\vec{\chi}_i \cdot \hat{\mathbf{L}}_N)^2 - \chi_i^2 \right] \right. \\
&\quad \left. + \frac{1}{96} \left(\frac{m_i}{M} \right)^2 \left[7\chi_i^2 - (\vec{\chi}_i \cdot \hat{\mathbf{L}}_N)^2 \right] \right\}, \\
\gamma &= \sum_{i=1}^2 \left[\left(\frac{732985}{2268} + \frac{140}{9} \eta \right) \left(\frac{m_i}{M} \right)^2 \right. \\
&\quad \left. + \eta \left(\frac{13915}{84} - \frac{10}{3} \eta \right) \right] \vec{\chi}_i \cdot \hat{\mathbf{L}}_N,
\end{aligned}$$

$$\begin{aligned}\xi &= \sum_{i=1}^2 \left[\frac{75\pi}{2} \left(\frac{m_i}{M} \right)^2 + \frac{151\pi}{6} \eta \right] \vec{\chi}_i \cdot \hat{L}_N, \\ \zeta &= \sum_{i=1}^2 \left[\left(\frac{m_i}{M} \right)^2 \left(\frac{130325}{756} - \frac{796069}{2016} \eta + \frac{100019}{864} \eta^2 \right) \right. \\ &\quad \left. + \eta \left(\frac{1195759}{18144} - \frac{257023}{1008} \eta + \frac{2903}{32} \eta^2 \right) \right] \vec{\chi}_i \cdot \hat{L}_N\end{aligned}$$

where q_i is a quadrupole-moment parameter, \hat{L}_N is the unit vector in the direction of the binary's orbital angular momentum, $\vec{\chi}_i = \vec{S}_i/m_i^2$ are the dimensionless spins of the i^{th} body, and $\chi_i = \vec{\chi}_i \cdot \hat{L}_N$. In the works that derive these pN corrections, q_i has been implicitly set to 1. This is the value it takes for spinning black holes but not the value it takes for neutron stars and possibly other spinning exotica [see for example Eq. (8) of E. (1998)]. However, we adopt the same simplification here since we will not be considering spinning systems outside of the Kerr class.

We reparameterize the component spins χ_i into an antisymmetric and a symmetric combination,

$$\vec{\chi}_s = \frac{1}{2} (\vec{\chi}_1 + \vec{\chi}_2) \quad (4.2.5)$$

$$\vec{\chi}_a = \frac{1}{2} (\vec{\chi}_1 - \vec{\chi}_2). \quad (4.2.6)$$

Recall that we restrict ourselves to spin-aligned (or antialigned), nonprecessing waveforms, which means $\chi_a \equiv \vec{\chi}_a \cdot \hat{L}_N = \pm |\vec{\chi}_a|$ and $\chi_s \equiv \vec{\chi}_s \cdot \hat{L}_N = \pm |\vec{\chi}_s|$. The positive sign corresponds to systems with (anti)symmetric spins aligned with the orbital angular momentum of the binary, and the negative sign corresponds to systems with (anti)symmetric spins antialigned with the binary's orbital angular momentum.

We also study nonspinning waveforms that include the 5.0 pN order tidal correction to the phase. Tidal corrections are calculated for the phase beyond 5.0 pN order (Damour et al. 2012). However, we find that the tidal corrections beyond 5.0 pN order in phase are completely unmeasurable by the Fisher matrix. Including these terms create a worse-conditioned Fisher matrix and does not affect the measurability of the 5.0 pN order tidal correction. Therefore, we omit all but the leading-order tidal correction in this work.

The point-particle contributions to the phase of the waveform are only calculated through 3.5 pN order (v_k^7 beyond leading order). The leading-order tidal correction to

the phase appears at 5.0 pN order (v_k^{10} beyond leading order). Therefore, the 5.0 pN 82 order term in the phase of the waveform does not include all point-particle effects to that order. The 5.0 pN order tidal term that adds linearly to Eq. (4.2.4) is

$$\delta\Psi_{\text{tidal}}(v_k) = -\frac{117\tilde{\Lambda}}{16\eta}v_k^5, \quad (4.2.7)$$

with $\tilde{\Lambda} = \tilde{\lambda}/M^5$ and

$$\tilde{\lambda} = \frac{1}{26} \left(\frac{m_1 + 12m_2}{m_1} \lambda_1 + \frac{m_2 + 12m_1}{m_2} \lambda_2 \right), \quad (4.2.8)$$

where λ_i is the tidal deformability parameter for component mass m_i (Hinderer et al. 2010). The tidal deformability parameter, which in this post-Newtonian description describes the ratio of the induced quadrupole moment to the perturbing external tidal field, is written in terms of the dimensionless tidal Love number k_2 (Hinderer et al. 2010) as

$$\lambda = \frac{2}{3}k_2r^5, \quad (4.2.9)$$

with r being the radius of the star. A fully relativistic generalization of this was provided in Binington & Poisson (2009), where it was shown that for nonrotating black holes, the relativistic Love numbers all vanish. Landry & Poisson (2015) also showed that the relativistic Love numbers vanish for slowly rotating black holes.

We examine two scenarios: spinning systems with no tidal corrections and nonspinning systems with tidal corrections. For spinning systems we “turn on” the 1.5 pN- to 2.5 pN order spin corrections in the phase by setting the parameter $\epsilon = 1$ in Eq. (4.2.4), and we “turn on” the 3.0 pN- and 3.5 pN order spin corrections in the phase by setting the parameter $\alpha = 1$. We also turn on or off the spin corrections in the amplitude of the waveform as derived in Arun et al. (2009). For nonspinning systems with tidal corrections, we turn off all of the spin corrections in the phase and the amplitude and add Eq. (4.2.7) linearly to Eq. (4.2.4) for the phase of the waveform. We do not include any tidal corrections in the amplitude of the waveform, because they have not yet been calculated.

4.3 Parameter estimation

4.3.1 Fisher matrix

We construct the covariance matrix using the Fisher information matrix formalism for a single detector to determine parameter errors and correlations. For a large enough signal-to-noise ratio (SNR), the measurement errors on the waveform parameters $\vec{\theta}$ given a gravitational waveform $\tilde{h}(f)$ fall into a Gaussian probability density function

$$p(\Delta\vec{\theta}) = \sqrt{\det\left(\frac{\mathbf{\Gamma}}{2\pi}\right)} e^{(-\frac{1}{2}\Gamma_{ij}\Delta\theta^i\Delta\theta^j)},$$

where $\mathbf{\Gamma}$ is the Fisher information matrix (Creighton & Anderson 2011; Cutler & Flanagan 1994). The components of the Fisher matrix are defined as

$$\Gamma_{ij} = \left(\frac{\partial h}{\partial \theta^i}, \frac{\partial h}{\partial \theta^j} \right) \Big|_{\vec{\theta}_{\max}}, \quad (4.3.1)$$

where h is the gravitational waveform, θ^i is a waveform parameter, $\vec{\theta}_{\max}$ is the set of true parameters, and $(\dots | \dots)$ is an inner product defined by

$$(a, b) = 4\text{Re} \int_0^\infty \frac{\tilde{a}(f)\tilde{b}^*(f)}{S_n(f)} df \quad (4.3.2)$$

for power spectral density $S_n(f)$ (see Sec. 3.1).

The root-mean-square error on a parameter θ^i is derived from the inverse Fisher matrix, which is the covariance matrix under certain assumptions (Vallisneri 2008),

$$(\Delta\theta^i)_{\text{rms}} = \sqrt{(\Gamma^{-1})^{ii}} \text{ (no summation over } i \text{)}. \quad (4.3.3)$$

The correlation between two parameters θ^i and θ^j is also derived from the inverse Fisher matrix,

$$c_{ij} = \frac{(\Gamma^{-1})^{ij}}{\sqrt{(\Gamma^{-1})^{ii}(\Gamma^{-1})^{jj}}} \text{ (no summation over } i \text{ or } j \text{)}. \quad (4.3.4)$$

4.3.2 Validity of the Fisher matrix

The Fisher matrix provides an approximation to the covariance matrix that represents the Cramer-Rao bound (Vallisneri 2008). Studies using the Fisher matrix in the context of gravitational-wave parameter estimation are vast in the literature (e.g. Poisson & Will

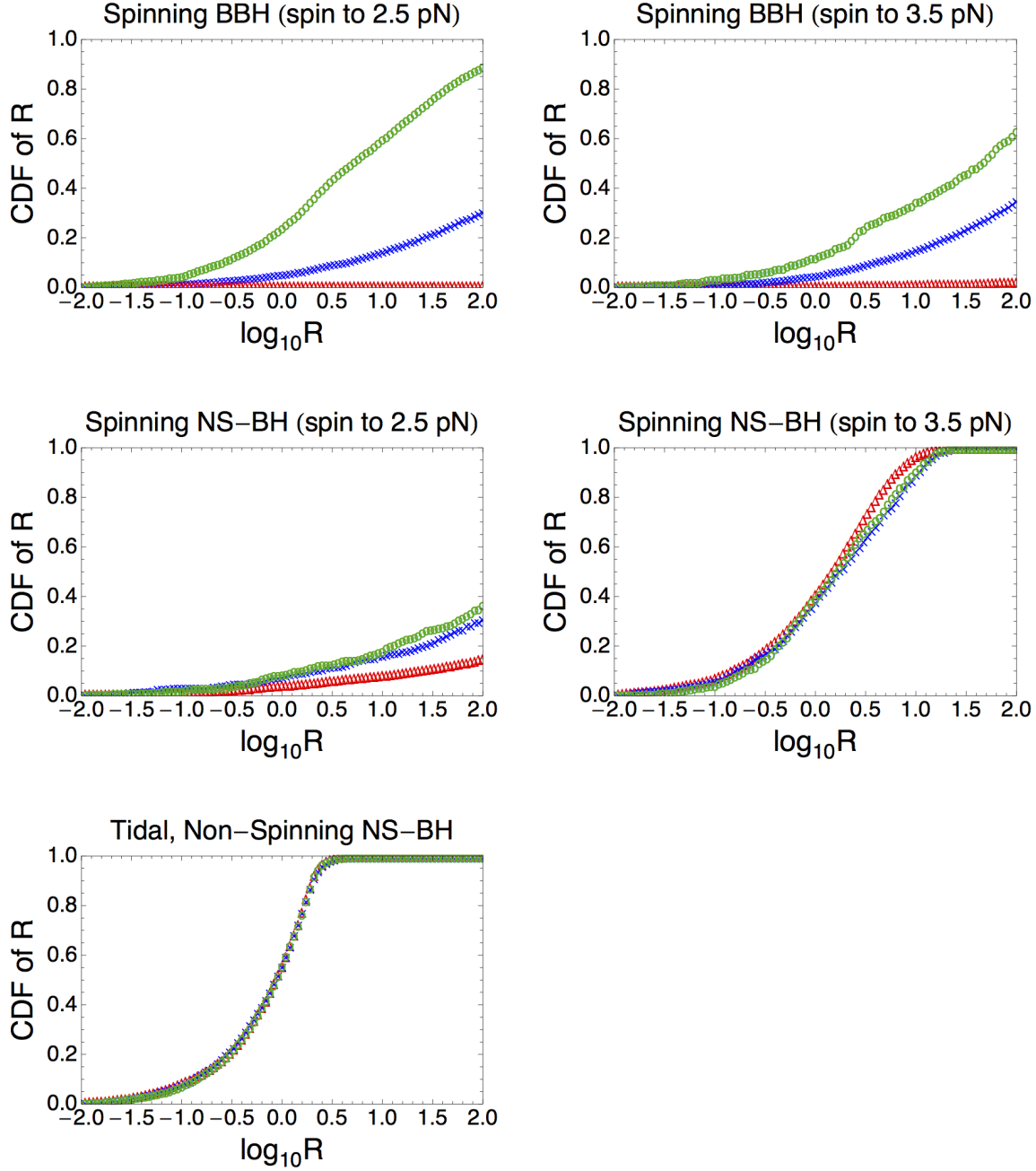


Figure 28 : The cumulative distribution function (CDF) for the quantity $\log_{10} R$ where $R \equiv |\log r|$. The quantity R , defined in Eq. (4.3.5), is a measure of the self-consistency of the Fisher matrix. This quantity is calculated at 5000 random points on the 1σ -error surface, and the CDF of these points is plotted here. The smaller values of R indicate a more self-consistent Fisher matrix. Therefore, the most self-consistent Fisher matrix calculations have a CDF of R that rises quickly. Above we plot $\log_{10} R$ for a spinning BBH system ($m_1 = 10 M_\odot$, $m_2 = 11 M_\odot$), a spinning NS-BH system ($m_1 = 1.4 M_\odot$, $m_2 = 10 M_\odot$), and a tidal BBH system ($m_1 = 10 M_\odot$, $m_2 = 11 M_\odot$) all with $t_c = 0$, $\phi_c = 0$, $\theta = \pi/6$, $\phi = \pi/6$, $\psi = \pi/4$ and $\iota = \pi/3$ and with a fixed SNR of $\rho = 100$. For the spinning BBH system, the component spins are $\chi_1 = \chi_2 = 1$, for the spinning NS-BH system the component spins are $\chi_1 = 0$ and $\chi_2 = 1$, and for the nonspinning, tidal BBH system the tidal deformability parameter is $\tilde{\Lambda} = 0$. The 1σ -error estimates employed in this calculation were obtained from a five- or four-parameter Fisher matrix calculation with $\vec{\theta} = \{\log \mathcal{M}, \eta, t_c, \chi_a, \chi_s\}$ or $\vec{\theta} = \{\log \mathcal{M}, \eta, t_c, \tilde{\Lambda}\}$ for the spinning systems and the tidal system, respectively. The plot shows results for the Newtonian-amplitude waveform (red triangles), the 0.5 pN order amplitude-corrected waveform (blue X's), and the 1.0 pN order amplitude-corrected waveform (green circles), with spin corrections included in the amplitude for the spinning systems. The spinning-system plot titles indicate which spin corrections are kept in the phase of the waveform.

(1995), Cutler & Flanagan (1994), Finn (1992), Nielsen (2013), Hinderer et al. (2010), and Van Den Broeck & Sengupta (2007)). However, there are several drawbacks in employing the Fisher matrix for parameter estimation studies. The derivation of the Fisher matrix requires the linearized signal approximation (LSA), which is only valid in the high-SNR limit (Vallisneri 2008). Real gravitational-wave detections in the advanced-detector era are not expected to fall into the high-SNR limit (Abadie et al. 2010). In addition, the Fisher matrix assumes a Gaussian, single-modal distribution of the likelihood function (Vallisneri 2008; Rodriguez et al. 2013). In reality, the likelihood could be very non-Gaussian and multimodal. The Fisher matrix does not fully explore the parameter space but rather focuses on one point in parameter space and assumes a Gaussian likelihood about this point. In reality, a full Bayesian calculation of the likelihood function starting from the raw data and using techniques such as MCMC to explore parameter space is required for accurate parameter estimation, which has also been studied extensively in the literature (e.g. Van Der Sluys et al. (2008a), Van Der Sluys et al. (2008b), Veitch & Vecchio (2010), Raymond et al. (2010), Veitch et al. (2012), the LIGO Scientific Collaboration et al. (2013), and Rodriguez et al. (2013)). Rodriguez et al. (2013) perform an in-depth comparison of the Fisher matrix with a full Bayesian MCMC study and find that the Fisher matrix can be very ill suited to parameter estimation for certain systems. Below, we perform some tests to verify the validity of the Fisher matrix approach in our work.

Vallisneri (2008) discusses a self-consistency check for the Fisher matrix. To determine the level of self-consistency of the Fisher matrix, we calculate

$$|\log r| = \frac{1}{2} \left((\Delta\theta^j)_{\text{rms}} h_j - \Delta h \mid (\Delta\theta^k)_{\text{rms}} h_k - \Delta h \right) \quad (4.3.5)$$

where $h_j = \partial h / \partial \theta_j |_{\vec{\theta}_{\text{max}}}$, $\Delta h = h |_{\vec{\theta}_{1\sigma}} - h |_{\vec{\theta}_{\text{max}}}$, and $\vec{\theta}_{1\sigma}$ is a point in parameter space that lies on the 1σ -error surface. The value of $|\log r|$ will depend on the SNR, since the 1σ -error surface and parameter root-mean-square errors are a function of SNR.

Fig. 28 plots the cumulative distribution function of $\log_{10} R$ ($R \equiv |\log r|$) calculated for a large number of random points on the 1σ -error surface at a fixed SNR of 100 for the Newtonian-amplitude waveform (red triangles), the 0.5 pN order amplitude-corrected waveform (blue X's), and the 1.0 pN order amplitude-corrected waveform (green circles),

with spin corrections included in the amplitude for the spinning systems. The 1σ -error surface used in the calculation of $|\log r|$ came from a five- or four-parameter Fisher matrix calculation with $\vec{\theta} = \{\log \mathcal{M}, \eta, t_c, \chi_a, \chi_s\}$ or $\vec{\theta} = \{\log \mathcal{M}, \eta, t_c, \tilde{\Lambda}\}$ for the spinning systems and the nonspinning, tidal system, respectively. Fig. 28 shows results for the spinning systems both with and without the 3.0 pN- and 3.5 pN order spin corrections to the phase.

Fig. 28 indicates that the approximations necessary for the Fisher matrix formalism to be self-consistent, such as the linearized signal approximation (LSA), are more valid for the 1.0 pN order amplitude-corrected waveform with spin corrections in the amplitude when compared to the Newtonian-amplitude waveform and the 0.5 pN order amplitude-corrected waveform for the spinning systems. In addition, including the 3.0 pN- and 3.5 pN order spin corrections to the phase for the NS-BH system leads to significant improvement in the self-consistency of the Fisher matrix. However, the spinning BBH system is either left unchanged or made slightly less valid by including these higher-order spin-orbit corrections. For the nonspinning, tidal BBH system, all of the waveforms prove equally valid.

Vallisneri (2008) notes that the LSA will be more valid for parameter spaces with weaker correlations. As will be discussed in Sec. 4.5, the amplitude-corrected waveforms cause certain parameters that are strongly correlated in the Newtonian-amplitude waveform to decouple for the spinning BBH system. Parameter correlations are broken when moving both from the Newtonian-amplitude waveform to the 0.5 pN order amplitude-corrected waveform and from the 0.5 pN order amplitude-corrected waveform to the spin-dependent 1.0 pN order amplitude-corrected waveform. Degeneracies are also slightly decreased when including the 3.0 pN- and 3.5 pN order spin corrections in the phase for the spinning NS-BH system but mostly unchanged for the spinning BBH system.

Fig. 28 is a good reference for the self-consistency of the Fisher matrix for different orders of the post-Newtonian expansion. The scale of $|\log r|$ indicates that the Fisher matrix may only be self-consistent for high SNR. Therefore, we perform an additional investigation into the validity of the Fisher matrix below. The results of this investigation conclude that the Fisher matrix should give fairly reliable results for the cases we study,

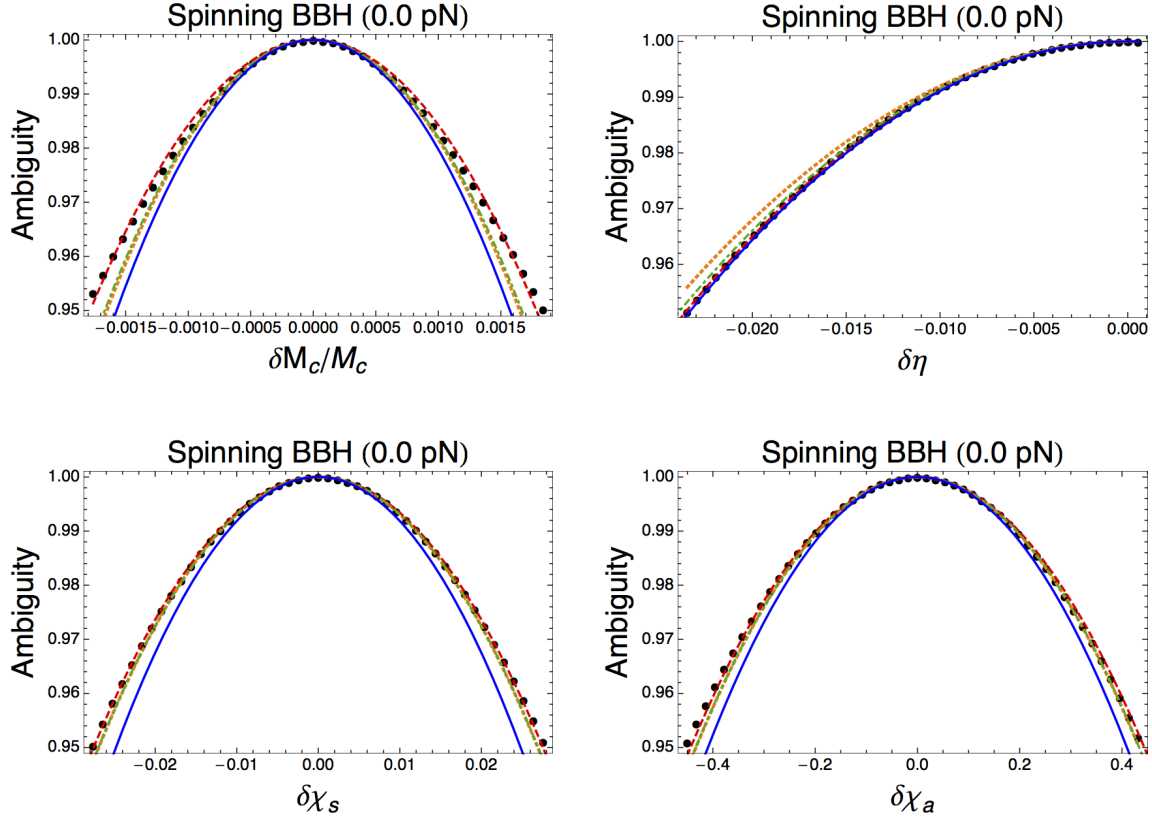


Figure 29 : The ambiguity function for different systems, as indicated by the title of each plot, over the most relevant parameters to this work, $\{\mathcal{M}, \eta, \chi_s, \chi_a\}$. The amplitude pN order is 0.0 pN for these plots. In each plot, the parameter on the x axis is varied while all other parameters are held fixed at fiducial values (see Sec. 4.4). Each plot also shows quadratic fits over three different scales: $P \geq 0.95$ (red dashed line), $P \geq 0.99$ (green dot-dashed line), and $P \geq 0.999$ (blue solid line). The actual ambiguity function is shown with black dots. The fit lines are all fairly close to each other, which indicates that the likelihood for these systems is fairly Gaussian over the relevant scale. In addition, the orange, dotted line shows the quadratic fit predicted from the Fisher matrix, which is also in good agreement.

even for a SNR of 10.

The Fisher matrix involves the partial derivative of the waveform with respect to a set of parameters. In order for the Fisher matrix approximation to be valid, the likelihood needs to be fairly Gaussian on scales appropriate to the SNR being studied. One way to examine the Gaussianity of the likelihood would be through the ambiguity function P , defined in Cho et al. (2013) as

$$P(\vec{\theta}_{\max}, \vec{\theta}) = \max_{t_c, \psi} \frac{(h_{\vec{\theta}_{\max}} | h_{\vec{\theta}})}{\sqrt{(h_{\vec{\theta}_{\max}} | h_{\vec{\theta}_{\max}}) (h_{\vec{\theta}} | h_{\vec{\theta}})}} \quad (4.3.6)$$

where $\max_{t_c, \psi}$ means a maximization over coalescence time and polarization angle, as described in Cho et al. (2013). The ambiguity function is a measure of the overlap between the true waveform with parameters $\vec{\theta}_{\max}$ and a waveform described by parameters $\vec{\theta}$.

If the likelihood is Gaussian, the ambiguity function should fit well to a quadratic curve (Cho et al. 2013). The scale over which the ambiguity function should be quadratic is determined by the SNR. For a SNR of ρ , the ambiguity function should be well fit to the same Gaussian over scales up to $P \geq 1 - 1/\rho^2$ (Cho et al. 2013). Throughout this work, we mainly study a SNR of $\rho = 10$, so the scale of interest for the ambiguity function is $P \geq 0.99$. For completeness, we examine the ambiguity function on scales $P \geq 0.95$. Fig. 29 shows the ambiguity function over the most relevant parameters to this work, $\{\mathcal{M}, \eta, \chi_s, \chi_a\}$. In each plot, the parameter on the x -axis is varied while all other parameters are held fixed at fiducial values, which are outlined for the previous validity test. Each plot also shows quadratic fits over three different scales: $P \geq 0.95$ (red dashed line), $P \geq 0.99$ (green dot-dashed line), and $P \geq 0.999$ (blue solid line). The actual ambiguity function is shown with black dots. Although we only show plots for the spinning BBH system in the Newtonian-amplitude, the plots look very similar for the different systems studied in this work and across different post-Newtonian approximations to the amplitude and phase. The quadratic fits across different scales match up well. This test indicates that the likelihood is appropriately Gaussian for the SNR we study.

Fig. 29 also shows the quadratic fit as predicted by the Fisher matrix (orange dotted line). The comparison between ambiguity and the Fisher matrix is most simply seen by examining the logarithm of the Gaussian likelihood, as retrieved from Eqs. (17) and (22) in Cho et al. (2013), for example. The one-dimensional ambiguity function over parameter θ_i not maximized over t_c or ψ , denoted below as \tilde{P} , is simply related to the relevant Fisher matrix component Γ_{ii} ,

$$\tilde{P} = 1 - \frac{1}{2} \frac{\Gamma_{ii}}{\rho^2} (\Delta\theta_i)^2 \quad (\text{no summation over } i). \quad (4.3.7)$$

However, to make a more direct comparison with the normalized ambiguity function maximized over t_c and ψ , the parameters D_M , t_c , and ψ should be projected out of the Fisher matrix. Projecting out these three parameters is achieved by computing a four-dimensional Fisher matrix including the parameters of interest, D_M , t_c , and ψ , inverting this matrix, and taking the inverse of the relevant component $[(\Gamma^{-1})^{ii}]^{-1}$. The orange

dotted lines plotted in Fig. 29 are for the quadratic fit,

$$P = 1 - \frac{1}{2} \frac{[(\Gamma^{-1})^{ii}]^{-1}}{\rho^2} (\Delta\theta_i)^2 \quad (\text{no summation over } i),$$

where θ_i is either \mathcal{M} , η , χ_s , or χ_a . These fits are very consistent with the ambiguity function calculation in all cases.

Qualitatively, we expect the Fisher matrix results to be accurate. Quantitatively, the Fisher matrix results will be most accurate for a high SNR. The results in this work are provided for an SNR of 10. The Fisher matrix results scale very simply from an SNR of 10 if the reader wishes to study different SNR scenarios. Other sources of quantitative error that may exceed the errors introduced by the Fisher matrix are errors associated with the inaccuracies of the post-Newtonian waveforms. When working with real data, additional quantitative errors, such as calibration errors, can also become significant. This work is intended to give insight into the ability of aLIGO to study tests of general relativity in a mainly qualitative manner. This study should motivate full Bayesian studies that will be required to investigate low-SNR scenarios quantitatively.

4.3.3 Singular-value decomposition

The parameter spaces that we investigate can be 11 or 10 dimensional; see Eqs. (4.4.1) and (4.4.3). In these multidimensional parameter spaces, the Fisher matrix is often singular or badly conditioned and therefore difficult to invert. One way we address this is by using a singular-value decomposition (SVD) on the Fisher matrix (Pai & Arun 2013). The SVD of a matrix $\mathbf{\Gamma}$ is

$$\mathbf{\Gamma} = \mathbf{U}\mathbf{S}\mathbf{V}^\dagger, \quad (4.3.8)$$

where \mathbf{S} is a diagonal matrix whose diagonal elements contain the singular values, and \mathbf{U} and \mathbf{V} are unitary matrices of the left and right singular vectors, respectively. The covariance matrix in terms of its singular-value decomposition is

$$\mathbf{\Gamma}^{-1} = \mathbf{V}\mathbf{S}^{-1}\mathbf{U}^\dagger.$$

Since the Fisher matrix is real and symmetric by definition, for our case we have $\mathbf{V} = \mathbf{U}$ and this matrix will be an orthogonal matrix of the real eigenvectors of $\mathbf{\Gamma}$.

If the Fisher matrix is singular or badly conditioned, its singular values will be zero or very small. We remove the singular or badly conditioned pieces of the Fisher matrix by zeroing out the elements of \mathbf{S}^{-1} that are very large or infinite. These elements correspond to the zero or very small singular values of the Fisher matrix, which become infinite or very large upon inversion. Zeroing out these elements is effectively removing the unmeasurable linear combinations of parameters from the Fisher matrix. In this way we are able to obtain error estimates for only the measurable parameters, and we do not have to assume *a priori* which are the measurable parameters.

4.4 Parameters and parameter space bounds

4.4.1 Spinning waveform

For the spinning waveform described in Sec. 4.2, the full parameter space is 11 dimensional,

$$\vec{\theta}_{\text{spin,full}} = \{\log(1/D_M), \log \mathcal{M}, \eta, t_c, \phi_c, \cos \iota, \chi_a, \chi_s, \cos \theta, \phi, \psi\} \quad (4.4.1)$$

where ι is the inclination angle of the binary, θ and ϕ are the sky position polar coordinates, ψ is the polarization angle, and χ_s and χ_a are the symmetric and antisymmetric spin parameters described in Sec. 4.2. We use true values of $t_c = 0$, $\phi_c = 0$, $\iota = \pi/3$, $\theta = \pi/6$, $\phi = \pi/6$, and $\psi = \pi/4$ for all of the results reported here. All calculations are performed for a fixed SNR, which determines the value of D_M for each calculation. The component masses and spins are varied as described in Sec. 4.5.1.

We find that a smaller dimensional parameter space is required to obtain reliable results from the Fisher matrix when performing calculations with the Newtonian-amplitude spinning waveform, even when employing the SVD method described in Sec. 4.3. For the Newtonian-amplitude spinning waveform calculations, we use a reduced six-dimensional parameter space:

$$\vec{\theta}_{\text{spin,reduced}} = \{\log(1/D_M), \log \mathcal{M}, \eta, t_c, \chi_a, \chi_s\} . \quad (4.4.2)$$

For this reduced parameter space, we use true values of $t_c = 0$, $\phi_c = 0$, $\iota = \pi/3$, $\theta = \pi/6$, $\phi = \pi/6$, and $\psi = \pi/4$, and we vary component masses and spins as described in Sec. 4.5.1.

Once again, the fixed SNR for each calculation determines the value of D_M for that system.

We exploit bounds on the symmetric mass ratio and the Kerr parameter to reduce the acceptable parameter space. The physical bounds on m_1 and m_2 and the definition of the symmetric mass ratio restrict η to be between 0 and 1/4. For Kerr solutions, cosmic censorship requires $|\vec{\chi}_i| \leq 1$, which restricts $|\vec{\chi}_s|$ and $|\vec{\chi}_a|$ to be less than or equal to 1. The bounds on spin and the symmetric mass ratio create a finite region of $\chi_{s,a} - \eta$ parameter space that is both physical and consistent with a Kerr black hole. Excluding the unphysical areas of η parameter space is not imposed as a flat prior in the Fisher matrix calculation but is applied after the fact to the error ellipse that results from an unrestricted Fisher matrix calculation. A more detailed discussion on the improved measurability of spin by restricting the spin-mass parameter space can be found in Sec. 4.5.1.

For amplitude-corrected waveforms, the 11-dimensional parameter space given in Eq. (4.4.1) often leads to a badly conditioned or singular Fisher matrix. We use the singular-value decomposition method discussed in Sec. 4.3 to invert the Fisher matrix and discover the unmeasurable linear combinations of parameters. For the Newtonian-amplitude waveform all of the parameters in the reduced parameter space $\vec{\theta}_{\text{spin, reduced}}$ are measurable. For the lowest-order amplitude-corrected waveform (0.5 pN), the measurable parameters are \mathcal{M} , η , t_c , ϕ_c , $\cos \iota$, χ_a , and χ_s . For the 1.0 pN order amplitude-corrected waveform, the measurable parameters are \mathcal{M} , η , t_c , ϕ_c , $\cos \iota$, χ_a , χ_s , and ϕ . In Sec. 4.5.1 we only report on the measurement errors for \mathcal{M} , η , χ_s and χ_a , since these are the most pertinent to our study.

4.4.2 Nonspinning, tidal waveform

For the nonspinning, tidal waveform described in Sec. 4.2, we investigate a 10-dimensional parameter space,

$$\vec{\theta}_{\text{tidal}} = \left\{ \log(1/D_M), \log \mathcal{M}, \eta, t_c, \phi_c, \cos \iota, \tilde{\Lambda}, \cos \theta, \phi, \psi \right\}. \quad (4.4.3)$$

We use true values of $t_c = 0$, $\phi_c = 0$, $\iota = \pi/3$, $\theta = \pi/6$, $\phi = \pi/6$, and $\psi = \pi/4$ for all of the results reported here. All calculations are performed for a fixed SNR, which

determines the value of D_M for each calculation. The component masses and the tidal parameter are varied as described in Sec. 4.5.2.

As was the case with the spinning waveform, the tidal parameter space also has bounds with useful physical interpretations. We explore how exploiting the physical bound on the symmetric mass ratio ($0 < \eta \leq 1/4$) affects the measurability of the tidal parameter. In addition, we place a bound on the tidal deformability parameter ($\tilde{\Lambda} = 0$) for the waveform to be consistent with expectations from the no-hair theorem, in the sense described in Sec. 4.1. Previous work on tidal deformability calculations for compact systems (Damour & Nagar 2009) suggests that $\delta\Psi_{\text{tidal}}$ should be zero or small for black holes. The closest matter analog would be an incompressible star at maximum compactness ($c = m/r = 4/9$), for which the tidal Love number would be $k_2 = 0.0017103$ (Damour & Nagar 2009). For an equal mass, equal radius binary system, the parameter $\tilde{\Lambda}$ is

$$\tilde{\Lambda} = \frac{\tilde{\lambda}}{(2m)^5} = \frac{\lambda}{(2m)^5} = \frac{1}{48}k_2 \left(\frac{r}{m}\right)^5$$

where the above follows from the definition of $\tilde{\lambda}$ (given by Eq. (4.2.8)) for an equal mass system, λ is the tidal parameter for one component object as defined in Eq. (4.2.9), r is the radius of one component object, and m is the mass of one component object. Using the ratio of m/r for maximum compactness in the above expression gives $\tilde{\Lambda} \approx 0.002$. Therefore, it is reasonable to conclude that the parameter $\tilde{\Lambda}$ should be small, if not identically zero, for black holes. There could potentially be internal structure effects appearing at 5.0 pN order in the phase that differ from the point particle approximation, but these effects should be undetectable for a black hole to have no hair. Therefore, we take $\delta\Psi_{\text{tidal}} = 0$, which implies $\tilde{\Lambda} = 0$, for a nonspinning black hole with no hair. For the most comprehensive aLIGO test of the no-hair theorem, it would be more appropriate to use numerical relativity waveforms with various realizations of internal structure parameterized by $\tilde{\Lambda}$.

Just as with the spinning waveform, this 10-dimensional parameter space often leads to a badly conditioned or singular Fisher matrix. Using the method described in Sec. 4.3, we determine the measurable parameters for each waveform. For the Newtonian-amplitude waveform, the measurable parameters are \mathcal{M} , η , t_c , and $\tilde{\Lambda}$. For the lowest-order amplitude-corrected waveform (0.5 pN), the measurable parameters are \mathcal{M} , η , t_c , ϕ_c , $\cos \iota$,

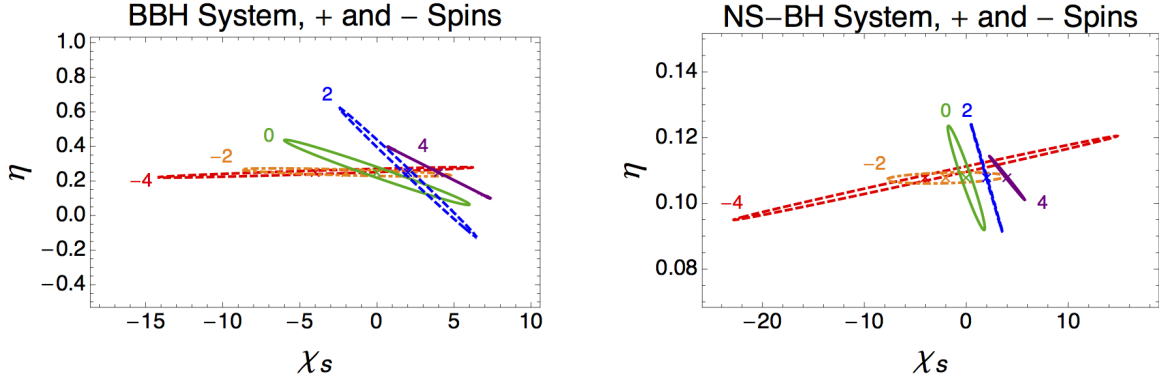


Figure 30 : The 1σ error ellipses in the $\eta - \chi_s$ parameter space for a spinning Newtonian-amplitude waveform with spin corrections in the phase to 2.5 pN order as described in Sec. 4.2 and with the reduced parameter space $\vec{\theta}_{\text{spin, reduced}}$ given in Eq. (4.4.2). These ellipses are calculated for a spinning BBH system with $m_1 = 10 M_\odot$ and $m_2 = 11 M_\odot$ (left plot) and a spinning NS-BH system with $m_1 = 1.4 M_\odot$ and $m_2 = 10 M_\odot$ (right plot). Both systems have true parameters $t_c = 0$, $\phi_c = 0$, $\theta = \pi/6$, $\phi = \pi/6$, $\psi = \pi/4$ and $\iota = \pi/3$ and a fixed SNR of $\rho = 10$. For the BBH system, the component spins are varied from $\chi_1 = \chi_2 = -4$ (red dashed ellipse) to $\chi_1 = \chi_2 = 4$ (purple solid ellipse). Each ellipse takes a step of 2 in component spins. For the NS-BH system, the component spins are varied from $\chi_1 = 0$, $\chi_2 = -8$ (red dashed ellipse) to $\chi_1 = 0$, $\chi_2 = 8$ (purple, solid ellipse). Each ellipse takes a step of 2 in χ_s , which corresponds to the black hole taking a step of 4 in its component spin. The neutron star spin is held fixed at zero. The numbers near each ellipse indicate the χ_s value for that ellipse (color coded).

and $\tilde{\Lambda}$. For the 1.0 pN order amplitude-corrected waveforms, ϕ also becomes measurable. In Sec. 4.5.2 we only report on the measurement errors for \mathcal{M} , η , and $\tilde{\Lambda}$, since these are the most pertinent to our study.

4.5 Results

4.5.1 Detectable apparent violations of the cosmic censorship conjecture

We study two different spinning systems: a near equal mass binary black hole (BBH) system with component masses $m_1 = 10 M_\odot$ and $m_2 = 11 M_\odot$ and a neutron-star-black-hole (NS-BH) system with component masses $m_1 = 1.4 M_\odot$ and $m_2 = 10 M_\odot$. The exactly equal mass limit is avoided due to singularities in the Fisher matrix at the equal mass limit when including amplitude corrections. Both systems are parameterized as described by Eqs. (4.4.1) or (4.4.2) and are subject to the parameter space bounds discussed in Sec. 4.4.1. We use the spinning waveform described in Sec. 4.2 with the phase kept to 3.5 pN order and the amplitude varied from 0.0 pN to 2.5 pN order. Spin corrections are always included in the phase to 2.5 pN order. We study the effect of

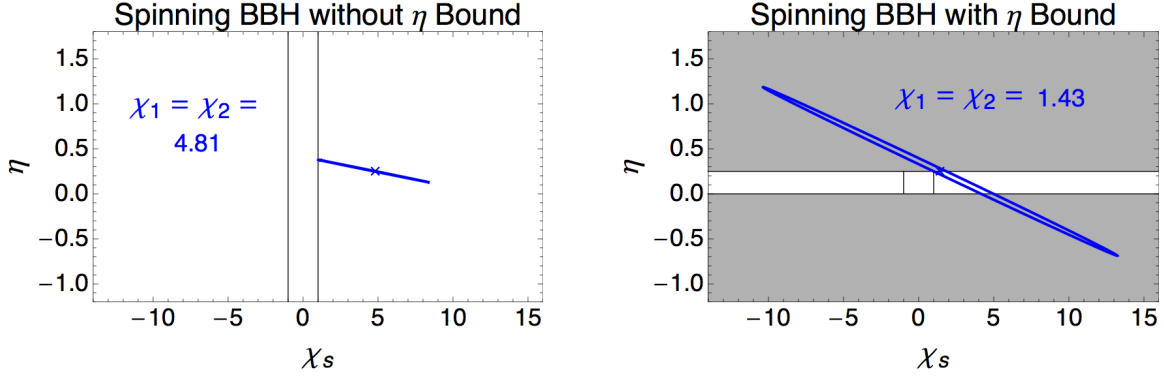


Figure 31 : The 1σ error ellipses in the $\eta - \chi_s$ parameter space for a spinning Newtonian-amplitude waveform with spin corrections in the phase to 2.5 pN order as described in Sec. 4.2 and with the reduced parameter space $\vec{\theta}_{\text{spin, reduced}}$ given in Eq. (4.4.2). These ellipses are calculated for a spinning BBH system with $m_1 = 10 M_\odot$, $m_2 = 11 M_\odot$, $t_c = 0$, $\phi_c = 0$, $\theta = \pi/6$, $\phi = \pi/6$, $\psi = \pi/4$ and $\iota = \pi/3$ and with a fixed SNR of $\rho = 10$. The component spins for each ellipse are given as an inlay on the plot. The plot on the left shows the minimum detectable violation of the Kerr bound when considering the entire parameter space. The plot on the right shows the minimum detectable violation of the Kerr bound when only considering the parts of the error ellipse that are physical. The unphysical areas of parameter space are shaded gray in the plot on the right. The vertical solid lines bound the region of parameter space that is consistent with the Kerr bound ($-1 \leq \chi_s \leq 1$).

turning on or off spin corrections in the amplitude of the waveform and turning on or off the 3.0 pN and 3.5 pN order spin corrections in the phase.

We use the zero detuned, high power aLIGO power spectrum as given in Shoemaker (2009) for the power spectral density $S_n(f)$. The inner product integrations are carried out from $f_{\text{min}} = 10$ Hz to $f_{\text{max}} = kF_{\text{LSO}}$ where (Creighton & Anderson 2011)

$$F_{\text{LSO}} = \frac{1}{6^{3/2} 2\pi M} . \quad (4.5.1)$$

We choose to only examine positive (aligned) spins when determining the minimum detectable violation of the Kerr spin bound. Negative (anti-aligned) spins are not as well measured as positive spins, and therefore will lead to a larger minimum detectable violation of the Kerr bound. Fig. 30 shows the 1σ error ellipses as produced by the Fisher matrix for both the spinning BBH system and the spinning NS-BH system. Each ellipse is calculated for different values of component spin. Fig. 30 demonstrates how positive spins are more measurable than negative spins and therefore more useful in determining the minimum detectable violation. The figure also illustrates how parameter measurability varies significantly for different values of spin for the BBH system and the NS-BH system.

One goal of our work with spinning black hole systems is to investigate how much

better aLIGO would be able to detect a violation of the Kerr bound ($\chi_i > 1$) when only the physical area of η parameter space is considered (see Sec. 4.4.1 for a discussion of parameter space bounds). As mentioned before, this is not done by imposing a flat prior on the Fisher matrix. Rather, an unrestricted Fisher matrix calculation is performed. We examine the 1σ error ellipses in the $\eta - \chi_s$ or $\eta - \chi_a$ plane and determine if the entire physical area of the ellipse is consistent or inconsistent with the Kerr bound. We explore the parameter space until we find the minimum $\chi_i = j_i/(m_i)^2$ that violate the Kerr bound when considering only physical parts of the error ellipse. As can be seen in Tables 2– 5, the parameter χ_s is better measured than the parameter χ_a . As discussed above and shown in Fig. 30, positive spins are also better measured than negative spins. Therefore, we determine the minimum violation of the $\chi_s = 1$ bound in order to determine the minimum violation of the Kerr bound.

Fig. 31 compares the minimally violating spin values for a Newtonian-amplitude waveform when considering the entire parameter space (left plot) versus considering only the physical area of parameter space (right plot). The error ellipse on the right of Fig. 31 is consistent with the Kerr bound when considering the entire parameter space, but it is inconsistent with the Kerr bound when considering only the area of the ellipse within the physically-allowed region of η . Results are shown for only the spinning BBH system. The spinning NS-BH system is not affected by bounding values of η due to the error ellipse's orientation and placement in parameter space, as is evident in Fig. 33.

The strong correlation between the symmetric mass ratio η and spin when using a Newtonian-amplitude waveform has been studied by Baird et al. (2013) and Nielsen (2013), among others. The correlation between mass and spin can be seen in Figs. 31, 32 and 33. As a result, the spin parameters are not well measured with the Newtonian-amplitude waveform when considering the full $\eta - \chi_s$ parameter space. However, by restricting the parameter space to only the physical region of η for the spinning BBH system, aLIGO's ability to detect violations of the Kerr bound increases by about a factor of three. This result is also summarized in Table 2.

We examine how the measurability of spin is affected by including spin-independent and spin-dependent amplitude corrections. The measurability of spin for waveforms with

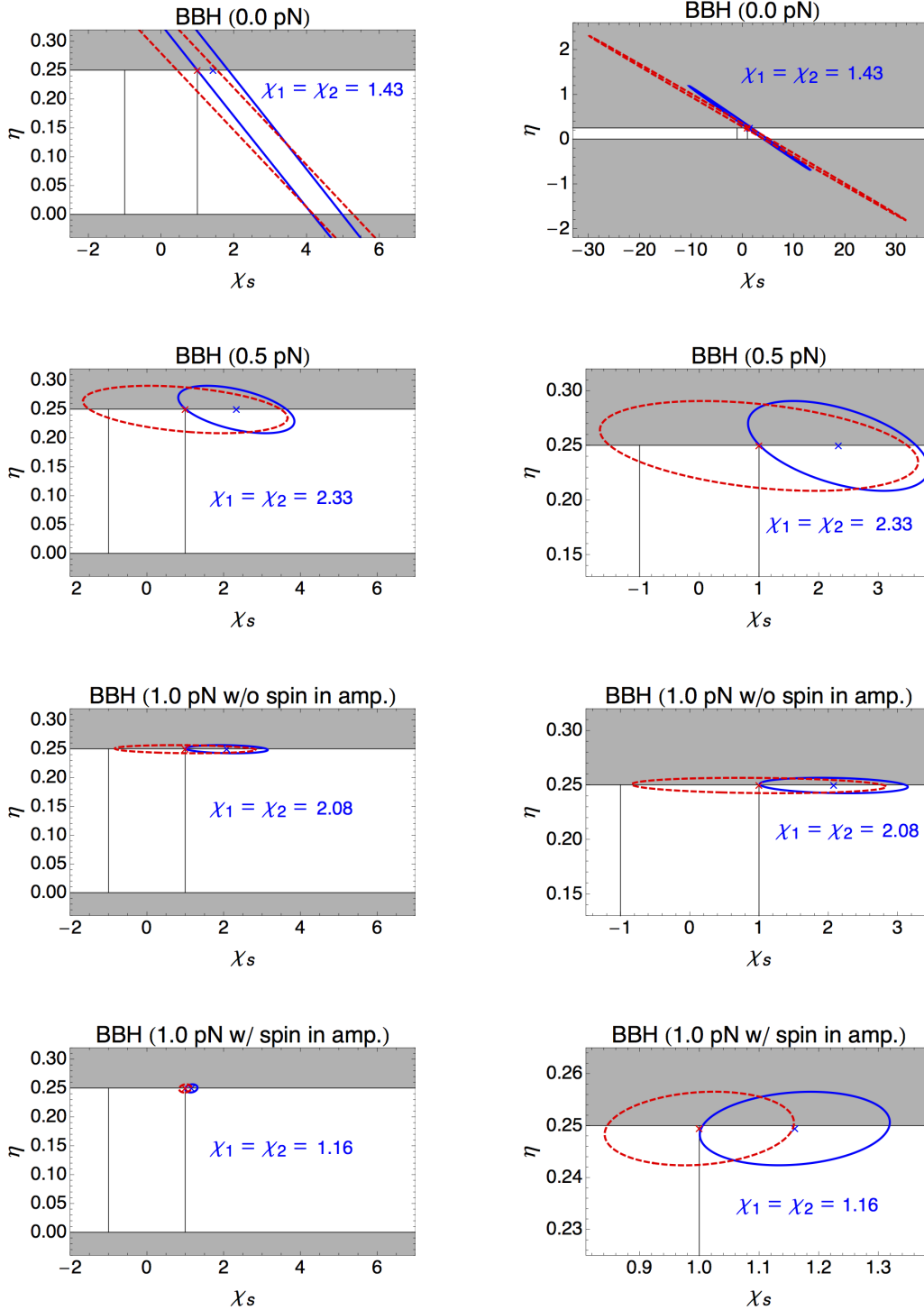


Figure 32 : The σ error ellipses in the $\eta - \chi_s$ parameter space for various spinning, amplitude-corrected waveforms with spin corrections in the phase to 2.5 pN order as described in Sec. 4.2. The title of each plot indicates the pN order amplitude correction. For the 1.0 pN order amplitude-corrected waveform, the title also indicates whether spin corrections have been included in the amplitude. These ellipses are calculated for a spinning BBH system with true parameters $m_1 = 10 M_\odot$, $m_2 = 11 M_\odot$, $t_c = 0$, $\phi_c = 0$, $\theta = \pi/6$, $\phi = \pi/6$, $\psi = \pi/4$ and $\iota = \pi/3$ and with a fixed SNR of $\rho = 10$. The component spins for the solid, blue ellipses are given as an inlay on the plot. These spins indicate the minimum detectable apparent violation of cosmic censorship. The dashed, red ellipses are calculated with the fiducial spin values of $\chi_1 = \chi_2 = 1$ in each plot. The plots on the left are all to the same scale for comparison purposes. The plots on the right are shown to a scale appropriate for each ellipse. The unphysical areas of parameter space are shaded gray. The vertical solid lines bound the region of parameter space that is consistent with cosmic censorship ($-1 \leq \chi_s \leq 1$).

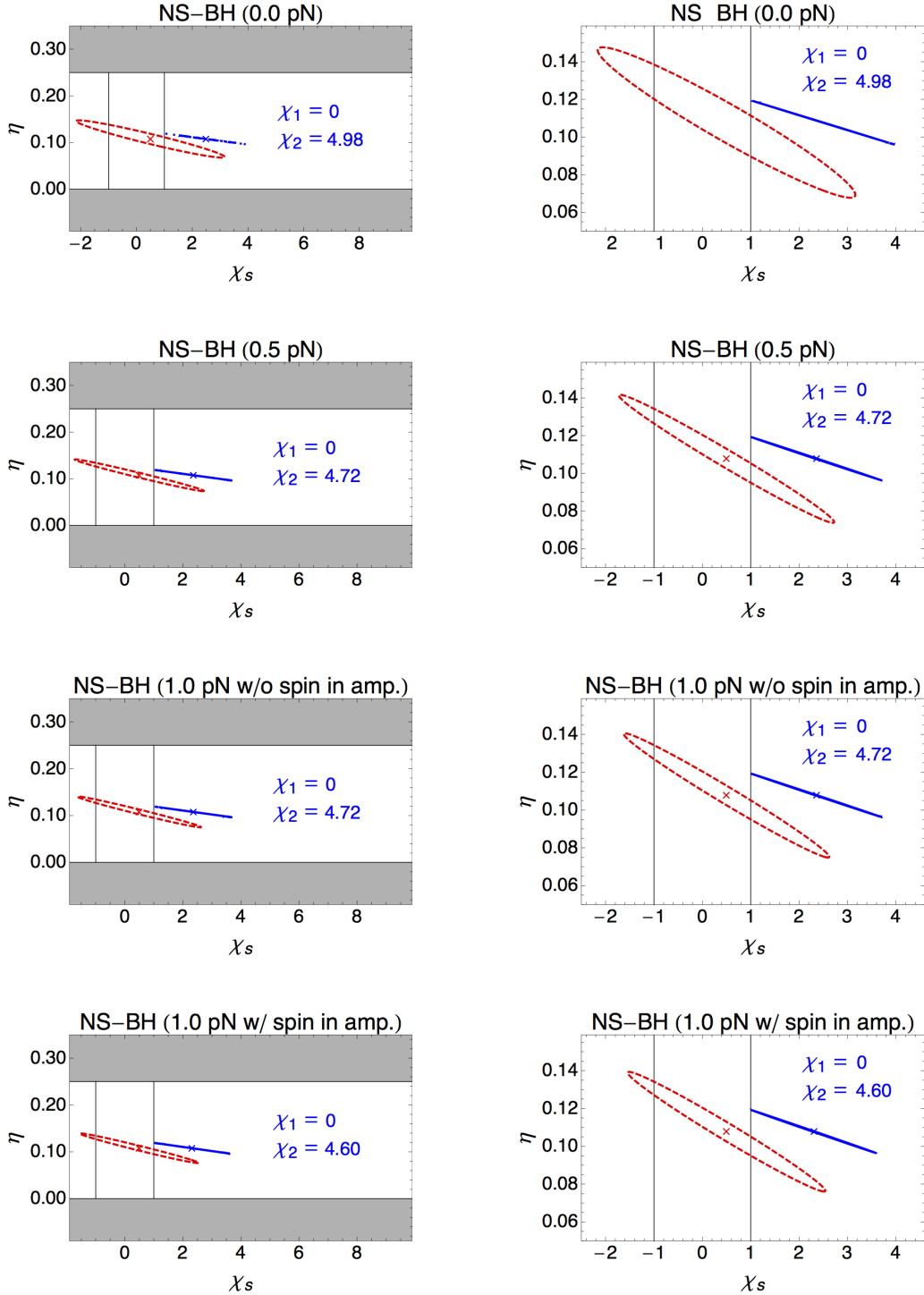


Figure 33 : The 1σ error ellipses in the $\eta - \chi_s$ parameter space for various spinning, amplitude-corrected waveforms with spin corrections in the phase to 2.5 pN order as described in Sec. 4.2. The title of each plot indicates the pN order amplitude correction. For the 1.0 pN order amplitude-corrected waveform, the title also indicates whether spin corrections have been included in the amplitude. These ellipses are calculated for a spinning NS-BH system with true parameters $m_1 = 1.4 M_\odot$, $m_2 = 10 M_\odot$, $t_c = 0$, $\phi_c = 0$, $\theta = \pi/6$, $\phi = \pi/6$, $\psi = \pi/4$ and $\iota = \pi/3$ and with a fixed SNR of $\rho = 10$. The component spins for the solid, blue ellipses are given as an inlay on the plot. These spins indicate the minimum detectable apparent violation of cosmic censorship. The dashed, red ellipses are calculated with the fiducial spin values of $\chi_1 = 0$ and $\chi_2 = 1$ in each plot. The plots on the left are all to the same scale for comparison purposes. The plots on the right are shown to a scale appropriate for each ellipse. The unphysical areas of parameter space are shaded gray. The vertical solid lines bound the region of parameter space that is consistent with cosmic censorship ($-1 \leq \chi_s \leq 1$).

Table 2 : **Spinning BBH System** This table shows results for the spinning BBH system with true parameters $m_1 = 10 M_\odot$, $m_2 = 11 M_\odot$, $t_c = 0$, $\phi_c = 0$, $\theta = \pi/6$, $\phi = \pi/6$, $\psi = \pi/4$ and $\iota = \pi/3$ and with a fixed SNR of $\rho = 10$. The spins χ_1 and χ_2 for each scenario are given in the tables. The tables show the 1σ measurement errors and correlation coefficients obtained from the Fisher matrix using spinning waveforms as described in Sec. 4.2 with spin corrections in the phase to 2.5 pN order. Also given in the tables is the distance D_M in units of Mpc of the system in order to achieve the fixed SNR of 10. Different order amplitude corrections, with and without spin in the amplitude, are given in different rows of the tables. The top table shows results for fiducial spin values of $\chi_1 = \chi_2 = 1$, and the bottom table shows results for the minimum detectable violating spins for each waveform. The first row of the bottom table is for the minimum violating spin when the entire η parameter space is considered, and the second row is when only the physical η parameter space is considered.

pN order in amp.	$\chi_1 = \chi_2$	D_M	$\Delta\mathcal{M}/\mathcal{M}$	$\Delta\eta$	$\Delta\chi_a$	$\Delta\chi_s$	$c_{\eta\chi_s}$	$c_{\mathcal{M}\chi_s}$
0.0 pN	1	938	0.0367	2.06	522.2	30.8	-0.9998	0.9989
0.5 pN	1	938	0.00420	0.0411	42.2	2.66	-0.3543	0.9197
1.0 pN	1	879	0.00328	0.00704	28.8	1.84	-0.1541	0.8777
1.5 pN	1	879	0.00339	0.00807	30.5	1.94	-0.1422	0.8844
2.0 pN	1	851	0.00360	0.00752	34.3	2.18	-0.1646	0.8979
2.5 pN	1	851	0.00329	0.00766	29.4	1.87	-0.1491	0.8790
1.0 pN + spin	1	879	0.00164	0.00709	2.84	0.159	0.1568	0.3184
1.5 pN + spin	1	935	0.00168	0.00882	2.56	0.167	0.2238	0.3168
2.0 pN + spin	1	901	0.00167	0.00809	2.44	0.159	0.1734	0.3169
2.5 pN + spin	1	902	0.00166	0.00825	2.44	0.159	0.1741	0.3201

pN order in amp.	$\chi_1 = \chi_2$	D_M	$\Delta\mathcal{M}/\mathcal{M}$	$\Delta\eta$	$\Delta\chi_a$	$\Delta\chi_s$	$c_{\eta\chi_s}$	$c_{\mathcal{M}\chi_s}$
0.0 pN (w/o η bound)	4.81	938	0.00609	0.129	103.2	3.81	-0.9998	-0.9452
0.0 pN (w/ η bound)	1.43	938	0.00918	0.936	226.3	11.8	-0.9994	0.9757
0.5 pN	2.33	938	0.00377	0.0411	23.6	1.51	-0.5014	0.8082
1.0 pN	2.08	879	0.00304	0.00709	15.0	1.07	-0.1851	0.8390
1.5 pN	2.12	879	0.00316	0.00810	15.7	1.12	-0.1737	0.8479
2.0 pN	2.21	850	0.00335	0.00755	16.7	1.21	-0.1995	0.8652
2.5 pN	2.09	851	0.00307	0.00769	15.2	1.09	-0.1809	0.8409
1.0 pN + spin	1.16	879	0.00165	0.00708	2.40	0.159	0.1693	0.3344
1.5 pN + spin	1.18	945	0.00170	0.00891	2.57	0.172	0.2471	0.3383
2.0 pN + spin	1.17	909	0.00169	0.00815	2.45	0.163	0.1891	0.3339
2.5 pN + spin	1.17	909	0.00168	0.00831	2.45	0.164	0.1916	0.3381

Table 3 : Spinning BBH System with 3.0 pN and 3.5 pN Spin-Orbit Phase Terms This table shows results for the spinning BBH system with true parameters $m_1 = 10 M_\odot$, $m_2 = 11 M_\odot$, $t_c = 0$, $\phi_c = 0$, $\chi_1 = \chi_2 = 1$, $\theta = \pi/6$, $\phi = \pi/6$, $\psi = \pi/4$ and $\iota = \pi/3$ and with a fixed SNR of $\rho = 10$. The table shows the 1σ measurement errors and correlation coefficients obtained from the Fisher matrix using spinning waveforms as described in Sec. 4.2 with spin corrections in the phase to 3.5 pN order. Also given in the table is the distance D_M in units of Mpc of the system in order to achieve the fixed SNR of 10. Different order amplitude corrections, with and without spin in the amplitude, are given in different rows of the table.

pN order in amplitude	$\chi_1 = \chi_2$	D_M	$\Delta\mathcal{M}/\mathcal{M}$	$\Delta\eta$	$\Delta\chi_a$	$\Delta\chi_s$	$c_{\eta\chi_s}$	$c_{\mathcal{M}\chi_s}$
0.0 pN	1	938	0.00431	0.0681	14.9	1.09	0.9173	0.8811
0.5 pN	1	938	0.00419	0.0358	20.9	1.14	0.1460	0.9062
1.0 pN	1	879	0.00309	0.00697	16.8	1.13	0.1315	0.8686
1.5 pN	1	879	0.00324	0.00798	17.5	1.17	0.1155	0.8788
2.0 pN	1	850	0.00356	0.00742	19.4	1.30	0.1271	0.9000
2.5 pN	1	851	0.00314	0.00757	17.4	1.16	0.1237	0.8736
1.0 pN + spin	1	879	0.00165	0.00707	2.42	0.166	0.1995	0.4112
1.5 pN + spin	1	935	0.00172	0.00880	2.55	0.176	0.2628	0.4319
2.0 pN + spin	1	901	0.00172	0.00806	2.44	0.168	0.2106	0.4303
2.5 pN + spin	1	902	0.00169	0.00822	2.43	0.168	0.2140	0.4224

spin corrections included in the phase but only spin-independent amplitude corrections was reported in Van Den Broeck & Sengupta (2007). Since then, more accurate spin corrections to the phase and spin corrections to the amplitude have been calculated. As described in Sec. 4.2, here we use the waveforms given in Arun et al. (2009), which include spin corrections in the amplitude to 2.0 pN order and spin corrections in the phase to 2.5 pN order. Later in this section we address the more recent spin-orbit corrections at 3.0 pN and 3.5 pN order in the phase.

The results for different order amplitude corrections, with and without spin corrections in the amplitude, are shown in Fig. 32 and Table 2 for the BBH system and in Fig. 33 and Table 4 for the NS-BH system. The plots in Figs. 32 and 33 show 1σ error ellipses for fiducial spin values of $\chi_1 = \chi_2 = 1$ for the BBH system and $\chi_1 = 0$, $\chi_2 = 1$ for the NS-BH system (red, dashed ellipses). In addition, the plots show 1σ error ellipses for the minimum detectable violation of the Kerr bound (blue, solid ellipses). The top table in Tables 2 and 4 show parameter root-mean-square errors and correlation coefficients for

Table 4 : **Spinning NS-BH System** This table shows results for the spinning NS-BH system with true parameters $m_1 = 1.4 M_\odot$, $m_2 = 10 M_\odot$, $t_c = 0$, $\phi_c = 0$, $\theta = \pi/6$, $\phi = \pi/6$, $\psi = \pi/4$ and $\iota = \pi/3$ and with a fixed SNR of $\rho = 10$. The spins χ_1 and χ_2 for each scenario are given in the tables. The tables show the 1σ measurement errors and correlation coefficients obtained from the Fisher matrix using spinning waveforms as described in Sec. 4.2 with spin corrections in the phase to 2.5 pN order. Also given in the table is the distance D_M in units of Mpc of the system in order to achieve the fixed SNR of 10. Different order amplitude corrections, with and without spin in the amplitude, are given in different rows of the tables. The top table shows results for fiducial spin values of $\chi_1 = 0$ and $\chi_2 = 1$, and the bottom table shows results for the minimum detectable violating black hole spin for each waveform. The first row of the bottom table is for the minimum violating spin when the entire η parameter space is considered, and the second row of the bottom table is for the minimum violating spin when only the physical η parameter space is considered.

pN order in amplitude	χ_1	χ_2	D_M	$\Delta\mathcal{M}/\mathcal{M}$	$\Delta\eta$	$\Delta\chi_a$	$\Delta\chi_s$	$c_{\eta\chi_s}$	$c_{\mathcal{M}\chi_s}$
0.0 pN	0	1	383	0.00199	0.0399	3.30	2.66	-0.9929	0.9981
0.5 pN	0	1	391	0.00164	0.0340	2.76	2.22	-0.9879	0.9964
1.0 pN	0	1	364	0.00156	0.0329	2.64	2.12	-0.9875	0.9965
1.5 pN	0	1	361	0.00159	0.0335	2.68	2.16	-0.9869	0.9963
2.0 pN	0	1	356	0.00159	0.0336	2.68	2.16	-0.9474	0.9965
2.5 pN	0	1	355	0.00158	0.0336	2.68	2.15	-0.9868	0.9964
1.0 pN + spin	0	1	363	0.00150	0.0316	2.53	2.04	-0.9864	0.9962
1.5 pN + spin	0	1	376	0.00154	0.0322	2.59	2.09	-0.9859	0.9958
2.0 pN + spin	0	1	371	0.00154	0.0323	2.59	2.08	-0.9861	0.9960
2.5 pN + spin	0	1	370	0.00154	0.0323	2.59	2.08	-0.9859	0.9959

pN order in amplitude	χ_1	χ_2	D_M	$\Delta\mathcal{M}/\mathcal{M}$	$\Delta\eta$	$\Delta\chi_a$	$\Delta\chi_s$	$c_{\eta\chi_s}$	$c_{\mathcal{M}\chi_s}$
0.0 pN	0	4.98	383	0.000469	0.0118	2.33	1.49	-0.99996	-0.7490
0.5 pN	0	4.72	391	0.000381	0.0115	2.11	1.35	-0.9998	-0.6461
1.0 pN	0	4.72	364	0.000357	0.0115	2.11	1.35	-0.9998	-0.6148
1.5 pN	0	4.78	362	0.000359	0.0115	2.14	1.37	-0.9998	-0.6162
2.0 pN	0	4.84	358	0.000361	0.0116	2.19	1.41	-0.9998	-0.6277
2.5 pN	0	4.84	356	0.000360	0.0117	2.21	1.42	-0.9998	-0.6232
1.0 pN + spin	0	4.60	365	0.000337	0.0115	2.03	1.30	-0.9997	-0.5566
1.5 pN + spin	0	4.52	435	0.000382	0.0114	1.97	1.26	-0.9995	-0.6175
2.0 pN + spin	0	4.50	430	0.000372	0.0113	1.94	1.24	-0.9995	-0.5960
2.5 pN + spin	0	4.50	429	0.000371	0.0113	1.94	1.24	-0.9994	-0.5914

Table 5 : **Spinning NS-BH System with 3.0 pN and 3.5 pN Spin-Orbit Phase Terms** This table shows results for the spinning NS-BH system with true parameters $m_1 = 1.4 M_\odot$, $m_2 = 10 M_\odot$, $t_c = 0$, $\phi_c = 0$, $\chi_1 = 0$, $\chi_2 = 1$, $\theta = \pi/6$, $\phi = \pi/6$, $\psi = \pi/4$ and $\iota = \pi/3$ and with a fixed SNR of $\rho = 10$. The table shows the 1σ measurement errors and correlation coefficients obtained from the Fisher matrix using spinning waveforms as described in Sec. 4.2 with spin corrections in the phase to 3.5 pN order. Also given in the table is the distance D_M in units of Mpc of the system in order to achieve the fixed SNR of 10. Different order amplitude corrections, with and without spin in the amplitude, are given in different rows of the table.

pN order in amplitude	χ_1	χ_2	D_M	$\Delta M/M$	$\Delta\eta$	$\Delta\chi_a$	$\Delta\chi_s$	$c_{\eta\chi_s}$	$c_{M\chi_s}$
0.0 pN	0	1	383	0.000452	0.00527	1.05	0.900	0.8153	0.9208
0.5 pN	0	1	390	0.000396	0.00480	0.956	0.822	0.7442	0.9138
1.0 pN	0	1	364	0.000387	0.00462	0.968	0.831	0.7350	0.9181
1.5 pN	0	1	361	0.000394	0.00469	0.991	0.850	0.7251	0.9192
2.0 pN	0	1	356	0.000397	0.00465	1.01	0.868	0.7222	0.9222
2.5 pN	0	1	355	0.000399	0.00466	1.02	0.876	0.7182	0.9229
1.0 pN + spin	0	1	363	0.000385	0.00461	0.963	0.827	0.7324	0.9173
1.5 pN + spin	0	1	376	0.000390	0.00474	0.954	0.819	0.7295	0.9137
2.0 pN + spin	0	1	371	0.000392	0.00471	0.969	0.832	0.7293	0.9162
2.5 pN + spin	0	1	370	0.000393	0.00472	0.976	0.838	0.7251	0.9167

the fiducial spin values. The bottom table in Tables 2 and 4 show parameter errors and correlation coefficients for the systems that provide the minimum detectable violation of the Kerr bound with each waveform.

The BBH system is strongly affected by including amplitude corrections in the waveform and spin corrections in the amplitude. There is about a factor-of-ten improvement in the measurability of the spin parameters when the lowest-order amplitude correction (0.5 pN) is included in the waveform and the spin terms in the phase are kept to 2.5 pN order. Van Den Broeck & Sengupta (2007) also report on improved measurability of spin when amplitude corrections are included in the waveform. A notable effect in our calculations is that the symmetric mass ratio decouples from spin and many other waveform parameters when the first-order amplitude correction is included in the waveform.³ There is additional improvement in spin and mass measurability when the 1.0

³Since the correlation between symmetric mass ratio and spin is decreased when using amplitude-corrected waveforms, restricting the error ellipse to only the physical area of η parameter space does not significantly improve aLIGO's ability to detect apparent violations of cosmic censorship with these

pN order amplitude correction is included in the waveform, and there is a slight decrease¹⁰² in the degeneracy between spin and chirp mass for this waveform. Furthermore, when spin corrections are included in the amplitude, which occurs at lowest-order at 1.0 pN, the measurability of spin improves by an additional factor of about ten. In this case, including spin corrections in the amplitude breaks the correlation between chirp mass and spin even further.

The spinning NS-BH system is not strongly affected by including spin-dependent or nonspinning amplitude corrections. There is a slight improvement in parameter measurability when moving from the Newtonian-amplitude waveform to the amplitude-corrected waveform, but this effect is not nearly as significant as with the spinning BBH system. There is an even less significant improvement in parameter measurability for the spinning NS-BH system when moving from nonspinning amplitude corrections to spin-dependent amplitude corrections. Overall, the Newtonian-amplitude spinning NS-BH waveform performs equally well as the amplitude-corrected waveforms when it comes to parameter measurability.

We do a brief study of how parameter measurability is affected by the 3.0 pN and 3.5 pN order spin-orbit corrections to the phase (Marsat et al. 2013). Tables 3 and 5 show the 1σ errors and correlation coefficients from the Fisher matrix for the spinning BBH system and the spinning NS-BH system, respectively, with spin corrections in the phase to 3.5 pN order and the amplitude corrections varied as described in the table.

The BBH system and the NS-BH system are both affected in some way by the 3.0 pN and 3.5 pN order spin-orbit terms in the phase. For the BBH system, there is more than a factor-of-ten improvement in the symmetric mass ratio and spin parameter measurability for the Newtonian-amplitude waveform, and there is about a factor-of-ten improvement in the chirp mass measurability. The degeneracy between the chirp mass and the spin is slightly decreased when the 3.0 pN and 3.5 pN order spin terms in the phase are included in the Newtonian-amplitude waveform, which may be what leads to the improved measurability of mass and spin. The amplitude-corrected waveforms without spin in the amplitude show improved measurability of about a factor of two for the spin but not the waveforms. This is evident from the plots in Fig. 32.

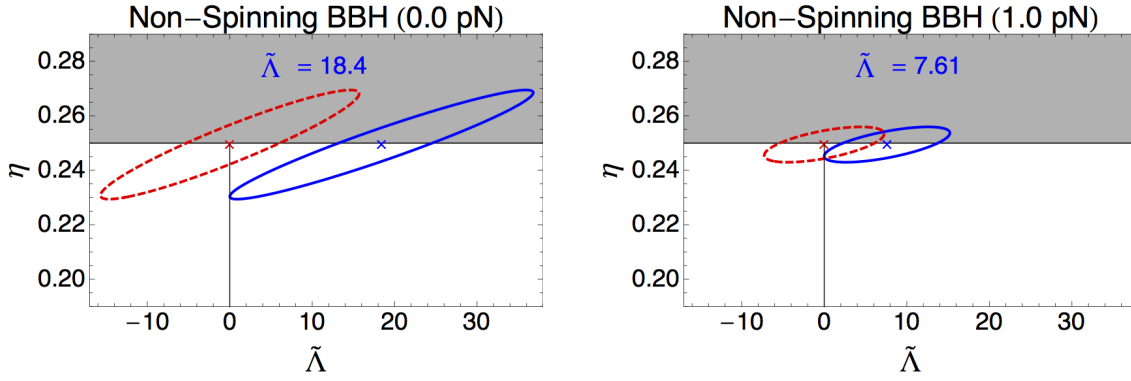


Figure 34 : The 1σ error ellipses in the $\eta - \tilde{\Lambda}$ parameter space for nonspinning, tidal waveforms, as described in Sec. 4.2. The title of each plot indicates the pN order amplitude correction. These ellipses were calculated for a BBH system with true parameters $m_1 = 10 M_\odot$, $m_2 = 11 M_\odot$, $t_c = 0$, $\phi_c = 0$, $\theta = \pi/6$, $\phi = \pi/6$, $\psi = \pi/4$ and $\iota = \pi/3$ and with a fixed SNR of $\rho = 10$. The tidal parameter $\tilde{\Lambda}$ for the solid, blue ellipses is given as an inlay on the plot. These tidal deformability parameters indicate the minimum detectable deviation from the no-hair theorem for each waveform. The dashed, red ellipses are shown for the fiducial tidal value of $\tilde{\Lambda} = 0$ in each plot. The unphysical areas of parameter space are shaded gray. The $\tilde{\Lambda} = 0$ axis indicates the area of parameter space that is consistent with the no-hair theorem. Both plots above are shown to the same scale for comparison purposes.

mass parameters, and the amplitude-corrected waveforms with spin corrections in the amplitude are minimally affected by the 3.0 pN and 3.5 pN order spin-orbit corrections to the phase.

For all of the different amplitude-corrected waveforms, the spinning NS-BH system shows about a factor-of-ten improvement in the measurability of the mass parameters when the 3.0 pN and 3.5 pN order spin-orbit corrections are included in the phase and about a factor of three improvement in the measurability of the spin parameters. The 3.0 pN and 3.5 pN order spin-orbit phase corrections decrease the degeneracy between the symmetric mass ratio and the spin parameters, which may lead to the improved parameter measurability in this case.

4.5.2 Detectable deviations from the no-hair theorem

In this section we discuss aLIGO's ability to detect deviations from the no-hair theorem using nonspinning, tidal waveforms, as described in Sec. 4.2. We keep the phase to 5.0 pN order, where point-particle calculations are known to 3.5 pN order and the leading order tidal correction appears at 5.0 pN order (point-particle corrections to 4.0, 4.5, and 5.0 pN orders are neglected). We vary the amplitude corrections from 0.0 pN to 2.5

Table 6 : Nonspinning Tidal BBH System This table shows results for the nonspinning BBH system with true parameters $m_1 = 10 M_\odot$, $m_2 = 11 M_\odot$, $t_c = 0$, $\phi_c = 0$, $\theta = \pi/6$, $\phi = \pi/6$, $\psi = \pi/4$ and $\iota = \pi/3$ and with a fixed SNR of $\rho = 10$. The tidal deformability parameter $\tilde{\Lambda}$ for each scenario is given in the tables. The tables show the 1σ measurement errors and correlation coefficients obtained from the Fisher matrix using the tidal waveform as described in Sec. 4.2. Also given in the table is the distance D_M in units of Mpc of the system in order to achieve the fixed SNR of 10. The phase is kept out to 3.5 pN order and different order amplitude corrections are given in different rows of the tables. The top table shows results for a fiducial tidal parameter value of $\tilde{\Lambda} = 0$, and the bottom table shows results for the minimum detectable violating tides for each waveform.

pN order in amplitude	$\tilde{\Lambda}$	D_M	$\Delta\mathcal{M}/\mathcal{M}$	$\Delta\eta$	$\Delta\tilde{\Lambda}$	$c_{\eta\tilde{\Lambda}}$	$c_{\mathcal{M}\tilde{\Lambda}}$
0.0 pN	0	938	0.00281	0.0200	15.7	0.9326	0.8305
0.5 pN	0	938	0.00234	0.0102	13.1	0.9019	0.7575
1.0 pN	0	879	0.00115	0.00649	7.26	0.6090	0.1241
1.5 pN	0	879	0.00123	0.00723	7.64	0.6569	0.2192
2.0 pN	0	851	0.00118	0.00694	7.77	0.6375	0.1778
2.5 pN	0	851	0.00118	0.00693	7.71	0.6331	0.1758
pN order in amplitude	$\tilde{\Lambda}$	D_M	$\Delta\mathcal{M}/\mathcal{M}$	$\Delta\eta$	$\Delta\tilde{\Lambda}$	$c_{\eta\tilde{\Lambda}}$	$c_{\mathcal{M}\tilde{\Lambda}}$
0.0 pN	18.4	938	0.00281	0.0200	18.4	0.9512	0.8581
0.5 pN	14.4	938	0.00232	0.0160	14.3	0.9193	0.7809
1.0 pN	7.61	879	0.00115	0.00649	7.61	0.6537	0.1723
1.5 pN	8.13	879	0.00123	0.00730	8.12	0.7039	0.2747
2.0 pN	8.19	850	0.00118	0.00698	8.18	0.6831	0.2308
2.5 pN	8.16	851	0.00118	0.00697	8.15	0.6811	0.2305

pN order. We do not include any tidal corrections in the amplitude of the waveform,¹⁰⁵ since they are not yet calculated. We only investigate heavy systems, nominally BBH systems, without spin. We look at a near equal mass BBH system with component masses $m_1 = 10 M_\odot$ and $m_2 = 11 M_\odot$. As with the spinning system, the exactly equal mass limit is avoided due to singularities in the amplitude-corrected waveforms at this limit. The BBH system is parameterized as described in Sec. 4.4.2. We use the zero detuned, high power aLIGO power spectrum (Shoemaker 2009) for the power spectral density, and we perform inner product integrations from $f_{\min} = 10$ Hz to $f_{\max} = kF_{\text{LSO}}$, where F_{LSO} is defined in Eq. (4.5.1).

We investigate how both excluding the unphysical values of the symmetric mass ratio and including different order amplitude corrections to the waveform affect aLIGO's ability to detect deviations from the no-hair theorem expectations, as described in Sec. 4.4.2. The bounds on the symmetric mass ratio parameter space do not decrease the minimum detectable deviation from the no-hair theorem due to the orientation of the 1σ error ellipses in the $\eta - \tilde{\Lambda}$ plane, as illustrated in Fig. 34. The amplitude corrections do have a noticeable affect on the measurability of tidal deformability. While the lowest-order amplitude correction (0.5 pN) does not lead to a dramatic improvement in the measurability of the tidal parameter $\tilde{\Lambda}$, the 1.0 pN order amplitude correction does give about a factor of two improvement in the measurement error on $\tilde{\Lambda}$. The tidal parameter is strongly correlated to both the symmetric mass ratio and the chirp mass, but these correlations are decreased, especially between chirp mass and $\tilde{\Lambda}$, when using the 1.0 pN order amplitude-corrected waveform. The results are summarized in Fig. 34 and Table 6 for both the fiducial tidal parameter value of $\tilde{\Lambda} = 0$ and for the minimum detectable violating $\tilde{\Lambda}$.

Applying physical limits on the symmetric mass ratio can have a noticeable impact on aLIGO's ability to measure spin. When considering a near equal mass, spinning BBH system, aLIGO's ability to test the cosmic censorship conjecture is improved by about a factor of three by excluding unphysical values of the symmetric mass ratio for a Newtonian-amplitude waveform, as can be seen in Fig. 31 and Table 2. The frequency domain waveform given in Eq. (4.2.2) with a Newtonian-amplitude is commonly used for detection and parameter estimation efforts. The strong correlations between the symmetric mass ratio and spins result in poor measurability of the spin parameters when using this waveform. However, our results imply that including a prior on the symmetric mass ratio can lead to a significant improvement of spin measurability for near equal mass, spinning BBH systems. We find that a prior on the symmetric mass ratio will not affect unequal mass systems, as can be seen in Fig. 33, nor will it affect near equal mass systems when amplitude-corrected waveforms are employed, as can be seen in Fig. 32.

We find that switching from the Newtonian-amplitude waveform to the amplitude-corrected waveform significantly affects parameter measurability for the near-equal mass, spinning BBH system, but not for the unequal mass, spinning NS-BH system. Amplitude corrections add multiple harmonics to the gravitational waveform. The Newtonian-amplitude waveform only includes the second harmonic. However, the 0.5 pN order amplitude-corrected waveform adds the lowest-order point particle correction to the first and third harmonics. The 1.0 pN order amplitude-corrected waveform adds a spin correction to the first harmonic, a point particle correction to the second harmonic and the lowest-order point particle correction to the fourth harmonic. Parameter measurability for the spinning BBH system is most significantly affected by the 0.5 pN order point particle correction terms in the first and third harmonics and the 1.0 pN order spin correction terms in the first harmonic. The higher order amplitude correction terms above 1.0 pN order minimally affect parameter measurability.

For the spinning BBH system, the lowest-order amplitude correction improves the measurement error for chirp mass and spin parameters by about a factor-of-ten and for

the symmetric mass ratio by about a factor of fifty when compared to the Newtonian-¹⁰⁷ amplitude waveform. This translates to about a factor of two improvement on the minimum detectable spins that violate the cosmic censorship conjecture when compared to the Newtonian-amplitude waveform using the full symmetric mass ratio parameter space. The improved measurability may be due to the breaking of the degeneracy between the symmetric mass ratio and the spin parameters.

The spinning BBH system shows significant improvement in parameter measurability again when the lowest-order spin corrections are added to the amplitude, but the spinning NS-BH system shows no significant change by including spin terms to the amplitude, as is seen in Tables 2 and 4 and Figs. 32 and 33. For the spinning BBH system, the lowest-order spin corrections to the amplitude result in more than a factor-of-ten improvement in the measurability of both spin parameters when compared to the 1.0 pN order amplitude-corrected waveform without spin corrections in the amplitude. The improved measurability may be a result of decoupling chirp mass from spin. There is also about a factor of two improvement in the measurability of chirp mass when the lowest-order spin corrections are included in the amplitude. Including spin corrections in the amplitude leads to about a factor of two improvement in the ability of aLIGO to detect violations of cosmic censorship for a near equal mass BBH system.

A brief study of how the 3.0 pN and 3.5 pN order spin-orbit phase corrections affect parameter measurability, summarized in Tables 3 and 5, indicates that these corrections can have a noticeable impact on the spinning BBH system and the spinning NS-BH system.

For the spinning BBH system, including the newer spin-orbit phase corrections leads to significant improvement in mass and spin measurability and a decrease in the degeneracy between spin and chirp mass for the Newtonian-amplitude waveform. There is also some improvement in the measurability of the spin parameters for the amplitude-corrected waveforms without spin terms in the amplitude. However, the amplitude-corrected waveforms with spin terms in the amplitude are mostly unaffected by the 3.0 pN and 3.5 pN order spin-orbit phase terms.

The spinning NS-BH system demonstrates improved measurability for all different

orders of amplitude corrections in the mass and spin parameters when the 3.0 pN and 3.5 pN order spin-orbit phase terms are included in the waveform. More follow-up studies should be done to see how the 3.0 pN and 3.5 pN order spin-orbit phase corrections affect aLIGO's ability to detect apparent violations of the cosmic censorship conjecture.

In summary, aLIGO can theoretically detect spin violations of the cosmic censorship conjecture at 1σ for an SNR of 10 (or 3σ for an SNR of 30) for a near equal mass BBH system with component spins as small as $\chi_1 = \chi_2 = 1.16$ when using 1.0 pN order amplitude-corrected waveforms with spin corrections in the amplitude. In addition, aLIGO can theoretically detect a spin violation at 1σ for an SNR of 10 (or 3σ for an SNR of 30) for a spinning NS-BH system with $m_1 = 1.4 M_\odot$, $m_2 = 10 M_\odot$, $\chi_1 = 0$ and $\chi_2 = 4.50$ when using the 2.0 pN or 2.5 pN order amplitude-corrected waveform with spin corrections in the amplitude.

As discussed in Sec. 4.5.2, excluding unphysical values of the symmetric mass ratio does not affect aLIGO's ability to test whether the requirements of the no-hair theorem are fulfilled. However, including amplitude corrections in the waveform does noticeably affect the measurability of the tidal deformability parameter $\tilde{\Lambda}$, as shown in Table 6 and Fig. 34, which improves aLIGO's ability to detect deviations from the no-hair theorem. There is some small improvement in parameter measurability when including the 0.5 pN order amplitude correction. However, there is about a factor of two improvement in measurement error for both mass parameters and the tidal parameter when moving to the 1.0 pN order amplitude-corrected waveform. Note that for the nonspinning BBH system examined in Sec. 4.5.2, no spin corrections were included in the amplitude. Therefore, the 1.0 pN order amplitude correction only adds a point particle correction to the second and fourth harmonic. The tidal parameter $\tilde{\Lambda}$ is coupled to both the symmetric mass ratio and the chirp mass for waveforms including up to the 0.5 pN order amplitude correction. The 1.0 pN order amplitude correction decouples $\tilde{\Lambda}$ from chirp mass and decreases the strength of the coupling between $\tilde{\Lambda}$ and the symmetric mass ratio.

The minimum detectable deviation from the no-hair theorem for a near equal mass BBH system with $m_1 = 10 M_\odot$ and $m_2 = 11 M_\odot$ is $\tilde{\Lambda} = 7.61$ at 1σ for an SNR of 10 (or 3σ for an SNR of 30). For comparison, a typical value for $\tilde{\Lambda}$ for a binary neutron star system

Table 7 : **Advanced LIGO's ability to measure spin and tidal deformability, and therefore test cosmic censorship and the no-hair theorem, improves by...**

	restricting η parameter space	including higher harmonics	including spin in the amplitude	including the 3.0 pN, 3.5 pN spin-orbit phase terms
spinning BBH	yes, only at 0.0 pN	yes, starting at 0.5 pN	yes, starting at 1.0 pN	yes, mostly at 0.0 pN
spinning NS-BH	no	no	no	yes, for all pN orders
tidal BBH	no	yes, starting at 1.0 pN	N/A	N/A

is about 40, but the value of $\tilde{\Lambda}$ is strongly dependent on the equation of state (Lackey et al. 2012). For an incompressible star at maximum compactness, the tidal parameter would be $\tilde{\Lambda} \approx 0.002$ (Damour & Nagar 2009).

It is worth making a brief mention of what could be causing an apparent violation of cosmic censorship or the no-hair theorem. There could be exotic objects, such as boson stars, that do violate cosmic censorship or the no-hair theorem and therefore lead to an apparent violation through their gravitational waveform. However, observing an apparent violation of cosmic censorship or the no-hair theorem does not necessarily mean these conjectures are false. Rather, it could be the theory of gravity, general relativity, that is wrong, or it could be post-Newtonian theory that is wrong. The post-Newtonian waveforms employed in this paper are based on assumptions in standard general relativity, which could be violated for systems such as a naked singularity. However, in the case of a naked singularity, the quantum gravity effects that are fixing the singularity should only minimally affect the surrounding spacetime on which post-Newtonian waveforms are based. In addition, the assumptions of the Kerr solution, such as axial-symmetry and asymptotic flatness, could not be satisfied. However, detecting a nominal black hole that violates the Kerr bound or detecting internal structure in a nominal black hole would be inconsistent with the current post-Newtonian framework of general relativity and cosmological conjectures in the Kerr geometry.

We explore ways to improve aLIGO's ability to test cosmic censorship and the no-hair theorem by improving the measurability of spin and tidal deformability. We find several methods for improving parameter measurability that affect different systems and different amplitude-corrected waveforms in different ways. Table 7 summarizes our findings for how to improve parameter measurability for each astrophysical system that we examine. The pN orders in the table all refer to pN order in the amplitude of the waveform, except when indicated directly.

Our studies indicate that both a prior on the symmetric mass ratio and including higher harmonics in the waveform can have a significant effect on aLIGO's ability to test whether expectations from the cosmic censorship conjecture and the no-hair theorem are satisfied for some, but not all, systems.

For near equal mass spinning BBH systems, both a prior on the symmetric mass ratio and including higher harmonics could lead to significant improvement in spin and mass parameter measurability, and therefore significant improvement in aLIGO's ability to test cosmic censorship. In addition, including spin corrections in the amplitude, specifically the lowest-order spin correction to the first harmonic, could lead to even further improved measurability of spin and mass parameters. For the Newtonian-amplitude waveform or the waveforms with nonspinning amplitude corrections, the 3.0 pN and 3.5 pN order spin-orbit phase terms should lead to improved mass and spin measurability as well.

For the spinning NS-BH system, a prior on the symmetric mass ratio should not lead to much improvement in aLIGO's ability to test cosmic censorship. Higher harmonics should also not improve spin or mass parameter measurability for this system. However, the 3.0 pN and 3.5 pN order spin-orbit phase corrections should lead to improved mass and spin measurability for both Newtonian and amplitude-corrected waveforms.

For near equal mass nonspinning BBH systems with tidal corrections, a prior on the symmetric mass ratio will not improve aLIGO's ability to investigate the no-hair theorem, but including higher harmonics in the waveform will improve mass and tidal measurability.

A final benefit of using amplitude-corrected waveforms, which include higher harmonic effects, is discussed briefly in Sec. 4.4. Certain angle parameters, ϕ_c , ι , and ϕ , are unmeasurable for a single detector with the Newtonian-amplitude waveform. However, including the lowest-order amplitude correction in the waveform allows both ϕ_c and ι to become measurable, even for a single detector. Including spin corrections in the amplitude further allows the azimuthal angle ϕ to become measurable for a single detector. Therefore, higher harmonics can play a significant role in the measurability of some of the system's angle parameters, on top of the benefits to mass and spin measurability discussed above.

Overall, using a flat prior on the symmetric mass ratio and including higher harmonics in the waveform could provide aLIGO with a keen ability to test the theory of general relativity with gravitational-wave detections from black hole compact binary coalescence events in the near equal mass limit.

Chapter 5

Conclusions

“Good night, black hole.”

— Adam Gamble and Mark Jasper,
Goodnight Galaxy

5.1 Summary

The first direct detections of gravitational waves from astrophysical sources is imminent. The Laser Interferometer Gravitational-wave Observatory (LIGO) is poised as the leading experiment to participate in the first detections. Tackling the challenging problem of gravitational-wave detection requires immense effort spread across the entire gravitational-wave science workflow. This dissertation has reviewed work from three components of the gravitational-wave science workflow: (1) the procedure of converting the output of the LIGO detector into gravitational-wave strain (calibration), (2) a search for gravitational-wave signals in LIGO data, and (3) post-detection science including tests of general relativity.

The production of real-time gravitational-wave event candidates is a priority for the advanced detector era. With low-latency detection, we will be able to fully participate in electromagnetic follow-up observations to gravitational-wave detections. The essential first step in low-latency detection is low-latency calibration. I developed a low-latency time-domain calibration pipeline that will be operating in the advanced detector era using the `gstlal` software package. The pipeline has been tested during previous LIGO engineering runs and is currently producing calibrated data for analysis by the collaboration.

In addition, I have improved the procedure used to generate the FIR filters necessary¹¹³ for calibration such that the FIR filters now contain negligible errors. Overall, we are prepared with reliable and accurate low-latency calibration machinery as we enter into the first science-quality data taking with advanced interferometers.

The next step in the gravitational-wave science workflow after calibrating the data is searching the data for gravitational-wave signals. I performed a search on one month of Initial LIGO (iLIGO) data for sub-solar mass binary black hole systems. The motivation for this search was both astrophysical and computational. Not only could the search produce the first detection of gravitational waves or set new upper limits on the rate of sub-solar mass binary black hole mergers, but the search was also a proof-of-principle for an Advanced LIGO (aLIGO) binary neutron star (BNS) search. There are similarities in an iLIGO sub-solar mass binary search and an aLIGO BNS search in both the duration of signals in band and the number of templates required to appropriately populate the template bank. I used the `gstlal_inspiral` search pipeline, which is poised as the leading low-latency compact binary coalescence search pipeline in aLIGO. While no gravitational waves were found in the iLIGO sub-solar mass binary search, we did find the search was sensitive out to about 4 Mpc, which is beyond our Local Group. This means we are now able to probe many other galaxy halos for primordial black hole systems, whereas microlensing experiments are limited to searching our own Galactic halo. We found that, upon tuning the pipeline appropriately, we were able to run the search with very reasonable computational resources. We determined that we would only require about 200 CPUs to produce results for a search with this type of computational burden in low-latency. Therefore, the low-latency search pipeline is ready for an aLIGO BNS search at design sensitivity.

The final step in the gravitational-wave science workflow is post-detection science. Any gravitational-wave detection will be carefully analyzed after-the-fact for details on the source parameters and consistency of the source with general relativity. I studied aLIGO's ability to test two conjectures believed to be true in general relativity: the cosmic censorship conjecture and the no-hair theorem. I used the Fisher matrix formalism to determine how well aLIGO will be able to measure spin and tidal parameters for binary

black hole and neutron star – black hole systems. I investigated how aLIGO’s parameter estimation accuracy will affect our ability to distinguish a system that has violated either the cosmic censorship conjecture or the no-hair theorem. Including corrections to the amplitude of the gravitational waveform can break parameter degeneracies between mass and spin, allowing significant improvement in the measurability of the spin parameter and therefore aLIGO’s ability to test the cosmic censorship conjecture. In addition, amplitude corrections can break degeneracies with the tidal parameter, which improves aLIGO’s ability to test the no-hair theorem. I found with amplitude-corrected waveforms aLIGO could significantly improve its ability to test conjectures believed to be true in general relativity.

5.2 Further work

Each of the projects discussed in this dissertation can be expanded and improved in the future. Below I outline plans for continued work in each of fields.

- **Calibraiton:** I will continue to improve the accuracy and reliability of the low-latency time-domain calibration pipeline and prepare the infrastructure for the first advanced detector science run. We are moving towards a system where the frequency domain models can be automatically and reliably converted into FIR filters, allowing for a seamless flow of the low-latency calibration network. I will lead this effort and help continue to improve the calibration infrastructure in the advanced detector era.
- **Sub-solar mass binary search:** I will analyze all of LIGO’s fifth and sixth science runs for sub-solar mass binary black hole systems. In the absence of a detection, I will place a new upper limit on the existence of sub-solar mass binary black hole systems.
- **Testing cosmic censorship and the no-hair theorem:** I plan to expand this project by using a full Bayesian framework to study aLIGO’s ability to test conjectures believed to be true within general relativity. I will study how different waveform accuracies and how different priors affect aLIGO’s ability to measure spin and

the tidal parameters, and therefore to test the cosmic censorship conjecture and the ¹¹⁵ no-hair theorem.

5.3 Closing remarks

Each step in the gravitational-wave science workflow plays a crucial role in the effort to detect gravitational waves with LIGO. In combination, each effort brings us closer to our first confident, and fast, detection. In the near future, when gravitational-wave detections become common place, we will be able to embrace the wealth of new knowledge that is bound to be uncovered. I anxiously anticipate this time, and I am glad to have been involved in readying ourselves for the new era of gravitational-wave science.

Bibliography

- Abadie, J., Abbott, B. P., Abbott, R., et al. 2010, *Class. Quant. Grav.*, 27, 173001
- Abbott, B., Abbott, R., Adhikari, R., et al. 2005, *Phys. Rev. D*, 72, 082002
- Abbott, B. P., Abbott, R., Adhikari, R., & et al. 2009, *Rep. Prog. Phys*, 72
- Alcock, C., Allsman, R. A., Alves, D. R., et al. 2000, *ApJ*, 542, 281
- Allen, B., Anderson, W. G., Brady, P. R., Brown, D. A., & Creighton, J. D. E. 2012, *Phys. Rev. D*, 85, 122006
- Apostolatos, T. A., Cutler, C., Sussman, G. J., & Thorne, K. S. 1994, *Phys. Rev. D*, 49, 6274
- Arun, K. G., Buonanno, A., Faye, G., & Ochsner, E. 2009, *Phys. Rev. D*, 79, 104023
- Arun, K. G., Iyer, B. R., Qusailah, M. S. S., & Sathyaprakash, B. S. 2006, *Phys. Rev. D*, D74, 024006
- Arun, K. G., Iyer, B. R., Sathyaprakash, B. S., & Sundararajan, P. A. 2005, *Phys. Rev. D*, 71, 084008
- Arun, K. G., & Pai, A. 2013, *Int. J. Mod. Phys.*, D22, 1341012
- Arun, K. G., & Will, C. M. 2009, *Class. Quant. Grav.*, 26, 155002
- Baird, E., Fairhurst, S., Hannam, M., & Murphy, P. 2013, *Phys. Rev. D*, 87, 024035
- Ballmer, S., Brown, D. A., Couvares, P., et al. 2012, *Online Detector Characterization System Overview*, LIGO Document T1200323

- Bhattacharjee, P., Chaudhury, S., & Kundu, S. 2014, *ApJ*, 785
- Binnington, T., & Poisson, E. 2009, *Phys. Rev. D*, 80, 084018
- Blanchet, L. 2002, *Living Rev. Relat.*, 5, doi:10.12942/lrr-2002-3
- Brown, D. A., Lundgren, A., & O'Shaughnessy, R. 2012, *Phys. Rev. D*, 86, 064020
- Buonanno, A., Iyer, B. R., Ochsner, E., Pan, Y., & Sathyaprakash, B. S. 2009, *Phys. Rev. D*, 80, 084043
- Cannon, K., Chapman, A., Hanna, C., et al. 2010, *Phys. Rev. D*, 82, 044025
- Cannon, K., Hanna, C., & Keppel, D. 2013, *Phys. Rev. D*, 88
- Cannon, K., Hanna, C., & Peoples, J. 2015, Likelihood-Ratio Ranking Statistic for Compact Binary Coalescence Candidates with Rate Estimation, LIGO Document P1400175
- Cannon, K., Cariou, R., Chapman, A., et al. 2012, *ApJ*, 748, 1107.2665
- Cannon, K., Hanna, C., Keppel, D., et al. 2014, *gstlal*
- Carr, B. J., & Hawking, S. W. 1974, *Mon. Not. Roy. Astr. Soc.*, 168, 399
- Carter, B. 1970, *Phys. Rev. Lett.*, 26, 331
- Chatziioannou, K., Yunes, N., & Cornish, N. J. 2012, *Phys. Rev. D*, D86, 022004
- Cho, H.-S., Ochsner, E., O'Shaughnessy, R., Kim, C., & Lee, C.-H. 2013, *Phys. Rev. D*, 87, 024004
- Chrusciel, P. T., Costa, J. L., & Heusler, M. 2012, *Living Rev. Relat.*, 15, doi:10.12942/lrr-2012-7
- Creighton, J. D. E., & Anderson, W. G. 2011, *Gravitational-Wave Physics and Astronomy: An Introduction to Theory, Experiment and Data Analysis*, 1st edn. (Wiley-VCH)
- Cutler, C., & Flanagan, É. E. 1994, *Phys. Rev. D*, 49, 2658
- Damour, T., & Nagar, A. 2009, *Phys. Rev. D*, 80, 084035

- Damour, T., Nagar, A., & Villain, L. 2012, Phys. Rev. D, 85, 123007
- Dreyer, O., Kelly, B. J., Krishnan, B., et al. 2004, Class. Quant. Grav., 21, 787
- E., P. 1998, Phys. Rev. D, 57, 5287
- Einstein, A., Infeld, L., & Hoffmann, B. 1938, Annals of Mathematics, 39, pp. 65
- Epstein, R., & Wagoner, R. V. 1975, ApJ, 197, 717
- Faye, G., Blanchet, L., & Buonanno, A. 2006, Phys. Rev. D, 74, 104033
- Finn, L. S. 1992, Phys. Rev. D, 46, 5236
- Flanagan, E. E., & Hughes, S. A. 2005, New J. Phys., 7
- Gossan, S., Veitch, J., & Sathyaprakash, B. S. 2012, Phys. Rev. D, D85, 124056
- Gstreamer. 2015, Gstreamer open source multimedia framework
- Hannam, M., Brown, D. A., Fairhurst, S., Fryer, C. L., & Harry, I. W. 2013, ApJL, arXiv:1301.5616
- Harry, I. W., Nitz, A. H., Brown, D. A., et al. 2013, Phys. Rev. D, arXiv:1307.3562
- Hartle, J. B. 2003, Gravity: An Introduction to Einstein's General Relativity (Addison Wesley)
- Hawking, S. 1971, Phys. Rev. Lett., 26, 1344
- . 1972, Commun. Math. Phys., 25, 152
- Hawkins, M. 2015, A&A, 575, 7
- Hayama, K., & Nishizawa, A. 2013, Phys. Rev. D, D87, 062003
- Hinderer, T., Lackey, B. D., Lang, R. N., & Read, J. S. 2010, Phys. Rev. D, 81, 123016
- Hogg, D. W. 1999, ArXiv e-prints, arXiv:astro-ph/9905116
- HTCondor. 2015, HTCondor: High Throughput Computing, <http://research.cs.wisc.edu/htcondor/>

Israel, W. 1967, Phys. Rev. D, 164, 1776

—. 1968, Commun. Math. Phys., 8, 245

Johannsen, T., & Psaltis, D. 2013, ApJ, arXiv:1202.6069

Kamaretsos, I., Hannam, M., Husa, S., & Sathyaprakash, B. S. 2012, Phys. Rev. D, D85, 024018

Keppel, D., & Ajith, P. 2010, Phys. Rev. D, D82, 122001

Kerr, R. P. 1963, Phys. Rev. Lett., 11, 237

Kidder, L. E. 1995a, Phys. Rev. D, 52, 821

—. 1995b, Phys. Rev. D, 52, 821

Kidder, L. E., Will, C. M., & Wiseman, A. G. 1993, Phys. Rev. D, 47, 4183

Kissel, J., Betzweiser, J., Wade, M., et al. 2014, Interferometer Calibration Preliminary Design Document, LIGO Document T1300088

Królak, A., Kokkotas, K. D., & Schäfer, G. 1995, Phys. Rev. D, 52, 2089

Lackey, B. D., Kyutoku, K., Shibata, M., Brady, P. R., & Friedman, J. L. 2012, Phys. Rev. D, 85, 044061

Landry, P., & Poisson, E. 2015, arXiv:1503.07366

Lang, R. N., & Hughes, S. A. 2006, Phys. Rev. D, 74, 122001

Lang, R. N., Hughes, S. A., & Cornish, N. J. 2011, Phys. Rev. D, 84, 022002

Li, T., Del Pozzo, W., Vitale, S., et al. 2012, Phys. Rev. D, D85, 082003

LSC. 2015, LSC Algorithm Library (LAL)

Marsat, S., Bohé, A., Faye, G., & Blanchet, L. 2013, Class. Quant. Grav., 30, 055007

Mirshekari, S., Yunes, N., & Will, C. M. 2012, Phys. Rev. D, D85, 024041

- Misner, C. W., Thorne, K. S., & Wheeler, J. A. 1973, Gravitation (W.H. Freeman and Company) ¹²⁰
- Nielsen, A. B. 2013, *Class. Quant. Grav.*, 30, 075023
- Owen, B., & Sathyaprakash, B. S. 1999, *Phys. Rev. D*, 60, doi:10.1103/PhysRevD.60.022002
- Owen, B. J., Tagoshi, H., & Ohashi, A. 1998, *Phys. Rev. D*, 57, 6168
- Pai, A., & Arun, K. G. 2013, *Class. Quant. Grav.*, 30, 025011
- Pekowsky, L., O'Shaughnessy, R., Healy, J., & Shoemaker, D. 2013, *Phys. Rev. D*, 88, 024040
- Penrose, R. 1969, *Rivista del Nuovo Cimento*, 1, 252
- Poisson, E., & Will, C. M. 1995, *Phys. Rev. D*, 52, 848
- Porto, R. A. 2006, *Phys. Rev. D*, 73, 104031
- . 2010, *Class. Quant. Grav.*, 27, 205001
- Privitera, S. M. 2014, PhD thesis, California Institute of Technology
- Raymond, V., van der Sluys, M. V., Mandel, I., et al. 2010, *Class. Quant. Grav.*, 27, 114009
- Rodriguez, C. L., Farr, B., Farr, W. M., & Mandel, I. 2013, *Phys. Rev. D*, arXiv:1308.1397
- Rodriguez, C. L., Mandel, I., & Gair, J. R. 2012, *Phys. Rev. D*, 85, 062002
- Ruffini, R., & Wheeler, J. A. 1971, *Phys Today*, 24, 30
- Sadeghian, L., & Will, C. M. 2011, *Class. Quant. Grav.*, 28, 225029
- Shoemaker, D. 2009, Advanced LIGO anticipated sensitivity curves, LIGO Document T0900288

- Siemens, X., Allen, B., Creighton, J. D. E., Hewiston, M., & Landry, M. 2004, *Class. Quant. Grav.*, 21
- Singer, L., Price, L., Farr, B., et al. 2014, *ApJ*
- Sofue, Y. 2013, *PASJ*, 65
- Stairs, I. H. 2003, *Living Rev. Relat.*, 6, 5
- Tagoshi, H., Ohashi, A., & Owen, B. J. 2001, *Phys. Rev. D*, 63, 044006
- The LIGO Scientific Collaboration, the Virgo Collaboration, Aasi, J., Abadie, J., & et al. 2013, *Phys. Rev. D*, 87, 022002
- the LIGO Scientific Collaboration, the Virgo Collaboration, Abadie, J., Abbott, B. P., & et al. 2012, *Phys. Rev. D*, 85, 082002
- the LIGO Scientific Collaboration, the Virgo Collaboration, Aasi, J., et al. 2013, *Phys. Rev. D*, arXiv:1304.1775
- Thorne, K. S., Hawking, S. W., & Israel, W. 1987, *Three hundred years of gravitation* (Cambridge University Press), 330–458
- Thrane, E., Mullavey, A., Shawhan, P., & et al. 2014, *Documentation of the Advanced LIGO Hardware Injection Infrastructure*, LIGO Document T1400349
- Tisserand, P., Le Guillou, L., Afonso, C., et al. 2007, *A&A*, 469, 387
- Trimble, V. 1987, *A&A*, 25, 425
- Vallisneri, M. 2008, *Phys. Rev. D*, 77, 042001
- Van Den Broeck, C. 2013, book chapter for the *Springer Handbook of Spacetime*, arXiv:1301.7291
- Van Den Broeck, C., & Sengupta, A. S. 2007, *Class. Quant. Grav.*, 24, 1089
- Van Der Sluys, M., Raymond, V., Mandel, I., et al. 2008a, *Class. Quant. Grav.*, 25, 184011

- Van Der Sluys, M. V., Röver, C., Stroeer, A., et al. 2008b, *ApJL*, 688, L61
- Vecchio, A. 2004, *Phys. Rev. D*, 70, 042001
- Veitch, J., & Vecchio, A. 2010, *Phys. Rev. D*, 81, 062003
- Veitch, J., Mandel, I., Aylott, B., et al. 2012, *Phys. Rev. D*, 85, 104045
- Wade, M. 2012, SNR loss summed over time slices due to SVD basis reduction, LIGO Document T1500168
- Wade, M., Creighton, J. D. E., Ochsner, E., & Nielsen, A. B. 2013, *Phys. Rev. D*, 88, doi:10.1103/PhysRevD.88.083002
- Wade, M., Siemens, X., Betzweiser, J., et al. 2014, Time domain calibration in Advanced LIGO, LIGO Document T1400256
- Weinberg, S. 1972, *Gravitation and Cosmology: Principles and Applications of the General Theory of Relativity* (John Wiley & Sons, Inc.)
- Wyrzykowski, L., Skowron, J., Kozłowski, S., et al. 2011, *Mon. Not. R. Astron. Soc.*, 416, 2949
- Yunes, N., & Pretorius, F. 2009, *Phys. Rev. D*, D80, 122003
- Yunes, N., & Siemens, X. 2013, *Living Rev. Relat.*, arXiv:1304.3473
- Zel'Dovich, Y. B., & Novikov, I. D. 1967, *Soviet Astronomy*, 10, 602
- Zweizig, J. G., & et al. 2014, Low Latency Data Distribution System Design, LIGO Document T1400343

CURRICULUM VITAE

123

Madeline Wade

Place of birth: Albany, NY

EDUCATION

- 8/2009–5/2015* **Doctor of Philosophy in Physics**
University of Wisconsin – Milwaukee, Milwaukee WI
Advisors: Dr. Jolien Creighton and Dr. Xavier Siemens
Awards: Research Excellence Award, Chancellor’s Graduate Student Award,
Physics Graduate Student Award
GPA: 3.82/4.00
- 8/2011–5/2014* **Certificate of Teaching and Learning in Higher Education**
University of Wisconsin – Milwaukee, Milwaukee, WI
Advisor: Dr. Simone Conceição
GPA: 4.00/4.00
- 8/2005–5/2009* **Bachelor of Science in Physics (mathematics minor)**
Bates College, Lewiston, ME
Advisor: Dr. Eric Wollman
Honors: Physics Honors, *Summa Cum Laude*, Phi Beta Kappa, Sigma Xi,
Dean’s List
GPA: 3.90/4.00
- 1/2008–5/2008* **Study Abroad Semester**
Danish Institute for Study Abroad, Copenhagen, Denmark

RESEARCH EXPERIENCE

- 6/2010–present* **Member of Laser Interferometer Gravitational-wave Observatory (LIGO)**
Work in the Compact Binary Coalescence working group, the Data Analysis
Software Working Group, and the Calibration Group.
- 6/2010–present* **Graduate Research Assistant**
University of Wisconsin - Milwaukee, Milwaukee WI
Advisors: Dr. Jolien Creighton and Dr. Xavier Siemens
Calibration of Advanced LIGO Data
Leading the time domain calibration effort in Advanced LIGO.
Initial LIGO sub-solar mass binary search
Leading a search for sub-solar mass binaries in Initial LIGO data.
*Using the Measurability of spin to test the cosmic censorship conjecture
and the no-hair theorem*
Led a theoretical project involving parameter estimation of compact
binary coalescence gravitational-wave signals to verify cosmic censorship
and the no-hair theorem.

TEACHING EXPERIENCE

- 8/2009–12/2014 **Teaching Assistant and Lecturer**
 University of Wisconsin – Milwaukee, Milwaukee, WI
Lecturer for “Survey of Astronomy”
 Was the sole lecturer for a total of three sections of introductory astronomy across two semesters.
Course design and lecturer for “The Art and Science of Teaching Physics”
 Redesigned and lectured a course aimed to educate incoming graduate students on teaching methods for physics.
Discussion section leader for introductory and advanced physics courses
 Led discussion sections for both introductory undergraduate courses and advanced level graduate courses.

FELLOWSHIPS & AWARDS

- 2012–2015 NASA Wisconsin Space Grant Consortium Fellowship Recipient
 2013, 2014 Distinguished Dissertation Fellowship Nominee (UWM)
 2013 Department of Physics Papastamatiou Scholarship (UWM)
 2012 Gravitational-wave Physics and Astronomy Workshop Poster Prize

PHYSICS EDUCATION RESEARCH

- 1/2014–5/2014 **Study on Concept Mapping in an Introductory Astronomy Course**
 University of Wisconsin – Milwaukee, Milwaukee, WI
 Performed a study on the effectiveness of concept mapping as a learning tool in an introductory astronomy course.

INVITED TALKS

- 1/2015 **LIGO Seminar**
 California Institute of Technology, Pasadena, CA
 Presented on dissertation research.

CONFERENCES AND PRESENTATIONS

LIGO-Virgo Fall Meeting, Stanford, CA, Aug. 2014. Oral presentation on the status of aLIGO calibration on behalf of the LIGO Calibration Team.

23rd Annual Midwest Relativity Meeting, Milwaukee, WI, Oct. 2013. Oral presentation on Ph.D. research project and publication “Using the measurability of spin to test the cosmic censorship conjecture and the no-hair theorem.”

LIGO-Virgo Fall Meeting, Hannover, Germany, Sept. 2013.

20th International Conference on General Relativity and Gravitation and 10th Amaldi Conference on Gravitational Waves, Warsaw, Poland, July 2013. Oral presentation on Ph.D. research project and publication “Using the measurability of spin to test the cosmic censorship conjecture and the no-hair theorem.”

LIGO-Virgo Spring Meeting, Bethesda, MD, March 2013.

American Astronomical Society Annual Meeting, Long Beach, CA, Jan. 2013. Oral presentation on Ph.D. research project and publication “Using the measurability of spin to test the cosmic censorship conjecture and the no-hair theorem.”

22nd Annual Midwest Relativity Meeting, Chicago, IL, Sept. 2012. Oral presentation on Ph.D. research “Search for sub-solar mass black holes in LIGO’s fifth science run.”

Gravitational-Wave Physics and Astronomy Workshop, Hannover, Germany, June 2012. Poster and oral presentation on Ph.D. research project and publication “Using the measurability of spin to test the cosmic censorship conjecture and the no-hair theorem.” Received second place poster prize.

Phenomenology 2012 Symposium, Pittsburgh, PA, May 2012. Oral presentation on Ph.D. research project and publication “Using the measurability of spin to test the cosmic censorship conjecture and the no-hair theorem.”

American Physical Society April Meeting, Atlanta, GA, April 2012. Poster presentation on Ph.D. research project and publication “Using the measurability of spin to test the cosmic censorship conjecture and the no-hair theorem.”

LIGO-Virgo Spring Meeting, Boston, MA, March 2012.

21st Annual Midwest Relativity Meeting, Urbana, IL, Nov. 2011. Oral presentation on Ph.D. research project and publication “Using the measurability of spin to test the cosmic censorship conjecture and the no-hair theorem.”

20th Annual Midwest Relativity Meeting, Guelph, Ontario, Nov. 2010. Oral presentation on research project “Construction of coherent and null LIGO data streams.”

PUBLICATIONS

Primary Publications

M. Wade, J. Creighton, E. Ochsner, and A. Nielsen. “Advanced LIGOs ability to detect apparent violations of the cosmic censorship conjecture and the no-hair theorem through compact binary coalescence detections.” *Phys. Rev. D* 88 (2013) 083002.

M. Wade, X. Siemens, et al. “Making $h(t)$ in Advanced LIGO”. (in prep.)

Collaboration Publications

The LIGO Scientific Collaboration, the Virgo Collaboration: J. Aasi, ... , **M. Wade**, et al. “Searching for stochastic gravitational waves using data from the two co-located LIGO Hanford detectors.” *Phys. Rev. D* 91 (2015) 022003.

The LIGO Scientific Collaboration, the Virgo Collaboration: J. Aasi, ... , **M. Wade**, et al. “Improved Upper Limits on the Stochastic Gravitational-Wave Background from 2009-2010 LIGO and Virgo Data.” *Phys. Rev. Lett.* 113 (2014) 231101.

The IceCube Collaboration, The LIGO Scientific Collaboration, the Virgo Collaboration: M.G. Aartsen, ... , **M. Wade**, et al. “Multimessenger Search for Sources of Gravitational Waves and High-energy Neutrinos: Results of the Initial LIGO-Virgo and IceCube.” Phys. Rev. D 90 (2014) 102002.

The LIGO Scientific Collaboration, the Virgo Collaboration: J. Aasi, ... , **M. Wade**, et al. “Implementation of an F-statistic all-sky search for continuous gravitational waves in Virgo VSR1 data.” Class. Quantum Grav. 31 (2014) 165014.

The LIGO Scientific Collaboration, the Virgo Collaboration: J. Aasi, ... , **M. Wade**, et al. “First all-sky search for continuous gravitational waves from unknown sources in binary systems.” Phys. Rev. D 90 (2014), 062010.

The LIGO Scientific Collaboration, the Virgo Collaboration: J. Aasi, ... , **M. Wade**, et al. “First Searches for Optical Counterparts to Gravitational-wave Candidate Events.” ApJS 211 (2014) 7.

The LIGO Scientific Collaboration, the Virgo Collaboration: J. Aasi, ... , **M. Wade**, et al. “Constraints on cosmic strings from the LIGO-Virgo gravitational-wave detectors.” Phys. Rev. Lett. 112 (2014) 131101.

The LIGO Scientific Collaboration, the Virgo Collaboration: J. Aasi, ... , **M. Wade**, et al. “Application from a Hough search for continuous gravitational waves on data from the 5th LIGO science run.” Class. Quantum Grav. 31 (2014) 085014.

The LIGO Scientific Collaboration, the Virgo Collaboration: J. Aasi, ... , **M. Wade**, et al. “The NINJA-2 project: Detecting and characterizing gravitational waveforms modelled using numerical binary black hole simulations.” Class. Quantum Grav. 31 (2014) 115004.

The LIGO Scientific Collaboration, the Virgo Collaboration: J. Aasi, ... , **M. Wade**, et al. “Search for gravitational wave ringdowns from perturbed intermediate mass black holes in LIGO-Virgo data from 2005-2010.” Phys. Rev D 89 (2014) 102006.

The LIGO Scientific Collaboration, the Virgo Collaboration: J. Aasi, ... , **M. Wade**, et al. “Search for gravitational waves associated with gamma-ray bursts detected by the InterPlanetary Network.” Phys. Rev. Lett. 113 (2014) 011102.

The LIGO Scientific Collaboration, the Virgo Collaboration: J. Aasi, ... , **M. Wade**, et al. “Search for gravitational radiation from intermediate mass black hole binaries in data from the second LIGO-Virgo joint science run.” Phys. Rev. D 89 (2014) 122003.

The LIGO Scientific Collaboration, the Virgo Collaboration: J. Aasi, ... , **M. Wade**, et al. “Methods and results of a search for gravitational waves associated with gamma-ray bursts using the GEO600, LIGO, and Virgo detectors.” Phys. Rev. D 89 (2014) 122004.

The LIGO Scientific Collaboration, the Virgo Collaboration: J. Aasi, ... , **M. Wade**, et al. “Search for long-lived gravitational- wave transients coincident with long gamma-ray bursts.” Phys. Rev. D 88 (2013) 122004.

The LIGO Scientific Collaboration, the Virgo Collaboration: J. Aasi, ... , **M. Wade**,¹²⁷ et al. “A directed search for continuous Gravitational Waves from the Galactic Center.” Phys. Rev. D 88 (2013) 102002.

The LIGO Scientific Collaboration, the Virgo Collaboration: J. Aasi, ... , **M. Wade**, et al. “Parameter estimation for compact binary coalescence signals with the first generation gravitational-wave detector network.” Phys. Rev. D 88 (2013) 062001.

The LIGO Scientific and the Virgo Collaborations: J. Aasi, ... , **M. Wade**, et al. “Search for Gravitational Waves from Binary Black Hole Inspiral, Merger and Ringdown in LIGO-Virgo Data from 2009-2010.” Phys. Rev. D 87 (2013) 022002.

The LIGO Scientific and the Virgo Collaborations: J. Aasi, ... , **M. Wade**, et al. “Einstein@Home all-sky search for periodic gravitational waves in LIGO S5 data.” Phys. Rev. D 87 (2013) 042001.

The LIGO Scientific Collaboration. “Enhancing the sensitivity of the LIGO gravitational wave detector by using squeezed states of light.” Nature Photonics 7 (2013) 613.

The ANTARES Collaboration, the LIGO Scientific Collaboration and the Virgo Collaboration: S. Adrian-Martinez, ... , **M. Wade**, et al. “A First Search for coincident Gravitational Waves and High Energy Neutrinos using LIGO, Virgo and ANTARES data from 2007.” JCAP 1306 (2013) 008.

The LIGO Scientific and the Virgo Collaborations: J. Abadie, ... , **M. Wade**, et al. “Search for Gravitational Waves from Intermediate Mass Binary Black Holes.” Phys. Rev. D 85 (2012) 102004.

The LIGO Scientific and the Virgo Collaborations: J. Abadie, ... , **M. Wade**, et al. “All-sky search for gravitational-wave bursts in the second LIGO-Virgo run.” Phys. Rev. D 85 (2012) 122007.

The LIGO Scientific and the Virgo Collaborations: J. Abadie, ... , **M. Wade**, et al. “Upper limits on a stochastic gravitational- wave background using LIGO and Virgo interferometers at 600-1000 Hz.” Phys. Rev. D 85 (2012) 122001.

J. Aasi, ... , **M. Wade**, et al. “The characterization of Virgo data and its impact on gravitational-wave searches.” Class. Quantum Grav. 29 (2012) 15502.

P.A. Evans, ... , **M. Wade**, et al. “Swift follow-up observations of candidate gravitational-wave transient events.” ApJS 203 (2012) 28.

The LIGO Scientific Collaboration, Virgo Collaboration: J. Abadie, ... , **M. Wade**, et al. “Search for gravitational waves associated with gamma-ray bursts during LIGO science run 6 and Virgo science runs 2 and 3.” Astrophys. J. 760 (2012) 12.